

Nanocrystalline metals: transient testing during in situ X-ray diffraction and molecular dynamics

THÈSE N° 7092 (2016)

PRÉSENTÉE LE 30 AOÛT 2016

À LA FACULTÉ DES SCIENCES ET TECHNIQUES DE L'INGÉNIEUR
LABORATOIRE DE MÉTALLURGIE MÉCANIQUE
PROGRAMME DOCTORAL EN SCIENCE ET GÉNIE DES MATÉRIAUX

ÉCOLE POLYTECHNIQUE FÉDÉRALE DE LAUSANNE

POUR L'OBTENTION DU GRADE DE DOCTEUR ÈS SCIENCES

PAR

Zhen SUN

acceptée sur proposition du jury:

Prof. P. Muralt, président du jury
Prof. H. Van Swygenhoven, Dr S. Van Petegem, directeurs de thèse
Prof. T. Pardoen, rapporteur
Prof. R. Pippan, rapporteur
Prof. R. Logé, rapporteur



ÉCOLE POLYTECHNIQUE
FÉDÉRALE DE LAUSANNE

Suisse
2016

Acknowledgements

This thesis could not have been finished without the help and support from many people. Herein, it is my great pleasure to acknowledge them.

Foremost, I would like to express my sincere gratitude to my mentors Prof. Helena Van Swygenhoven and Dr. Steven Van Petegem for their constant guidance and continuous support throughout my PhD study. Their immense knowledge, experience, and encouragement helped me all the time including building this thesis from the first draft to the last version. Also, I would like to thank Prof. Van Swygenhoven for supporting me in broadening my understanding of related fields and presenting this project in international conferences and workshops, as well as for providing advice on my personal development and career.

My sincere thanks are extended to Prof. Roland Logé, Prof. Thomas Pardoën, and Prof. Reinhard Pippan for their time in reviewing this manuscript and joining in the Examination Committee, and to Prof. Paul Muralt for chairing the examination procedure. They provided me with their insightful comments and suggestions, and let my defence be an enjoyable moment.

My sincere appreciation also goes to many collaborators. I would like especially to thank Prof. Wolfgang Blum for his expertise in transient testing and constant support in meticulous data analysis as well as results discussion. I am grateful for his tremendous time investment in this project, providing deep vision and invaluable guidance. Also, I am deeply touched by his dedication and passion for science; even retirement did not keep him from persistently conducting the scientific research. I would also like to thank Prof. Karsten Durst for materials supply and contributions to scientific discussion in this project. Particularly, I am indebted to Dr. Christian Brandl for his implementation of MD simulations and valuable inputs into technique and discussion parts of this thesis.

It was a privilege to work with the researchers and technical staff in PSI. I am extremely thankful to Dr. Elisabeth Müller for her patience and guidance in my FIB and TEM experiments. She has been always willing to help whenever I had requests or encountered issues in the lab. In particular, I am indebted to Alex Bollhalder who gave indispensable contributions to the development of setup for *in situ* mechanical tests. Also, I would like to thank Dr. Antonio Cervellino (beamline scientist at MS beamline), Dr. Sousan Abolhassani, Anja Weber, and Dr. Ekaterina Pomjakushina, who have helped me with their technique support.

Many thanks to all the former and current colleagues in the Photons for Engineering and Manufacturing group at PSI: Deniz, Cecile, Michael (Weisser), Christophe, Mario, Julia, Vadim, Steven, Patrick, Michael (Wedel), Tobias, Tram, Antoine, Michael (Kessler), Harry, Benedikt, Anna, Jean-Baptiste, Ainara, Saba, Nicolo, Manas, Karl, Wei-Neng, Maxime, Marina, Efthymios, Miroslav, Jan, and Thomas. They made contributions in many ways: sharing the knowledge, providing advice and support, and creating a pleasant atmosphere in the group. I am especially thankful to Maxime and Tobias for their help at the final rush of the thesis. A special thank you goes to Ainara and Saba who I started my PhD study together with.

Acknowledgements

Throughout the last four years, we supported each other and had so much fun and memory along the way. My sincere gratitude also goes to Renate Bercher and Martina Füglistner as they have always been helpful with the administrative issues.

Last but not the least, I sincerely thank my parents and friends for supporting me unconditionally throughout my entire life. This thesis is dedicated to my husband Wentao for all his love, understanding, and constant encouragement, and for bringing colour to my life.

Abstract

Nanocrystalline (NC) metals have attracted widespread interest in materials science due to their high strength compared to coarse-grained (CG) counterparts. It is well known that during uniaxial deformation, the stress-strain behaviour exhibits an extraordinary work-hardening followed by an early observation of constant flow stress. Information on possible deformation mechanisms have been gathered by extensive research combining *in situ* deformation experiments, electron microscopy observations and computational modelling. Generally, these mechanisms are categorized into two types: dislocation slip and grain boundary (GB) accommodation processes, as for instance, GB sliding based mechanisms and GB migration eventually coupled to the shear stress. However, the interplay between these mechanisms resulting in the constant deformation resistance is not fully understood.

Transient testing has proven to be a suitable tool to gather information on the rate limiting deformation mechanisms that are activated during the deformation path. In particular in stress reduction experiments, after an intermediate/large stress drop thermally activated dislocation slip is suppressed so that other underlying mechanisms are brought into foreground during subsequent transient creep. Those mechanisms may play a minor role in the determination of the flow stress but might still be essential to the development of a constant deformation resistance. Within this thesis, transient testing is combined with *in situ* X-ray diffraction at the Swiss Light Source. Therefore, transient responses are captured in terms of evolution of macrostrain as well as diffraction peak broadening. Since dislocation slip and GB accommodation have an opposite footprint on the peak broadening, the presence of these two types of mechanisms can be distinguished.

Three electrodeposited NC materials with different grain sizes are investigated: two NC Ni batches and one NC Ni₅₀Fe₅₀ batch. The results reveal that the constant flow stress reached during uniaxial deformation of electrodeposited NC metals reflects a quasi-stationary balance between dislocation-based mechanisms and GB-mediated accommodation. The latter plays an important role in the generation of plastic strain and the recovery of defects and internal stresses. Depending on the magnitude of the stress drop, a non-monotonic behaviour of the diffraction peak width is observed, suggesting an alternation of mechanisms. Also, by comparing transient responses among different NC materials, the relative contributions of dislocation slip and GB accommodation mechanisms are discussed in terms of grain size and alloying.

Finally, different magnitudes of stress reduction are carried out by molecular dynamics (MD) simulations with the aim of verifying *in situ* experimental results and exploring the mechanisms responsible for GB accommodation. MD simulations confirm that dislocation slip is reduced after a moderate stress drop, however can continue to operate after adaption of the GB structures by a variety of GB accommodation mechanisms. This can explain the non-monotonic behaviour of the peak broadening during transient creep.

Keywords

Nanocrystalline metals and alloys, *in situ* X-ray diffraction (XRD), stress reduction tests, molecular dynamics (MD), constant deformation resistance

Zusammenfassung

Nanokristalline (NK) Metalle haben, aufgrund ihrer hohen Stärke, verglichen mit ihren grobkörnigen (GK) Gegenständen, ein weit gefächertes Interesse in den Materialwissenschaften geweckt. Es ist sehr gut bekannt, dass die Spannungs-Dehnungs-Beziehung eine ausgeprägte Arbeitsverfestigung zeigt, die von einer frühen konstanten Fließspannung gefolgt wird. Informationen über mögliche Verformungsmechanismen wurden durch intensive Forschungen, welche in-situ Verformungsexperimente, Elektronenmikroskopie und Computersimulationen kombinieren, gewonnen. Im Allgemeinen lassen sich diese in zwei Kategorien einteilen: Versetzungsgleiten und Korngrenzen-Kohärenzspannungs-Prozesse, zum Beispiel Korngrenzen-Gleit-Prozesse, die möglicherweise mit Scherspannungen kombiniert sind. Wie auch immer, das Zusammenspiel dieser Mechanismen resultiert in einem konstanten Verformungswiderstand, der noch nicht voll verstanden ist.

Übergangs-Verformungsexperimente sind eine geeignete Methode um Informationen über die Geschwindigkeit abhängigen Verformungsmechanismen zu gewinnen, die während der Verformung aktiviert werden. In Besonderen sind bei Spannungs-Reduktions-Experimenten nach einem moderaten/ hohen Spannungsabfall die thermisch aktivierten Versetzungsgleit-Prozesse unterdrückt, so dass die zugrundeliegenden Mechanismen bei kleinen Übergangskriechschritten sichtbar werden.

Diese Mechanismen spielen zwar eine untergeordnete Rolle bei der Bestimmung der Fließspannung, sind aber grundlegend für die Entwicklung des konstanten Verformungswiderstandes. In dieser Arbeit werden Übergangs-Verformungsexperimente mit in-situ Röntgenbeugungsexperimenten an der Swiss Light Source (SLS) kombiniert. Dabei wird die Reaktion beim Übergang als Entwicklung der Makrospannung sowie der Verbreiterung der Beugungspeaks gemessen. Da das Versetzungsgleiten und die Korngrenzen-Kohärenzspannungen einen entgegengesetzten Einfluss auf die Verbreiterung der Beugungspeaks haben, kann die Anwesenheit dieser beiden Mechanismen während des Prozesses bestimmt werden.

Es wurden drei galvanisch abgeschiedene nanokristalline Materialien mit unterschiedlichen Korngrößen untersucht: zwei Sätze nanokristallines Nickel (Ni) und ein Satz einer nanokristallinen Nickel-Eisen-Legierung ($\text{Ni}_{50}\text{Fe}_{50}$). Die Ergebnisse zeigen, dass der konstante Verformungswiderstand, der sich bei uniaxialen Verformungsexperimenten von galvanisch abgeschiedene nanokristalline Materialien einstellt, ein quasi-stationäres Gleichgewicht zwischen versetzungsbasierten und Korngrenzen-Kohärenzspannungsbasierten Mechanismen darstellt. Der Letztere spielt eine wichtige Rolle bei der Erzeugung von plastischer Verformung, dem Abbau von Defekten und allgemein bei internen Spannungen. In Abhängigkeit von der Amplitude des Spannungsabfalls kann eine nicht-monotone Entwicklung der Verbreiterung der Beugungspeaks beobachtet werden, die einen Wechsel der zugrundeliegenden Mechanismen vermuten lässt. Des Weiteren werden die relativen Beiträge der Versetzungsgleit- und Korngrenzen-Kohärenzspannungs-Mechanismen anhand eines Vergleichs der Übergangsreaktionen zwischen den verschiedenen nanokristallinen Materialien in Hinsicht auf die Korngrößen und die Materialzusammensetzung diskutiert.

Abschließend wurden Molekular dynamische Simulationen mit verschiedenen Spannungsreduktionsstärken durchgeführt, um die in-situ Experimente zu verifizieren und die verantwortlichen Mechanismen für die Korngrenzen-Kohärenzspannung zu bestimmen. Die MD Simulationen bestätigen, dass das Versetzungsgleiten nach einem moderaten Spannungsabfall unterdrückt ist, aber nach Anpassung an die Korngrenzenstruktur durch verschiedene Korngrenzen-Kohärenz-spannung-Prozesses das Versetzungsgleiten weiterhin aktiv sein kann. Dieses liefert eine Erklärung für das nicht-monotone Verhalten der Verbreiterung der Beugungspeaks während des Übergangskriechvorganges.

Schlagworte

Nanokristalline Metalle und Legierungen, in-situ Röntgen Beugung (XRD), Spannungsabfall Tests, Molekulare Dynamik, konstanter Verformungswiderstand

Contents

Acknowledgements	i
Abstract	iii
Zusammenfassung	v
Contents	vii
List of Figures	xi
List of Tables	xix
List of Abbreviations	xxi
Chapter 1 Introduction	1
1.1 Deformation mechanisms in nanocrystalline metals	2
1.1.1 Dislocation-based mechanisms	2
1.1.2 GB-mediated accommodation.....	3
1.1.3 Theoretical models of deformation	4
1.2 Nanocrystalline alloy.....	5
1.3 <i>In situ</i> testing.....	6
1.3.1 <i>In situ</i> TEM.....	6
1.3.2 <i>In situ</i> X-ray diffraction	6
1.4 Transient testing.....	7
1.5 Thesis outline	8
1.6 Thesis structure.....	10
Chapter 2 Experimental and technical details	13
2.1 Materials description.....	13
2.1.1 NC Nickel.....	13
2.1.2 NC Ni ₅₀ Fe ₅₀ alloy.....	16
2.2 Specimen preparation.....	16
2.2.1 Mechanical testing.....	16
2.2.2 TEM characterization.....	16
2.3 Mechanical testing	17

Contents

2.3.1	Tensile testing.....	17
2.3.2	Compression testing.....	20
2.3.3	Stress reduction operation mode	22
2.4	X-ray powder diffraction	23
2.4.1	Fundamental principle.....	23
2.4.2	Material Science Beamline at the SLS.....	23
2.4.3	<i>In situ</i> experiments.....	24
2.4.4	Peak profile fitting.....	28
2.4.5	Extracting structural parameters.....	28
2.5	Molecular dynamic simulations	31
2.5.1	Molecular dynamics	31
2.5.2	Simulation procedure	32
2.5.3	Analysis techniques.....	33
Chapter 3	Experimental Results.....	35
3.1	Plastic deformation of nanocrystalline Nickel	35
3.1.1	<i>In situ</i> continuous deformation	35
3.1.2	Continuous deformation at different strain rates	38
3.1.3	<i>In situ</i> load-unload deformation.....	38
3.1.4	Summary.....	41
3.2	Stress reduction tests on nanocrystalline Nickel	41
3.2.1	Conventional stress reduction tests.....	41
3.2.2	Inserting creep before stress reduction.....	49
3.2.3	Multistep test	50
3.2.4	Summary.....	55
3.3	Stress reduction tests on nanocrystalline Ni ₅₀ Fe ₅₀ alloy.....	56
3.3.1	Conventional stress reduction tests.....	56
3.3.2	Multistep test	59
3.3.3	Summary.....	61
3.4	Grain size evaluation.....	61
3.4.1	<i>In situ</i> X-ray diffraction	61
3.4.2	Post-mortem TEM.....	62
3.4.3	Summary.....	62

Contents

Chapter 4	Molecular dynamics simulation results	67
4.1	Overview of stress reduction tests series	67
4.2	A medium stress reduction with longer creep.....	69
4.2.1	Dislocation emission.....	69
4.2.2	Dislocation-dislocation interaction	71
4.2.3	GB-mediated accommodation.....	72
4.3	Summary	76
Chapter 5	Discussion	79
5.1	Nanocrystalline Ni	79
5.1.1	Major observations	79
5.1.2	Deformation behaviour	80
5.1.3	Grain size effects.....	88
5.1.4	Activation volume and athermal stress	89
5.2	Nanocrystalline Ni ₅₀ Fe ₅₀ versus Ni.....	89
5.2.1	Major observations	89
5.2.2	Deformation behaviour	91
5.3	MD simulation at lower strain rates.....	95
Chapter 6	Conclusion	99
6.1	Achieved results	99
6.2	Outlook.....	101
References		103
Curriculum Vitae		115

List of Figures

Figure 1-1 Deformation mechanisms in NC face-centred cubic (FCC) metals [19]...	2
Figure 1-2 Stress–strain curves for a tensile test (green) and a compression test (red) in NC Ni.....	9
Figure 1-3 A graph of thesis outline	10
Figure 2-1 Cross-sectional view of as-received NC Ni_35: (a) a bright field TEM image and (b) grain size distribution.	14
Figure 2-2 In-plane view of as-received NC Ni_35: (a) a bright field TEM image and (b) grain size distribution.	15
Figure 2-3 Cross-sectional view of as-received NC Ni_65: (a) a bright field TEM image and (b) grain size distribution.	15
Figure 2-4 In-plane view of as-received NC Ni_65: (a) a bright field TEM image and (b) grain size distribution.	15
Figure 2-5 (a) During mechanical testing, the loading direction is perpendicular to the normal vector of the deposition plane. (b) For both non-deformed and deformed specimens, lamellae along the cross-section and in-plane direction were cut for TEM characterization.	16
Figure 2-6 Technical drawings of (a) the micro tensile machine (MTM) [18]. (b) the mini dogbone-shaped tensile test specimen, and (c) the specimen grips [124].	17
Figure 2-7 (a) E_{app} was determined as a function of force F from a multistep test. (b) The logarithm of $1/E_{app}$ is linearly proportional to the force F	19
Figure 2-8 (a) A qualitative picture of stress versus total strain curve for a load-unload test. (b) Stress versus inelastic strain curve after subtracting the elastic component.	20
Figure 2-9 Technical drawings of (a) the micro compression machine (K&W) and (b) the cuboid specimen.....	21
Figure 2-10 Schematic representation of transient testing via stress reduction during a constant strain rate test.....	22
Figure 2-11 (a) Block diagram of the positions of the most important beamline components, the abbreviations of which are briefly illustrated in Table 2-4. The white beam is shown in purple, and the monochromatic beam in yellow. (b) A schematic of the optics set-up (reproduced from [128])......	24
Figure 2-12 <i>In situ</i> tensile deformation apparatus at the MS beamline.....	25
Figure 2-13 <i>In situ</i> compression deformation apparatus at the MS beamline: (a) front view, and (b) back view at the connection between K&W machine and goniometer.	25

List of Figures

- Figure 2-14 The scattering geometry for X-ray diffraction: (a) before deformation, and (b) under tension..... 26
- Figure 2-15 A schematic illustration of grain size measurement during *in situ* deformation: (a) under the condition of a fixed angle, the estimation of coherent scattering length (seen as grain size) from Willison-Hall analysis use {111} and {222} diffraction peaks that differ in the direction of scattering vector. (b) After the alignment of the scattering vector in the same direction, the accuracy of measurement can be improved..... 27
- Figure 2-16 Influence of the specimen geometry on the instrumental broadening: (a) a typical case for a mini dogbone-shaped specimen used in MTM, and (b) a typical case for a cuboid specimen used in K&W. This figure is reproduced from Ref. [123]..... 28
- Figure 2-17 A cell structure of the constructed sample, in which atoms are coloured via CNA analysis..... 34
- Figure 3-1 Overview of deformation behaviour during the *in situ* continuous tensile tests for Ni₃₅ (a-d) and Ni₆₅ (e-h): (a, e) the stress-strain curves; (b, f) corresponding evolution of the transverse lattice strain for {111}, {200}, {220}, and {311} grain families; (c, g) deviation of lattice strain from the linear fit (dashed line); (d, h) corresponding evolution of FWHM for all grain families. 36
- Figure 3-2 The evolution of the FWHM for {111}, {200}, {220}, and {311} grain families as a function of total strain: (a) NC Ni₃₅ and (b) NC Ni₆₅..... 37
- Figure 3-3 NC Ni₃₅: (a) the stress-strain curve of a compression test; (b) the evolution of the FWHM for {111}, {200}, {220}, and {311} grain families as a function of total strain. 37
- Figure 3-4 The quasi-stationary stress values for NC Ni₃₅ (solid) and NC Ni₆₅ (open) obtained in continuous tensile tests at constant strain rates..... 38
- Figure 3-5 The corresponding stress-strain curves of a series of load-unload cycles for (a) NC Ni₃₅ and (b) Ni₆₅..... 39
- Figure 3-6 Overview of deformation behaviour during *in situ* load-unload tensile tests for Ni₃₅ (a-c) and Ni₆₅ (d-f): (a, d) the stress-time relation; (b, e) corresponding evolution of the lattice strain for {111}, {200}, {220}, and {311} grain families; (c, f) corresponding evolution of the FWHM for all grain families. 40
- Figure 3-7 NC Ni₃₅: (a) the stress-strain curve of a series of load-unload cycles in compression; (b) the evolution of the FWHM for {111}, {200}, {220}, and {311} grain families as a function of time. 41
- Figure 3-8 Schematic representation of a series of conventional stress reduction tests: the specimen is first strained to a pre-defined stress σ_0 reached with a constant loading rate, followed by a fast stress reduction and creep at a reduced stress σ_r . Finally, at the end of creep the specimen is reloaded until fracture. 42
- Figure 3-9 Results of the standard *in situ* stress reduction tests series on NC Ni₃₅. Transient responses in dependence of R for $\sigma_0 = 1.75$ GPa: (a) the inelastic strain, and

(b) the FWHM of the {311} diffraction peak as a function of creep time. ε_1 and FWHM_1 refer to the values at the beginning of creep..... 43

Figure 3-10 Schematic illustration of different definitions of strain rate during transient creep: (a) $\dot{\varepsilon}_{r,i} > 0$ and (b) $\dot{\varepsilon}_{r,i} < 0$ 44

Figure 3-11 Results of *in situ*/ *ex situ* stress reduction experiments with long creep times on NC Ni_35: (a) the schematic representation of the *in situ* experiments; (b) and (c) the evolution of the strain rate (black curve) and the peak broadening (blue curve) for the 60 min stress reduction tests performed at $\sigma_0 = 1.75$ GPa and $\sigma_0 = 2$ GPa with R values of 0.67 and 0.82, respectively. Also shown in (c) is the evolution of the strain rate (black open symbols) for a 165 hours creep period test with R value of 0.70. FWHM_{00} refers to the value at non-deformed state..... 45

Figure 3-12 Results of the standard *in situ* stress reduction tests series on NC Ni_65. Transient responses in dependence of R for $\sigma_0 = 1.5$ GPa: (a) the inelastic strain, and (b) the FWHM of {311} diffraction peak as a function of creep time. ε_1 and FWHM_1 refer to the values at the beginning of creep..... 46

Figure 3-13 For NC Ni_35 (solid symbols) and NC Ni_65 (open symbols), the normalized forward creep rate $\varepsilon_r/\varepsilon_0$ as a function of normalized stress σ_r/σ_0 is plotted on a semi-logarithmic scale. Each group of data is fitted by a sum of two exponential functions (dashed lines). The solid line represents the resulting fit..... 47

Figure 3-14 stress-strain curves of a conventional stress reduction test (black curve) and a continuous tensile test (red dashed curve) at the same loading rate: (a) NC Ni_35 and (b) NC Ni_65, both with $R = 0.87$ 48

Figure 3-15 Results from an *in situ* stress reduction experiment during compression on NC Ni_35: (a) the stress-strain curve and (b) the change of the FWHM with total strain. FWHM_{00} refers to the value at non-deformed state..... 48

Figure 3-16 The evolution of (a) the strain rate (black curve) and (b) the FWHM of {311} diffraction peak (blue curve) as a function of inelastic strain during transient creep. FWHM_{00} refers to the value at non-deformed state..... 49

Figure 3-17 A modified stress reduction experiment performed on NC Ni_35, in which a short creep period was inserted before the stress reduction so that the quasi-stationary state can be further approached: (a) the stress-time relation and (b) the stress-strain curve..... 50

Figure 3-18 The evolution of (a) strain rate and (b) the FWHM of {311} diffraction peak as a function of inelastic strain during transient periods. FWHM_{00} refers to the value at non-deformed state..... 51

Figure 3-19 Schematic representation of the evolution of strain rates during I. single transient creep in a conventional stress reduction test (blue dashed line) and II. repeated transient creep in a multistep test with each step ending near the creep rate given by the green dashed line. Black dot is the maximum forward strain rate after a large stress reduction. The pink curve is quasi-stationary line..... 51

List of Figures

- Figure 3-20 Schematic representation of a multistep test: after a large stress reduction, the applied stress is stepwise increased. In the present work, each stress level is held constant for 20 min followed by an increment of ~ 35 MPa per step..... 52
- Figure 3-21 Overview of transient behaviour as a function of inelastic strain for the *in situ* multistep tests performed on Ni_35 (a-c) and Ni_65 (d-f): (a, d) the stress-inelastic strain relation, (b, e) creep rates, and (c, f) the overall change of the FWHM for {200} and {311} peaks..... 53
- Figure 3-22 Overview of transient behaviour as a function of applied stress for the *in situ* multistep tests performed on Ni_35 (a-c) and Ni_65 (d-f): (a, d) creep rates, (b, e) and (c, f) decouple the overall change of FWHM for {200} and {311} peaks into contributions from 20 min creep periods (square symbols) and from stepwise stress increasing (circle symbols)..... 54
- Figure 3-23 (a) The evolution of creep rates as a function of stress for stress reduction tests performed on NC Ni_35 with $\sigma_0 = 2$ GPa (see Figure 3-11c). Pink circles: quasi-stationary flow stresses given by Figure 3-4. (b) Schematic of the evolution of the stress (upper) and the strain rate (lower) as a function of total strain in a stress reduction test. 55
- Figure 3-24 Results of standard *in situ* stress reduction tests series performed on NC Ni₅₀Fe₅₀. Transient responses depend on R for $\sigma_0 = 1.7$ GPa: (a) the inelastic strain, and (b) the FWHM of the {200} diffraction peak as a function of creep time. Three regimes can be distinguished. ε_1 and FWHM_1 refer to the values at the beginning of creep. 57
- Figure 3-25 Evolution of the inelastic strain and the change of the FWHM for {111}, {200} and {311} diffraction peaks during transient creep at $R \sim 1$: (a) NC Ni₅₀Fe₅₀, (b) NC Ni_65, and (c) NC Ni_35. ε_1 and FWHM_1 refer to the values at the beginning of creep... 58
- Figure 3-26 For NC Ni₅₀Fe₅₀, the normalized maximum forward strain rate $\varepsilon_T/\varepsilon_0$ is plotted logarithmically as a function of normalized reduced stress σ_T/σ_0 . All data points are fitted by a sum of two exponential functions (dashed lines). The solid line represents the resulting fit..... 58
- Figure 3-27 NC Ni₅₀Fe₅₀: (a) stress-strain curves for a conventional stress reduction test (black curve) and a continuous tensile test (red dashed curve) performed with the same loading rate. (b) shows the magnitudes of the overshooting plotted versus the amount of prior inelastic strain produced before reloading. The inelastic strain is normalized with respect to the strain produced at 1 GPa..... 59
- Figure 3-28 Overview of transient behaviour during the *in situ* multistep tests for NC Ni₅₀Fe₅₀: (a) the stress-inelastic strain relation; (b) and (d) creep rates as function of inelastic strain and applied stress; (c) the overall behaviour of the FWHM for {200} and {311} peaks as a function of the inelastic strain; (e) and (f) decouple the overall change of the FWHM into contributions from 20 min creep periods (square symbols) and from stepwise stress increasing (circle symbols), and display the change as a function of the applied stress..... 60

List of Figures

- Figure 3-29 Stress-strain curves of load-unload cycles and the corresponding evolution of grain size during/ after deformation measured from X-ray diffraction patterns: (a, b) for NC Ni₃₅, (c, d) for NC Ni₆₅, and (e, f) for NC Ni₅₀Fe₅₀..... 63
- Figure 3-30 Cross-section view of as-deformed NC Ni₃₅ with a total strain up to 20 %: (a) a bright field TEM image and (b) grain size distribution..... 64
- Figure 3-31 In-plane view of as-deformed NC Ni₃₅ with a total strain up to 20 %: (a) a bright field TEM image and (b) grain size distribution. 64
- Figure 3-32 Grain size distribution of non-deformed and deformed states presented in cumulative percent..... 65
- Figure 4-1 A simulated stress-strain curve for a NC Al sample deformed at room temperature at a constant strain rate of 10^8 /s..... 67
- Figure 4-2 (a) For the simulated stress reduction tests series, the trends of strain-time curves during creep periods are found to be R dependent and similar to those of *in situ* experiments. (b) After different magnitudes of the stress drops, the number of mobile dislocations propagating in the grain interiors decreases with decreasing R 68
- Figure 4-3 After a stress reduction with $R = 0.53$, one dislocation formed during prior deformation sits in the middle of one grain, see $t = 0$ ps. During subsequent creep, this dislocation continues propagating, e.g. $t = 4$ ps, until being absorbed at the GBs. The atoms are coloured based on CNA analysis, see Section 2.5.3. FCC atoms are not shown for simplicity. The black arrow indicates the propagation direction. 68
- Figure 4-4 Creep strain versus time curve for the additional stress reduction test with $R = 0.86$ followed by a creep period of 2290 ps. Each slip event in the grain is indicated on the curve. The insert presents G14 (centred) and its neighbouring grains. The viewing direction for G14 is perpendicular to the (-111) slip plane. Atoms are coloured based on CNA analysis..... 69
- Figure 4-5 Snapshots of a zoom-in of the rectangular region as indicated in Figure 4-4. The arrows indicate different dislocation and GB activity during creep. Atoms are coloured based on CNA analysis. 70
- Figure 4-6 Dis1-Dis2 interaction followed by a jog motion producing a vacancy inside the grain. The atoms are coloured based on atomic potential energy analysis. The potential energy ranges from -3.4 eV (blue) to -3.1 eV (red)..... 71
- Figure 4-7 Snapshots of a zoom-in of the circled region R1 as indicated in Figure 4-5: $t = 0$ ps and $t = 1315$ ps represent the configurations short after the stress reduction and at the time of a full emission of Dis1, respectively. The analysis of CNA and local hydrostatic pressure are applied. The red colour is representative for compressive stress field while blue for tensile..... 73
- Figure 4-8 After the stress reduction the shear strain at the GBs increases with creep time, and it is heterogeneously developed among the GBs. The colour bar scales the shear strain value ranging from 0 (white) to 0.2 % (dark blue)..... 73

List of Figures

- Figure 4-9 Snapshots of a zoom-in of the circled region R2 as indicated in Figure 4-5. The configurations short after the stress reduction ($t = 0$ ps), at the time of a full emission of Dis1 ($t = 1315$ ps), and at the time of Dis1 pinning ($t = 1340$ ps) and unpinning ($t = 2085$ ps) are compared in terms of atomic arrangement (CNA analysis). The atomic displacements (light blue) show the relative change between 1315 ps and 0 ps, 1340 ps and 1315 ps, and 2085 ps and 1340 ps, respectively. 74
- Figure 4-10 Upon Dis1 unpinning a ledge structure in the GB is removed. A viewing direction is perpendicular to the slip plane (-111). Atoms are coloured based on CNA analysis..... 75
- Figure 4-11 Snapshots on the zoom of the rectangular region as indicated in Figure 4-4. The configurations at time frames of $t = 400$ ps, 1315 ps, and 2085 ps are selected ; the atomic displacements show the relative change between 400 ps and 0 ps, 1315 ps and 400 ps, and 2085 ps and 1315 ps, respectively. The arrows mark the sites where long diffusion paths in the GBs occur. 76
- Figure 4-12 Local GB migration that occurs upon Dis2 nucleation and emission. The same region R2 as in Figure 4-7 is inspected. 76
- Figure 5-1 Transient behaviour of NC Ni₃₅ after the stress reductions: (a) the evolution of the strain rate as a function of the inelastic strain; (b) the corresponding change of the peak broadening. FWHM_{00} refers to the initial broadening prior to loading. The inset represents a zoom-in..... 80
- Figure 5-2 Schematic of the model describing forward and backward dislocation flow (red), and GB-mediated mechanisms (blue) for Regimes I-IV together with the corresponding evolution of strain contribution with creep time. 81
- Figure 5-3 CaF₂ that contains subgrain with (mainly) low-angle boundaries after prior deformation: (a) after a medium/large stress drop the inelastic strain rate during transient creep exhibits a non-monotonic change; (b) the total transient strain rate can be decomposed into contributions from two mechanisms [115]. 83
- Figure 5-4 A configuration prior to Dis1 emission: atoms in GBs are coloured according to CNA in (a) and shear strain analysis in (b)..... 84
- Figure 5-5 Once all grains have deformed, it is expected that GBs will receive dislocations with respective Burgers vector \mathbf{b}_1 and \mathbf{b}_2 to be absorbed from both sides. 86
- Figure 5-6 A zoom-in of the high- R region of Figure 3-13 as well as Figure 3-26. The relative contribution of the GB-mediated processes to the overall strain rate at the point of stress reduction can be obtained by extrapolating the linear slope $\varepsilon_r/\varepsilon_0$ fitted to the large and medium stress drops to $R = 1$, as indicated by the cross symbol..... 88
- Figure 5-7 The interplay between the FWHM of {200} diffraction peak and the inelastic strain in NC Ni₅₀Fe₅₀..... 90
- Figure 5-8 The total change of the peak broadening versus the total change of the inelastic strain generated during the creep periods of 30 min: FWHM_1 and ε_1 refer to the values at the start of the creep; $\text{FWHM}_{30\text{min}}$ and $\varepsilon_{30\text{min}}$ refer to the values measured at

List of Figures

- the end of the creep. The data points framed in the black squares were measured at a relative reduced stress $R = 1$. R decreases along the straight lines from the right side of plot to the left..... 91
- Figure 5-9 The evolution of normalized inelastic strain rate $\varepsilon_{inel}/\varepsilon_0$ as a function of inelastic strain generated during creep after stress reductions with $R = 1$ and $R = 0.9$: Ni₃₅ and Ni₅₀Fe₅₀ are respectively denoted as pink and blue symbols. 92
- Figure 5-10 Stress-strain curves of continuous deformation tests at different strain rates for NC Ni and NC NiFe [113]. 94
- Figure 5-11 Creep strain versus time curve for one test with a stress reduction of $R = 0.86$ followed by creep periods of 2290 ps..... 95
- Figure 5-12 The configurations of continuous deformation with and without stress reduction are compared when the same amount of strain is produced. The inspection is carried out in the same sections of GB 12-14 as studied in Figure 4-11, Figure 4-7, and Figure 4-9. 97

List of Tables

Table 2-1 Deposition parameters of NC Ni	13
Table 2-2 Structural parameters of as-received NC Ni determined by X-ray powder diffraction.....	13
Table 2-3 Structural parameters of as-received NC Ni ₅₀ Fe ₅₀ determined by X-ray powder diffraction.....	16
Table 2-4 The most important components at MS beamline layout.	24
Table 2-5 The classification of internal stresses and their influence on the peak profile (peak position, and peak width).	30
Table 3-1 Overview of all conventional stress reduction tests done on NC Ni batches.	42
Table 3-2 A modified stress reduction test in which the transient periods are composed of four different stress-controlled stages.	50
Table 3-3 Overview of all <i>in situ</i> conventional stress reduction tests done on NC Ni ₅₀ Fe ₅₀	56
Table 3-4 A comparison of average grain size between non-deformed and deformed state.....	64
Table 5-1 Comparison of the strain rate and the FWHM at the end of creep periods for a given stress in conventional stress reduction tests and a multistep test.	87
Table 5-2 Comparison of the number slip events and deformation time in continuous deformation with and without stress reduction when the same amount of strain is produced.....	97

List of Abbreviations

CG	Coarse-grained
CNA	Common Neighbour Analysis
CPMU	Cryogenically-cooled Permanent-Magnet Undulator
DCM	Double-crystal Monochromator
ED	Electrodeposited
EDM	Electrical-discharge Machining
FCC	Face-centered Cubic
FIB	Focused Ion Beam
FWHM	Full-width at Half-maximum
GB	Grain boundary
GBD	Grain Boundaries Dislocation
HCP	Hexagonal Close-packed
HRTEM	High Resolution Transmission Electron Microscopy
IW	Integral Width
LAMMPS	Large-scale Atomic/ Molecular Massively Parallel Simulator
MD	Molecular Dynamics
MEMS	Micro-electro-mechanical Systems
MS	Materials Science
MTM	Micro Tensile Machine
NC	Nanocrystalline
NEMS	Nano-electro-Mechanical Systems
OVITO	Open Visualization Tool
PID	Proportional-integral-Derivative
PSI	Paul Scherrer Institut
QCP	Quantized Crystal Plasticity
RMS	Root-mean-square
SAD	Selected Area Diffraction
SFE	Stacking Fault Energy
SLS	Swiss Light Source
TEM	Transmission Electron Microscopy
TJ	Triple Junction
UFG	Ultra-fine grained
UTS	Ultimate Tensile Strength
WH	Williamson-Hall
XRD	X-ray Diffraction

Chapter 1 Introduction

Nanocrystalline (NC) materials are defined as polycrystals with a grain size below 100 nm. Initial research interest in this class of materials originates from the pioneering work of H. Gleiter and co-workers [1]. Over the last three decades NC materials have witnessed an explosion of research interest, which is strongly related to their advanced mechanical properties. It has been reported that, as the crystallite size scales below 100 nm, NC materials exhibit enhanced strength/ hardness and increased strain rate sensitivity as compared to their coarse-grained (CG) counterparts (10-300 μm) [2].

Various NC metals have been suggested as potential candidates for applications, for instance, for the development of Micro-Electro-Mechanical Systems (MEMS) and Nano-electro-Mechanical Systems (NEMS). However their usage in real-life applications is currently rather limited. This is related to their limited ductility in tension, thermomechanical stability, time-consuming synthesis method, etc. In order to further develop and improve existing classes of NC metals a detailed understanding of the deformation mechanisms is therefore essential.

In NC metals, it is suggested that the very small scale of grain size limits the presence of dislocation sources inside grain interiors and largely reduces dislocation pile-ups. On the other hand, grain boundaries (GBs) start playing a more prominent role as their volume fraction increases significantly with decreasing grain size [3]. As a consequence, the Hall-Petch relation [4][5] in equation (1-1), a phenomenological scaling law that describes the relation between the yield stress σ_y , the friction stress σ_0 , and grain size d ,

$$\sigma_y = \sigma_0 + k_{H-P}d^{-1/2} \quad (1-1)$$

exhibits a different scaling coefficient k_{H-P} ($k_{H-P} > 0$) for grain sizes below 100 nm, and even breaks down ($k_{H-P} < 0$) below a critical grain size regime, typically around 10 to 20 nm [6][7][8]. It is therefore suggested that the deformation mechanisms change from conventional intragranular dislocation activity to GB mediated mechanisms. In Ref. [9], a maximum strength for NC Ni-W was observed in the regime of 10 to 20 nm; below that there is a crossover to glass-like deformation (i.e. shear banding) at finest grain sizes. To pin down the picture of plastic deformation in NC materials, a wide variety of techniques has been used, such as mechanical testing, X-ray diffraction (XRD), transmission electron microscopy (TEM), and computational modelling [10][11]. End of the nineties molecular dynamics (MD) simulations have proposed that during plastic deformation of NC materials GBs act as sources and sinks for dislocations [12][13][14], a model that has been verified by experimental technique [15] and which is now widely accepted. To date, many deformation mechanisms have been proposed, mainly characterized as dislocation-based processes and GB accommodation processes. The latter can involve GB sliding based mechanisms and GB migration such as migration coupled to shear stress.

There exist many different techniques to synthesize NC metals and alloys [10][16][17], such as mechanical alloying, inert gas condensation, electrodeposition, severe plastic deformation, and sputtering techniques. Electrodeposited (ED) NC samples are frequently used in studies because this technique can synthesize a

large variety of porosity-free NC metals with little size and shape limitations. On the other hand, ED NC samples exhibit large internal stress variations in their as-prepared state in comparison to CG and ultra-fine grained (UFG) materials. As suggested by previous investigations [16][18] this initial stored internal stress has an effect on their deformation behaviour.

1.1 Deformation mechanisms in nanocrystalline metals

Figure 1-1 presents a schematic picture of various possible deformation mechanisms in NC metals [19]. Dislocation-based mechanisms are presented in grains A-D and a-c, while GB-mediated accommodation in grains 1-4. In what follows the most important results from simulations and TEM/ HRTEM found in literature will be highlighted.

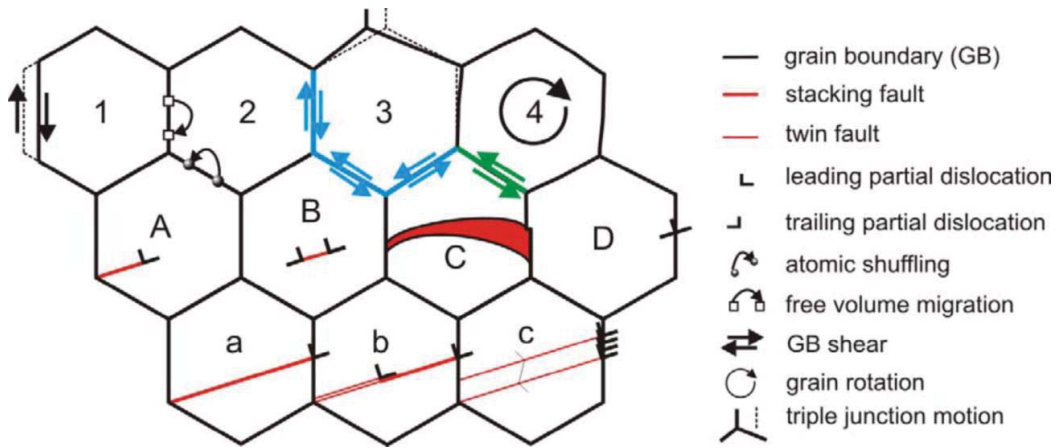


Figure 1-1 Deformation mechanisms in NC face-centred cubic (FCC) metals [19].

1.1.1 Dislocation-based mechanisms

Simulations

In NC regime, atomistic simulations demonstrate that dislocation activity involving dislocation nucleation, propagation, and absorption are mediated by dislocation-GB interaction. Refs. [12][13][14] have shown that a dislocation can be emitted from stress concentrations at GBs, travel through the entire grain, and eventually be absorbed at neighbouring and opposite GBs (see grain A-D in Figure 1-1). Whether partial or full dislocation activity is predominant within the nanosecond simulation time frame is determined by the ratio of the stable to unstable stacking fault energy (SFE) of the simulated material [20]. Also, it is proposed that under the condition of emitting a partial dislocation, the formation of a deformation twin is possible if the second partial of the same type as the first one is emitted on an adjacent slip plane (see grain a-c in Figure 1-1) [21][22]. During the propagation of a dislocation, GB ledges or misfit regions may act as obstacles; the pinning-unpinning process is thermally activated [23]. The subsequent work in Ref. [24] suggests that the pinning site can also be overcome via dislocation cross-slip. Note that dislocation activity as mentioned above changes the structural details of GBs.

Experiments

E. Ma and his co-workers performed uniaxial tensile tests on NC Ni (25 nm) at liquid-nitrogen temperature [25][26], capturing the trapped full dislocations in the grain interior as well as near GBs in post-mortem HRTEM. At ambient temperature, however, there is no clear evidence of dislocation debris by post-mortem investigations [27]. Mostly, dislocation-based processes in NC materials are revealed during *in situ* TEM deformation [28][29]. In Ref. [30], trapped dislocations in a 5 nm NC Ni grain were detected during *in situ* HRTEM straining; during a subsequent relaxation period these dislocations annihilated. In Ref. [31], L. Wang *et al.* observed the annihilation of dislocation dipoles as well as dislocations storage in the grain interior for a NC Ni with a grain size less than 10 nm. Moreover, deformation twinning in NC Al has been experimentally detected using HRTEM although Al has high stacking fault energy (SFE) [32][33][34]. Nevertheless, it should be noted that the dislocation behaviour observed by TEM/ HRTEM may not be active in bulk NC materials because the thinning process can change the microstructure and the large free surface with few grains longitudinally stacked may have a strong influence on the dislocation activity.

1.1.2 GB-mediated accommodation

Simulations

As mentioned earlier, it is expected that GB-mediated mechanisms become more important with decreasing grain size. The GB structures in Ni and Cu with grain sizes in the range of 5-12 nm were detailed analysed in Refs. [35][36]. The presence of highly structured GBs provides evidence against the view of being highly disordered, amorphous, or liquid-like interfaces. On the other hand, the results suggest the disordered regions in the GBs as candidates for playing a primary role in plastic deformation. To date, a variety of GB-mediated mechanisms have been studied by means of MD simulations (see grains 1-4 in Figure 1-1) including GB sliding (grain 3), GB motion (grain 1), triple junction (TJ) migration (grain 3), grain rotation (grain 4), and GB diffusion.

Refs. [12][37][38][39] show that GB sliding is the primary deformation mechanism for NC metals with grain sizes below 12 nm. Such GB activity is facilitated by atomic shuffling and stress-assisted free volume migration (see grain 2 in Figure 1-1) [39]. Since pure GB sliding is not fully compatible, it requires other cooperative processes such as GB motion and TJ migration, dislocation activity, and grain rotation to relieve the stress built up across neighbouring grains [40][41]. An alternative deformation mechanism is GB motion, which can contribute to grain growth during deformation. In Ref. [42], strain-driven GB migration (normal motion) was reported for NC Ni at room temperature, whereas in Refs. [43][44] GB migration coupled to shear deformation was observed. The latter is consistent with the early work done by A. Suzuki and Y. M. Mishin [45][46] on bicrystal configurations. In addition to GB motion, grain growth can result from grain rotation-induced grain coalescence [42][43][47] and GB diffusion as well. The latter, however, usually operates at high temperature and low rate [48]. Diffusion at room temperature can hardly be observed in MD simulation due to the restrictions of high deformation rates and short timescale.

Experiments

HRTEM experimental observations on NC Ni (30-40 nm) and Pd (5 nm) identified the crystallinity maintained in the GBs [28][49][50], suggesting GB structures of NC metals are similar to those in CG polycrystals. Direct experimental evidences of GB accommodation mechanisms, more often, are seen as grain coarsening during deformation [51][52][53]. In Ref. [54], K. Zhang *et al.* performed micro-indentation

tests on NC Cu (20 nm), detecting faster grain growth at cryogenic temperature than at ambient temperature. This result suggests that grain growth in this case is a stress-driven rather than a diffusion-driven mechanism. T.J. Rupert *et al.* [55] performed tensile tests on NC Al thin films (60-90 nm) that were specially designed with stress and strain concentrators, demonstrating that grain growth is driven more by shear stresses than by plastic strain. This result is supported by *in situ* TEM observations of ultrafast grain boundary motion in Ref. [56]. In contrast, strain-driven GB migration was reported by M. Jin *et al.* [57] during *in situ* nano-indentation tests. By performing high pressure torsion (HPT) on NC Ni (22 nm), R. Pippan and his co-workers [58] observed an increased extent of coarsening and softening with increasing applied stress, suggesting large strains and high stresses being required to induce grain growth. Additionally, grain rotation-induced grain coalescence upon *in situ* TEM tensile straining was observed for NC Ni with respective average grain size of 10 nm in Ref. [59] and 20 nm in Ref. [60].

1.1.3 Theoretical models of deformation

Composite model

The deformation behaviour of NC materials is often interpreted in terms of a composite model. The basic principle is to distinguish different responses of grain interiors and GBs regions when a material is subjected to an applied stress, and coupled these two in terms of their relative volume fraction varying with grain size. In literature, a variety of models [10] have been proposed which predict, for instance, the grain size dependent hardness and yield stress in accordance with experimental results.

In Ref. [61] Meyers-Ashworth model proposed that the plastic deformation is initiated in GBs regions at the localized stress concentrations arising from elastic incompatibility and dislocation sources in GBs. As the applied stress increases, these two effects combined with activated multislip at GBs lead to the formation of a work hardened GB layer that exhibits a faster rise in dislocation density. Further extension of this model to the NC regime was made by D.J. Benson *et al.* in Ref. [62]. Since GB sliding is not incorporated in this model, only a reduction of Hall-Petch slope with decreasing grain size is presented. Also, the validity of this model in NC regime is questioned: (1) an early formation of a work hardened GB in microplastic region is unlikely because only a fraction of grains are supposed to be deformed [8]; (2) the thickness of work hardened layer is largely dependent on the grain size, which is not addressed experimentally [28][49][50] as well as in MD simulations.

H.S. Kim *et al.* [63] developed a composite model: the deformation of the grain interior is modelled as being viscoelastic, involving both dislocation-based mechanisms and diffusion creep, whereas that of GB phase is modelled as a diffusional flow and independent of GB thickness. In this model, the dislocation mechanism cannot operate below a critical grain size, and the upper limit of the stress in GB is set to be equal to the strength of an amorphous phase. This model is consistent with a thermally activated GB shearing model below a critical grain size proposed by H. Conrad and J. Narayan [37]. Both interpret the breakdown of the Hall-Petch relation with decreasing grain size in terms of importance of GB sliding mechanisms.

R.J. Asaro and his co-workers proposed a model [64][65] that involves the dislocation-GB interaction, including mechanisms of the emission of perfect and partial dislocations, along with deformation twins from GBs, and GB sliding in the NC regime. By accounting for the grain size, strain rate, and temperature dependent transition between these mechanisms, this model interprets the increasing strain rate

sensitivity in NC FCC metals. Further extension of this approach was made by B. Zhu *et al.* [66], in which the effect of grain size distributions is incorporated, exhibiting good agreement with experimental data.

A quantized crystal plasticity model

The quantized crystal plasticity (QCP) model was proposed by L. Li *et al.* [67][68] where a key feature of grain-averaged shear strain/ stress jumps by discrete slip events in MD simulations was adopted. This model is characterized by four fundamental microstructural features: (1) anisotropic elastic moduli, (2) a grain orientation distribution, (3) a grain-to-grain distribution of critical resolved shear stress at which a slip event occurs, and (4) a grain-to-grain distribution of the local plastic strain jump by a slip event across an entire grain. Hence, the latter feature scales as $\sim 1/d$ (d : grain size). QCP model is capable of predicting the stress-strain response of NC metals as observed in the experiments, for instance, enhanced flow stress, extended plastic transition strain, and propensity for strain localization. Furthermore, their recent work in Ref. [69] has shown that QCP model can successfully reproduce the X-ray diffraction footprints of *in situ* experiments performed on NC and UFG Ni. In contrast to composite models mentioned above, QCP model does not incorporate deformation induced GB migration and GB sliding, the complex nature of TJs, and other detailed aspects, such as grain shapes and grain size distribution.

1.2 Nanocrystalline alloy

In comparison to pure NC metals, NC alloys have potential wider applications due to their increased thermal stability and grain size control. J. Weissmuller [70] and C.C. Koch *et al.* [71] have reviewed the grain size stabilization by solute additions. It is pointed out that further reduction in grain size can be achieved either through kinetic reduction of GB mobility, e.g. solute drag, or through a thermodynamic approach of lowering GB energy, i.e. solute segregation. By this means, the limit in refinement of single-phase materials by SPD processes can be overcome [72], for instance, a significant reduction in grain size from ~ 200 nm in Ni to ~ 100 nm in Ni-25wt%Fe alloy. On the other hand, electrodeposited NC Ni-W alloys with a large range of grain sizes down to the amorphous limit (3-150 nm) have been synthesized with W promoting grain refinement by J.R. Trelewicz and C.A. Schuh [9]. They found that in the regime of 10-20 nm the onset of the Hall-Petch breakdown corresponds to a minimum value for the activation volume. This result suggests that below this regime an increase of activation volume is associated with a mechanism shift to glass-like plasticity. However, in contrast to pure NC metals, the main issue with alloys is that the concentration of solutes in the grain interior and at the GBs is not constant when changing the grain size. As a consequence, the deformation mechanisms may be affected by this.

In CG alloys, it is known that the interaction of an alloying element with dislocations gives rise to an increased glide resistance, causing solid solution strengthening. For NC alloys, T.J. Rupert *et al.* [73] suggests that solute addition has an important effect on the global average elastic modulus as well due to a model of dislocation pinning at NC GBs. By combining both models, one can predict solute solution strengthening or softening for a variety of NC metals.

Furthermore, the addition of alloying can reduce the SFE of a material [74], and accordingly affect the strength of NC alloys as well as their deformation mechanisms. Experimentally, it is anticipated that at a relatively low SFE the emission of partial dislocations in terms of a leading and trailing partial will be favoured over a full dislocation and become dominant during plastic deformation.

1.3 *In situ* testing

1.3.1 *In situ* TEM

In contrast to post-mortem characterization, an *in situ* TEM/ HRTEM experiment provides an opportunity to observe dislocation and/ or GB activity that is active in NC metals upon straining. In literature, qualitative *in situ* TEM/ HRTEM have been performed in the works of [28][29][30][31][56][59][75][76][77][78][79].

To relate the direct evidence of deformation mechanisms to the stress-strain behaviour, quantitative *in situ* TEM testing on NC metals in terms of force and displacement measurement has been developed. This was driven by the pioneering work of M.A. Haque and M.T.A. Saif [80][81][82][83]. In Ref. [84], the new generation of the Haque-Saif device has been designed and applied for an *in situ* TEM study of microplasticity and Bauschinger effect in NC metals during load-unload experiments. Also, it is worth mentioning that H. D. Espinosa and his co-workers developed a different MEMS-based tensile testing stage, as was reported in Ref. [85]. To date, a growing number of MEMS devices have been invented, which enable different types of testing to be performed, for instance, *in situ* TEM tensile fatigue testing [86] and time-resolved HRTEM creep/ relaxation testing [87]. The latter was conducted on a novel lab-on-chip set-up developed by T. Pardoen and his co-workers. This set-up allows performing thousands of nanomechanical tests simultaneously without time consuming calibration procedures and sophisticated actuating/ loading devices [88][89]. Their tests performed on NC Pd films (30 nm) reported unexpectedly large creep rates at room temperature and dislocation-mediated relaxation behaviours that were derived from the evolution of dislocation density as well as twinning boundary thickness in HRTEM investigations [87].

Recently, a novel technique of combining automated crystal orientation mapping (ACOM) with *in situ* TEM has been developed and applied on NC/ sub-micro grained metals [90][91][92]. This technique enables a statistically quantitative evaluation of grain size distribution, crystal orientation and texture evolution during *in situ* plastic deformation, which can provide evidence for mechanisms of grain growth and rotation, and twinning/ detwinning.

1.3.2 *In situ* X-ray diffraction

The deformation processes during *in situ* TEM may not be always representative for bulk NC materials. *In situ* synchrotron X-ray measurements during deformation allow the investigation of the bulk mechanical behaviours of NC microstructures. Depending on the applied energy of synchrotron radiation, *in situ* experiments can be performed either in reflection or in transmission mode.

Medium energy X-ray diffraction in reflection geometry was used in Van Swygenhoven's group. The diffraction patterns collected by one-dimensional (1D) Microstrip detector provide the information on transverse lattice planes. The early work published in Ref. [15] revealed a reversible peak broadening during load-unload cycles of NC Ni. This result suggests a lack of permanent residual dislocation network after plastic deformation of a NC metal, and supports the suggestions from MD simulation that GBs act as dislocation sources and sinks. Similar *in situ* load-unload cycles were later performed at 180 K, evidencing no reversible peak broadening [93]. In Ref. [94] this type of mechanical testing was further utilized for the sake of studying different strain-hardening mechanisms in the micro- and macroplastic regimes. Other *in situ* mechanical testing, such as stress reduction (relatively mild stress drops) experiments followed by creep were reported in Ref. [95]. The signatures of the peak profile at different creep stress levels suggest

the presence of two competing deformation mechanisms with opposite effects on the diffraction peak width.

High energy synchrotron radiation permits high penetration depth, thus allowing applying transmission geometry in which the information of structure evolution on both longitudinal and transverse lattice planes can be obtained. In the meantime, the utilization of two-dimensional (2D) (area) detector records complete Debye-Scherrer rings, which allows monitoring the texture development and differentiating the types of mechanisms involved. In literature, this technique has been applied on the study of deformation behaviour of a bulk Ni-Fe alloy during uniaxial tension [53][96] and fatigue [97]. In Ref. [96], the investigation of the deflection of the lattice strain proposes that the initial localized deformation occurs in GBs regions. For NC Ni, the *in situ* uniaxial tension [98][99][100] and compression experiments [91] have been carried out. The latter suggests that the deformation in NC metals is governed by a succession of different, partly overlapping mechanisms.

1.4 Transient testing

Transient testing has proven to be a suitable tool to obtain information on rate limiting deformation mechanisms [101]. The basic principle behind such tests is to suddenly change the imposed deformation conditions during a monotonic test and evaluate the subsequent response of the material to these new conditions [101]. Here one assumes that the microstructure remains constant during the transient so that one is solely probing the effect of the rate sensitivity of the deformation mechanisms. Activation volume V and strain rate sensitivity m are two quantities that one frequently obtains from transient testing. They are respectively defined as

$$V = \sqrt{3}k_B T \left(\frac{\partial \ln \dot{\epsilon}}{\partial \sigma} \right) \quad (1-2)$$

$$m = \frac{\partial \ln \sigma}{\partial \ln \dot{\epsilon}} = \frac{\sqrt{3}k_B T}{V\sigma} \quad (1-3)$$

where k_B is the Boltzmann constant, T the temperature, $\dot{\epsilon}$ the strain rate, and σ the flow stress.

Overall, there are two main philosophies in transient testing: one is to conduct sudden changes in the strain rate, usually called strain rate jump tests [102][103][104][105], the other is to control the stress and conduct sudden changes in the applied stress, followed by a measurement of the stress relaxation [102][103][106][107][108][109] or the strain at constant stress [110][111][112]. Transient testing on FCC metals has revealed a strong grain size dependence on the V and m . For NC metals, as for instance NC Ni with an average grain size of the order of 30 nm, much lower V values of 10-20 b^3 than those of conventional forest dislocation cutting mechanism (on the order of 100-1000 b^3) as well as ten times higher m values of 0.011-0.02 have been measured in comparison to their CG counterparts [102][103][105]. Also, these V and m values are inconsistent with those expected for GB diffusion creep ($V \sim b^3$, $m \sim 1$) and GB sliding ($V = 1 b^3$, $m = 0.5$). Y.M. Wang *et al.* [103] performed transient testing on NC Ni over a range of temperature (77-373 K) and reported an inverse temperature-dependent behaviour, i.e. an increase of V with decreasing T . The authors suggest that the interactions of mobile dislocations with

1.5 Thesis outline

GBs such as nucleation, unpinning, and transmission are the rate controlling processes. Similar experimental observations were obtained by G. Guisbiers *et al.* performing relaxation tests on NC Pd film from 293 K to 323 K [109]. They propose a transition from dislocations-dislocations dominated interactions to dislocations-GBs dominated interactions. For Ni-Fe alloy, however, m value about one order of magnitude smaller than those for pure NC metals was reported in Ref. [113]. Reduced GB mobility by the alloying elements is suggested by G.J. Fan *et al.* [53].

Generally, strain rate jump tests need large magnitudes of plastic and anelastic strains to reach the new level of flow stress such that the condition of constant structure may be violated. In contrast, stress change tests can be performed relatively fast, as, in principle, only changes of elastic strain are required. In other words, the assumption of constant microstructure is easier to fulfil when transient is controlled by stress at very short times. Traditionally, stress change tests at constant temperature are focusing on three major goals: (1) determination of the activation volume of the dominant deformation mechanism by examining the relation between plastic strain rate and stress during the transient; (2) decomposition of the macroscopic stress into an effective (thermal) stress σ^* and an internal (athermal) stress σ_{ath} ; (3) identification of those deformation mechanisms that may play a minor role in the determination of the high value of the flow stress but might be essential to the development of a constant deformation resistance.

The study of dynamic recovery processes via a long-term stress reduction is based on the concept of the third goal. By performing a large stress drop, the thermally activated dislocation glide is suppressed enough so that dynamic recovery of defects can be brought into foreground and captured during the subsequent transient period. This technique has been early applied on single crystals [114][115] and CG polycrystals [116][117][118][119][120] that after prior deformation contained subgrains with (mainly) low-angle boundaries. These works reveal that it is low-angle boundaries that control the recovery processes as well as strength evolution during plastic deformation. In the present work, this technique will be applied on NC metals that have predominantly high-angle grain boundaries.

1.5 Thesis outline

It is known that NC metals exhibit rather limited ductility during uniaxial tensile deformation. On the other hand, much larger plastic deformation can be achieved during compression experiments, as illustrated in Figure 1-2. Note that in both deformation modes, the deformation curves are characterized by an initial hardening followed by a constant flow stress, whereas in CG counterparts a mild work-hardening regime extends over a large strain interval. As reported above there exists a large variety of possible deformation mechanisms in NC metals to explain the observed increased strength of NC metals. However, relatively little is known about the interplay between these mechanisms that lead to an early observation of plateau regime.

The main objective of this thesis is to develop a better understanding on the interplay between dislocation-based and GB accommodation mechanisms resulting in the development of a constant deformation resistance. The methods proposed are stress reduction experiments: after an intermediate/ large stress drop thermally activated dislocation slip is suppressed so that other underlying mechanisms will become visible during subsequent transient creep. Those mechanisms may play a minor role in the determination of the flow stress but might still be essential to the control of the strength evolution. The combination of such

tests with *in situ* synchrotron X-ray diffraction allows studying transient responses in terms of evolution of macrostrain as well as diffraction peak broadening. Since dislocation slip and GB accommodation have an opposite footprint on the peak broadening, the presence of these two types of mechanisms can be distinguished.

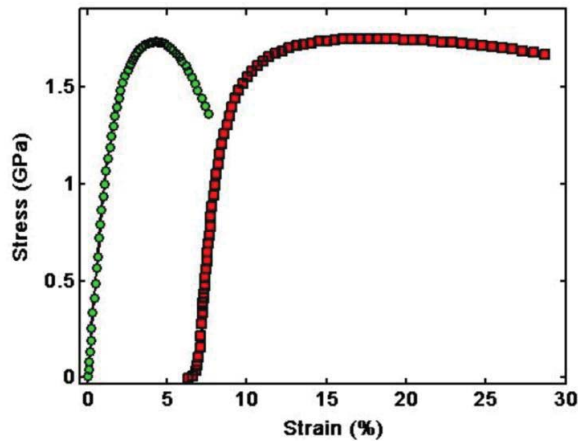


Figure 1-2 Stress–strain curves for a tensile test (green) and a compression test (red) in NC Ni

Figure 1-3 is a graph of thesis outline. Within this thesis, three electrodeposited NC materials with different grain sizes are investigated: two NC Ni batches and one NC Ni₅₀Fe₅₀ batch. The latter is the same batch as studied in Refs. [121][122][113]. The research is initiated by performing *in situ*/ *ex situ* continuous tests and *in situ* load-unload tests on NC Ni batches with the aim of obtaining their mechanical properties and comparing their results with former findings on NC Ni from Goodfellow [15][18][94][113]. On the other hand, by performing *in situ* load-unload tests on all materials, the grain size evolution during/ after tensile deformation is to be probed from X-ray diffraction patterns analysis. Complementary post-mortem TEM characterization is also implemented for the selected sample.

Stress reduction experiments are performed using *in situ*/ *ex situ* methods to follow the footprints of deformation mechanisms during transient creep. Tension and compression modes are both applied since the latter allows conducting stress reductions at larger deformation. In addition, to inspect the transient behaviour after a larger stress reduction, a modified method is developed where the reduced stress is stepwise increased. To further explore the effects of grain size as well as alloying on the interplay between dislocation-based and GB accommodation mechanisms, the results obtained for different batches are compared.

Finally, different magnitudes of stress reduction are carried out by molecular dynamics (MD) simulations so as to further understand the experimental results, in particular the interplay between different deformation mechanisms.

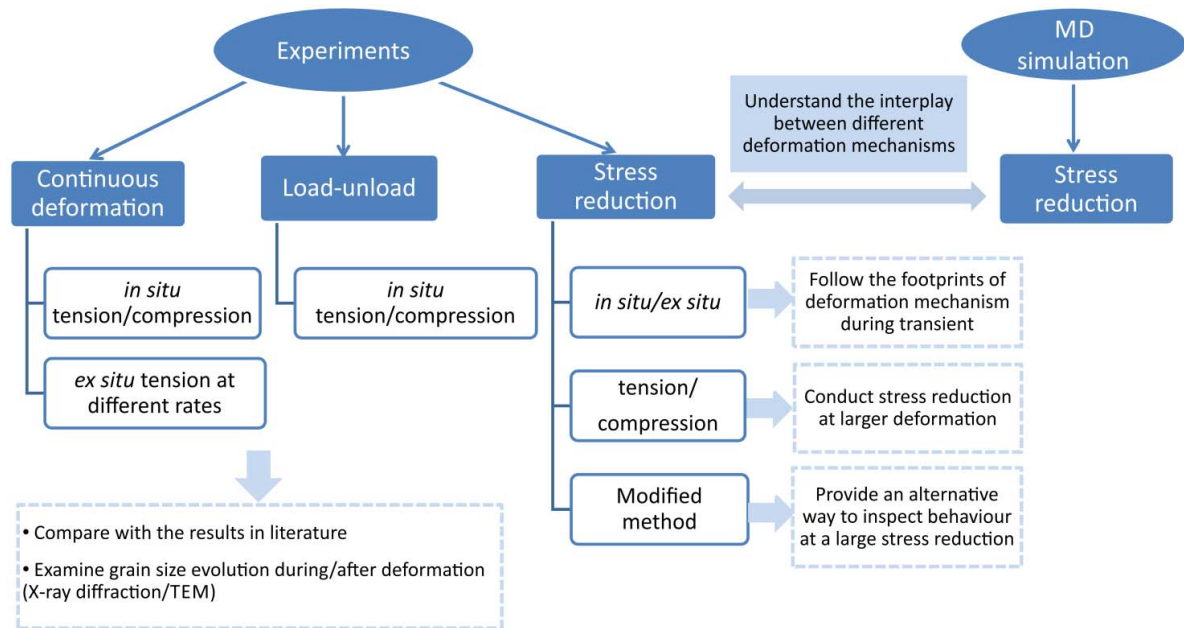


Figure 1-3 A graph of thesis outline

1.6 Thesis structure

The present thesis is divided into six chapters.

Chapter 2: introduces the experimental and technical details, including materials description, specimen preparation procedure, mechanical testing technique, *in situ* X-ray diffraction method, and MD simulations approach.

Chapter 3: presents the major results from experiments. First, the results of *in situ/ex situ* continuous deformation tests and *in situ* load-unload tests performed on two NC Ni batches are displayed. Afterwards, the results of stress reduction experiments are presented, first for NC Ni batches and then for Ni₅₀Fe₅₀. Finally, the evolution of grain size during/ after deformation is addressed.

Chapter 4: presents the results from MD simulations of stress reduction tests, which are composed of two parts. The first part aims to provide an overview of transient responses to different magnitudes of stress drop, showing the influence of applied stress on the transient behaviour. The second part focuses on one stress reduction test followed by a longer simulation time, for which dislocation and GB activity after the stress drop are detailed analysed.

Chapter 5: highlights the observations in Chapter 3 and Chapter 4, and elaborates them in terms of the interplay between dislocation-based and GB accommodation mechanisms. The discussion begins on one NC Ni batch followed by a comparison with another NC Ni batch so as to explore the grain size effect. Further discussion is held by comparing the results of NC Ni₅₀Fe₅₀ with those of NC Ni. The elaboration focuses on the peculiar behaviours of NC Ni₅₀Fe₅₀ in which both grain size and alloying effects are present. Finally, a brief comparison between present MD simulations and those reported for MD simulations at higher strain rates in literature is provided.

Chapter 6: summarizes the most important findings and provides the suggestions for unsolved issues and possible future directions of the work.

Chapter 2 Experimental and technical details

2.1 Materials description

2.1.1 NC Nickel

Two batches of NC Ni were synthesized by pulsed electrodeposition at the University of Erlangen-Nürnberg. Table 2-1 provides the deposition parameters. The main difference between the two batches is the saccharin content added for grain refinement. Under these conditions, it is well known that S, C and O impurities are present both in the grain interiors and at the GBs [28]. This technique is widely used to produce NC materials because it has the advantage of producing pore-free nanostructures. However, it generally leads to columnar grains along the growth direction [27][28]. In the deposition plane of grain growth the grains are equiaxed [28].

Table 2-1 Deposition parameters of NC Ni

Pulse current density	Pulse repletion rate	Duty cycle	Bath temperature	Electrolyte	Surfactant	Saccharin inhibitor
40 mA cm ⁻²	20 Hz	50 %	50 °C	Nickel sulphate (280 g/l), Nickel chloride (60 g/l), Boric acid (30 g/l)	Sodium dodecyl sulphate (0.2 g/l)	0.5 / 1.5 g/l

Table 2-2 displays their structural parameters obtained by X-ray powder diffraction (XRD) at the Swiss Light Source (SLS). The ratio of the integral intensities of the {111}/{200} diffraction peaks provides a measure for the texture. It is found that the intensity ratios for both are lower than that of a randomly textured FCC metal (~2), in agreement with the expected (100) out-of-plane texture. A measure of the average grain size and root-mean-square (RMS) microstrain is obtained by a Williamson-Hall analysis of the {111}-grain family. The NC Ni batches have average grain sizes of 35 nm (NC Ni_35) and 65 nm (NC Ni_65) and a similar RMS microstrain of ~0.3 %. It is noteworthy to mention that here the columnar length were measured by XRD.

Table 2-2 Structural parameters of as-received NC Ni determined by X-ray powder diffraction

Material	Ratio of integral intensities of the {111}/{200} diffraction peaks	Average grain size (nm)	RMS microstrain (%)
NC Ni_35	1.05, Mild (100) texture	35	0.32
NC Ni_65	0.35, Strong (100) texture	65	0.29

2.1 Materials description

The grain size distribution of as-received NC Ni is obtained by TEM characterization, performed respectively along the grain growth direction (cross-sectional view) and in the deposition plane (in-plane view), respectively. For NC Ni_35, the bright field images as well as grain size distributions are displayed in Figure 2-1 and Figure 2-2; for NC Ni_65, they are displayed in Figure 2-3 and Figure 2-4.

As seen in these bright field images, the determination of a clear grain structure is problematic. Firstly, the high internal strain field causes frequently changing black white contrast within the grains. Secondly, when the thickness of the TEM lamella is larger than the average grain size, it contains several overlapping grains. Within this thesis, a statistical evaluation of grain size was therefore performed on a series of dark field images that were taken by moving selected area diffraction (SAD) aperture along 111, 200, 220, and 311 rings, respectively. Extracting grain size information from those dark field images required subsequent image processing that were performed successively via GIMP and ImageJ software. In GIMP, the following procedures were followed: (1) created a transparent and a black layer (in invisible mode) on top of the imported image, (2) hand-traced the edge of each grain with the free select tool, (3) filled each grain with white colour. Once all grains have been outlined, the multi-layers were merged and fed into ImageJ for particle analysing where the grains were picked out by thresholding. Finally, the size of each grain was calculated as the diameter of a sphere with similar area as the original grain.

The results of TEM characterization are summarized as follows. Firstly, for both electrodeposited NC Ni batches, the grains are slightly elongated along the growth direction. The elongation direction is estimated by the yellow line in Figure 2-1a and Figure 2-3a. In contrast, the in-plane view shows rather equiaxed grains. Secondly, all grain size histograms obtained by TEM can be well fitted by log-normal distributions. It was found that NC Ni_35 has an out-of-plane and in-plane mean grain size of 29.2 ± 12.2 nm and 27.8 ± 12.0 nm, respectively, whereas for NC Ni_65 values of 53.2 ± 30.0 nm and 43.7 ± 22.4 nm are obtained. This shows that NC Ni_65 has a larger mean grain size as well as a broader size distribution. Additionally, it has been noted that for both batches the average grain size measured by TEM at the cross-section is slightly smaller than the columnar length measured by XRD. The assumption of a circular grain by TEM characterization can be one of the reasons for underestimating the columnar length.

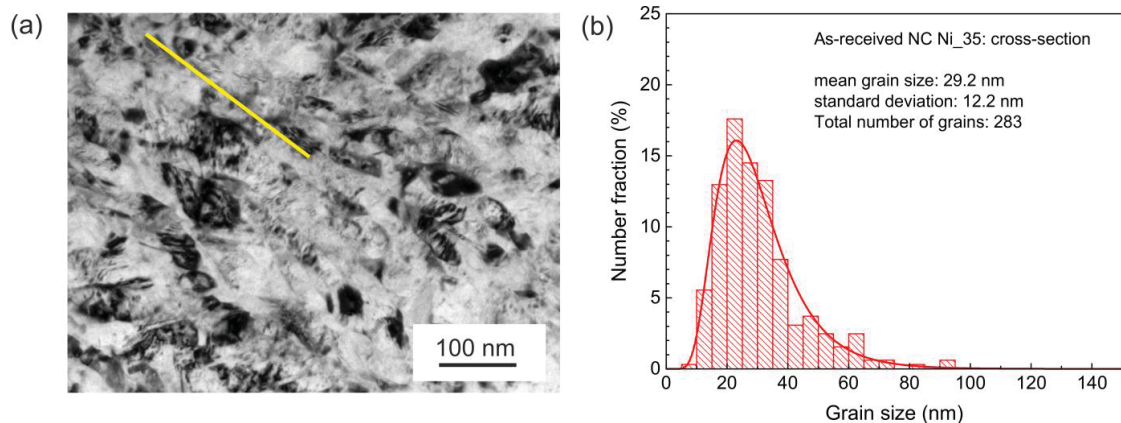


Figure 2-1 Cross-sectional view of as-received NC Ni_35: (a) a bright field TEM image and (b) grain size distribution.

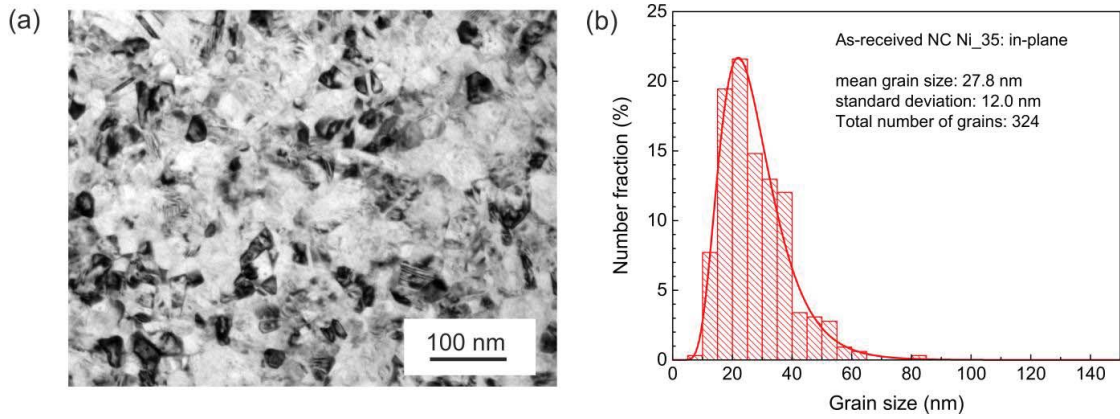


Figure 2-2 In-plane view of as-received NC Ni_35: (a) a bright field TEM image and (b) grain size distribution.

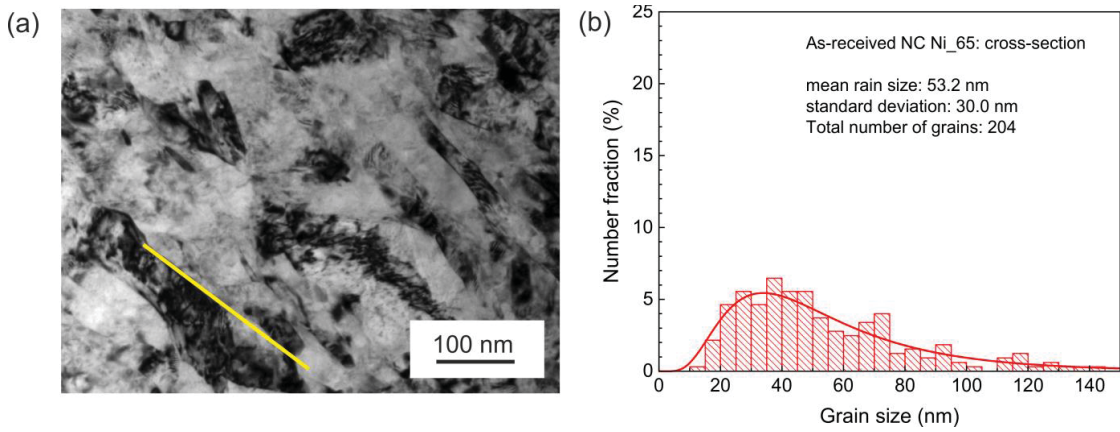


Figure 2-3 Cross-sectional view of as-received NC Ni_65: (a) a bright field TEM image and (b) grain size distribution.

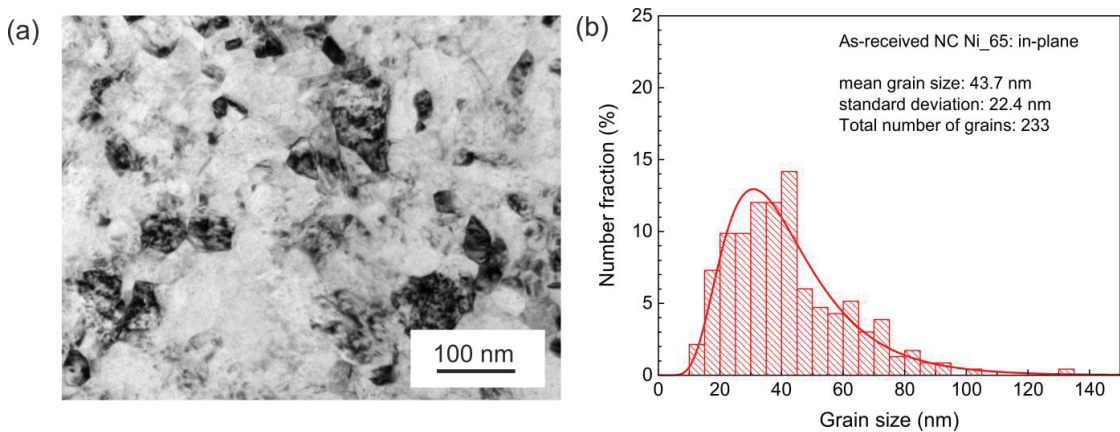


Figure 2-4 In-plane view of as-received NC Ni_65: (a) a bright field TEM image and (b) grain size distribution.

2.2 Specimen preparation

2.1.2 NC Ni₅₀Fe₅₀ alloy

NC Ni₅₀Fe₅₀ was purchased in sheet form from Integran Technologies. It has an face-centred cubic (FCC) crystal structure, where the Fe atoms are in solute solution in the Ni matrix. Table 2-3 provides structural information obtained from X-ray powder diffraction. It is observed that NC Ni₅₀Fe₅₀ exhibits a mild (100) texture, a rather small grain size of 15 nm and high RMS microstrain of 0.5%. A more in-depth characterisation for NC Ni₅₀Fe₅₀ can be found in Ref. [122].

Table 2-3 Structural parameters of as-received NC Ni₅₀Fe₅₀ determined by X-ray powder diffraction.

Material	Ratio of integral intensities of the {111}/{200} diffraction peaks	Average grain size (nm)	RMS microstrain (%)
NC Ni ₅₀ Fe ₅₀	0.85, Mild (100) texture	15	0.5

2.2 Specimen preparation

2.2.1 Mechanical testing

The specimens for mechanical testing were cut from the original bulk/ sheet materials by wire electrical-discharge machining (EDM). Although different sample geometries were used for tensile and compression tests, the loading directions are identical, which is perpendicular to the normal vector of the deposition plane. This is visualized in Figure 2-5a. Additionally, in order to remove the resulting recast-layer produced by EDM cutting, the resulting samples were further electro-chemically polished using a solution of 3% Perchloric acid (70%), 30% 2-Butoxyethanol, and 67% Methanol. This process was operated with a voltage of 15 V and a bath temperature of -15 °C. More detailed description can be found in Ref. [18].

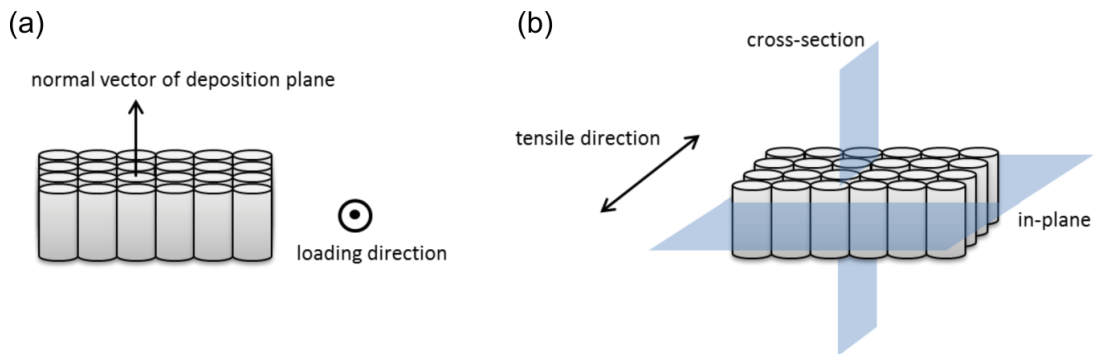


Figure 2-5 (a) During mechanical testing, the loading direction is perpendicular to the normal vector of the deposition plane. (b) For both non-deformed and deformed specimens, lamellae along the cross-section and in-plane direction were cut for TEM characterization.

2.2.2 TEM characterization

The specimens for TEM characterization were prepared by focused ion beam (FIB) thinning with a “lift-out” procedure. The primary advantage of this technique is that multiple TEM lamellae of well-defined areas (all orientations) can be directly made at the nanometre scale without sacrificing the entire specimen. This

becomes critical to miniature specimens studied in this thesis. Here, TEM characterization along the cross-section as well as in-plane direction was performed on both as-received NC Ni specimens and on a largely deformed NC Ni₃₅ specimen under compression.

The preparation procedure started with the deposition of a protective layer on the area of interest. In this thesis, a triple-layered deposition of carbon/platinum/carbon with a total thickness of 2 μm was utilized to protect the surface of the investigated material from being damaged by the incident Ga⁺ beam. After that the lamella was milled by FIB; different ion beam parameters were employed for different steps. Before a “lift-out” procedure, 30 kV·13 nA to 30 kV·3 nA were used for coarse milling and lamella-cutting. After being “lift-out” and welded to the Cu-grip, the lamella was thinned down step by step at gradually reduced current. The high currents provide fast milling while low currents increase milling precision. Once the wanted thickness has been achieved, usually between 80 and 120 nm, a final polishing of lamella was carried out at a lower voltage in order to minimize the amorphous layers generated during high-voltage milling.

2.3 Mechanical testing

2.3.1 Tensile testing

Machine and specimen geometry

All mechanical tensile tests were performed with a Micro Tensile Machine (MTM) [18][123][124], in which 3 mm mini dogbone-shaped specimens with a gauge length of 1.7 mm and a nominal cross-section of $0.2 \times 0.2 \text{ mm}^2$ were used. Figure 2-6a and b show the technical drawings of the MTM and the dogbone.

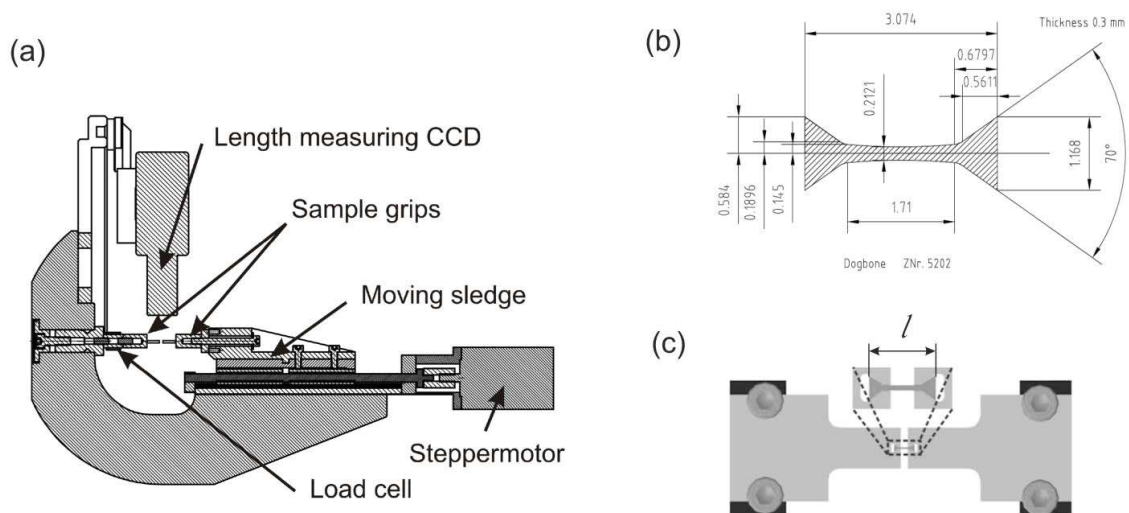


Figure 2-6 Technical drawings of (a) the micro tensile machine (MTM) [18]. (b) the mini dogbone-shaped tensile test specimen, and (c) the specimen grips [124].

2.3 Mechanical testing

During a tensile test, the dogbone is placed in the grips as shown in Figure 2-6c and is loaded via a moving sledge driven by a stepper-motor with minimum step size of 16 nm. During loading, the force measurement is done by a load cell (MLP50, Transduce Techniques) connected to one end of the left grip, and the length measurement of the dogbone is carried out with a CCD camera with back illumination. Thus, the specimen length l is measured as the distance between its two ends. In this method, the resolution of strain is limited to 0.01 %. More information on the MTM operation can be found in the thesis of S. Brandstetter [18].

Stress and strain

The calculation of the engineering strain ε_{eng} and engineering stress σ_{eng} is given by

$$\varepsilon_{eng} = \frac{\Delta L}{L_0}, \quad \Delta L = l - l_0 \quad (2-1)$$

and

$$\sigma_{eng} = \frac{F}{S_0}, \quad S_0 = W * H \quad (2-2)$$

Here, L_0 is the initial gauge length, a fixed value of 1.7 mm is used for a mini dogbone; ΔL is the elongation of the specimen, extracted from the difference between the actual length l and the initial length l_0 ; F is the measured force; S_0 is the initial cross-section, derived from the multiplication of specimen width W and thickness H that are both measured with a high precision micrometer.

Assuming a constant volume during deformation, the true strain ε and true stress σ defined by

$$\varepsilon = \int \frac{dL}{L} \quad (2-3)$$

and

$$\sigma = \frac{F}{S} \quad (2-4)$$

can be calculated from ε_{eng} and σ_{eng} using equations of

$$\varepsilon = \ln(1 + \varepsilon_{eng}) \quad (2-5)$$

and

$$\sigma = \sigma_{eng}(1 + \varepsilon_{eng}) \quad (2-6)$$

Here, S is the true cross-section. Note that Δl represents the length change of the whole dogbone, not of gauge section only. With other words, Δl also includes length changes in the ears of the dogbone. Even though this effect is relatively small (as the stress in the ears is much lower compared to the gauge section) it does lead to a significant underestimation of the Young's modulus. In the plastic regime deformation is localized at the gauge section and therefore Δl is less affected by this artifact.

Machine compliance

For transient testing, however, the inelastic strain ε_{inel} needs to be further extracted. It is composed as the sum of anelastic strain and plastic strain. There are a few methods of deducting elastic strain from the total strain ε_{tot} . One simple method is to apply the equation

$$\varepsilon_{inel} = \varepsilon_{tot} - \sigma/E_{app} \quad (2-7)$$

where E_{app} is the apparent elastic modulus comprising the contribution from the machine and the specimen. In this thesis, the term E_{app} as a function of force F , seen in Figure 2-7a, was determined by studying the slope of the stress-strain curve during the subsequent stress increases in the so-called multistep test (see also Section 3.2.3). In this test the stress is incremented in small steps. Here each step can be considered as elastic deformation with an apparent elastic modulus $E_{app} = \Delta\sigma/\Delta\varepsilon_{tot}$. In Figure 2-7b, the logarithm of $1/E_{app}$ is observed to be linearly proportional to the applied force F , thus an equation of

$$1/E_{app} = \exp(1/c_1 + c_2F) \quad (2-8)$$

can be derived with c_1 and c_2 as constants.

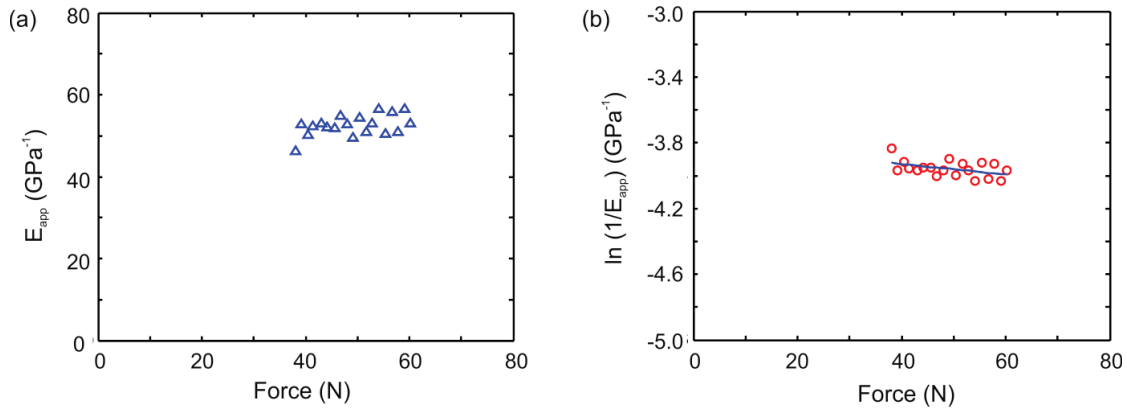


Figure 2-7 (a) E_{app} was determined as a function of force F from a multistep test. (b) The logarithm of $1/E_{app}$ is linearly proportional to the force F .

Further optimization of E_{app} is done by checking the stress versus inelastic strain curves for load-unload tests. In these tests the total stress-strain curve is seen as a mixture of elastic strain, anelastic strain, and forward plastic strain at high stresses. Figure 2-8a provides a qualitative picture for one load-unload cycle. In the unload cycle (red), it contains plastic forward flow at the beginning, elastic behaviour in the central part, and anelastic back flow behaviour at low stresses. During reloading (blue), the curve exhibits elastic behaviour in the beginning, anelastic forward flow during further loading, and finally plastic forward flow. Figure 2-8b shows the qualitative feature of the stress-inelastic strain curve, in which the elastic component has been subtracted. However, in practice a perfect correction is rather demanding and not

required. In compromise, a sufficient extent, e.g. 90 % correctness, is enough to improve the data presentation, in particular making the anelastic effect better visible.

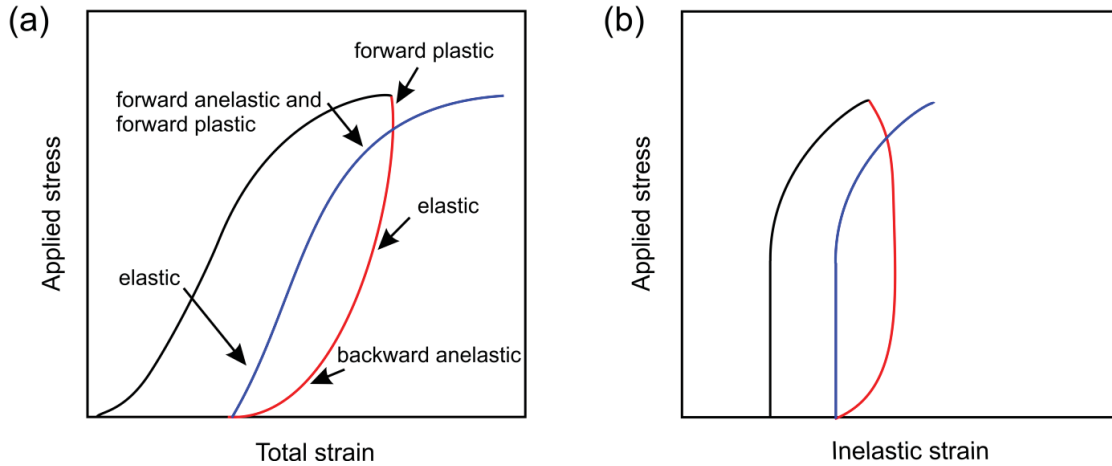


Figure 2-8 (a) A qualitative picture of stress versus total strain curve for a load-unload test. (b) Stress versus inelastic strain curve after subtracting the elastic component.

Strain rate

The inelastic strain rate $\dot{\varepsilon}_{inel}$ is determined from the derivative of the inelastic strain ε_{inel} with respect to time t , denoted as

$$\dot{\varepsilon}_{inel} = \frac{d\varepsilon_{inel}}{dt} \quad (2-9)$$

$$\dot{\varepsilon}_{inel,i} = \frac{\varepsilon_{inel,i+1}(t_{i+1}) - \varepsilon_{inel,i-1}(t_{i-1})}{t_{i+1} - t_{i-1}} \quad (2-10)$$

In this thesis, the calculations were performed on the treated data, which have been smoothed by the average software SmooMuDS [125][126]. This procedure allows eliminating the data noise and generating smooth $\dot{\varepsilon}_{inel}$ -curves.

2.3.2 Compression testing

Machine and specimen geometry

The compression tests were carried out with a deformation rig from Kammrath & Weiss (K&W), in which 1.1 mm cuboidal specimens with a gauge cross-section of $0.8 \times 0.9 \text{ mm}^2$ were used. Figure 2-9a and b display the technical drawings of the machine and the specimen. This specimen geometry was chosen by considering two main factors. First of all, the cross-section of specimen is restricted by the upper limit of the load cell (2kN) due to the extremely high flow stress of NC metals. Secondly, the specimen needs to be deformed to high plastic strains without buckling. This can be achieved by considering the following

constraint for the specimen aspect ratio $\kappa_0 = L_0/\sqrt{S_0} < 1.2 \sim 1.3$ (L_0 : initial gauge height, S_0 : cross section).

In order to handle this micro-sized specimen on the commercial K&W machine, the grips had to be redesigned. As shown in Figure 2-9a, the new grips system consists of a pair of carbide inserts and a pair of pressurizers wrapping outside. Compared with MTM machine, this device has a limited deformation speed ranging from 0.3 to 50 $\mu\text{m/s}$ and a larger step size.

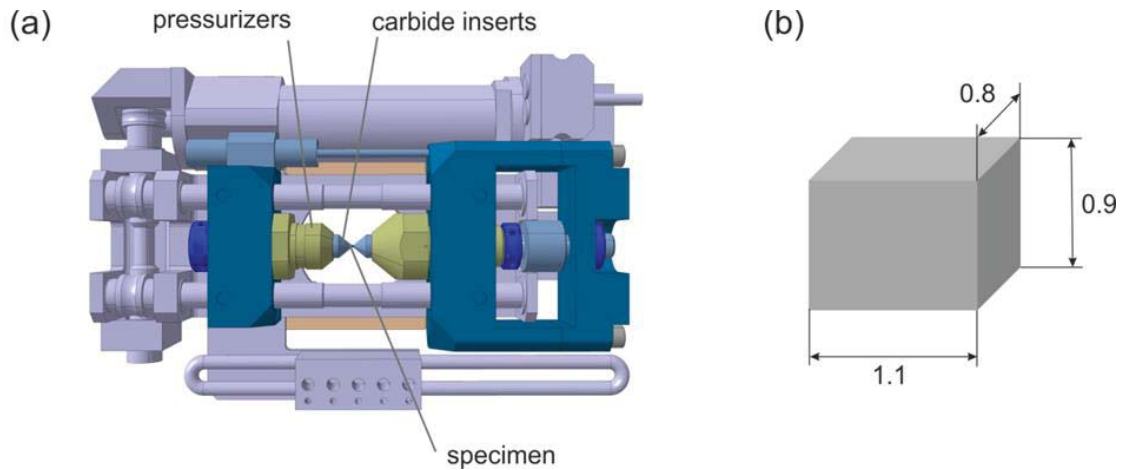


Figure 2-9 Technical drawings of (a) the micro compression machine (K&W) and (b) the cuboid specimen.

Friction correction

For the compression tests the same equations as for tensile testing were applied for the calculation of the stress and the strain, where now $\Delta L = l - l_0 < 0$. Considering the influence of friction at the contact surface between the specimen and the compression machine, the nominal true stress σ was corrected by multiplying with an empirical factor f [127]

$$f = (1 - \exp(-\kappa/c_3))^{c_4} \quad (2-11)$$

$$\kappa = \kappa_0 \cdot \exp(-1.5\varepsilon) \quad (2-12)$$

where c_3 and c_4 are the fitting constants, respectively taken as 0.4 and 0.5 that were reported for steel in Ref. [127]. In this thesis, this factor decreases slightly from 0.975 to 0.954 as ε increases in the interval from 0.05 to 0.2 where all change tests have been done.

The sticking friction at the end of surface of the specimen does influence the fracture tendency. However, when the specimen is deformed near to the quasi-stationary state, its influence on the hindrance of deformation during compression is expected to be negligible. The argument is that: when the resolved shear stress is high enough, the dislocations glide on the activated slip planes, and transfer stress to their environment by local relaxation. As a result, the neighbourhood also starts deforming by dislocation

motion, and the whole volume of the specimen deforms at approximately equal rate by stress redistribution.

2.3.3 Stress reduction operation mode

In this thesis, transient testing via stress reduction was carried out during constant strain rate deformation. Figure 2-10 is a schematic representation of such a transient test, which consists of constant strain rate, stress dip, and constant stress mode. Each specimen is first strained to a pre-defined stress σ_0 at a constant loading rate. Then upon reaching σ_0 the applied stress is suddenly reduced to a new stress level σ_r , followed by a certain period of creep. The ratio between both stress levels is denoted by the relative reduced stress $R = \sigma_r / \sigma_0$.

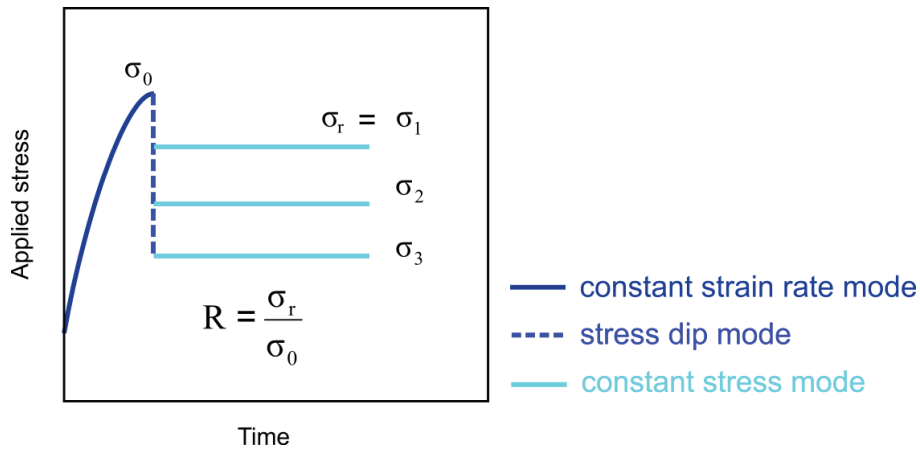


Figure 2-10 Schematic representation of transient testing via stress reduction during a constant strain rate test.

The operation of stress reduction on MTM machine is realized in the following way: at a pre-defined stress σ_0 , the crosshead is moved backwards at very high speed (opposite to the loading direction) by a certain distance and stopped; then the average of the stress value σ_r is determined immediately and it is kept constant via a proportional-integral-derivative (PID) controller in a LabView program.

Such an operation on K&W machine is done via motor control, from which constant strain rate deformation in “manual mode” can be switched to creep deformation in “load constant mode”. In this latter mode, the machine will achieve the input load value in a way defined by the control parameters P , v_{min} , and v_{max} . P is regulator sensitivity, increased for fast reaction and decreased for invert reaction. v_{min} and v_{max} are the minimum velocity and maximum velocity for regulation.

2.4 X-ray powder diffraction

2.4.1 Fundamental principle

The fundamental principle of X-ray powder diffraction is based on the constructive interference that is produced by the interaction of monochromatic X-ray beams with crystalline structures when a simple geometrical relation Bragg's law is fulfilled. This law is described by the equation

$$n\lambda = 2d_{hkl} \sin \theta_{hkl} \quad (2-13)$$

where n is the reflection order, λ the X-ray wavelength, d_{hkl} the lattice spacing of (hkl) planes, and θ_{hkl} the diffraction angle that is half of the (hkl) peak position $2\theta_{hkl}$.

Peak profile analysis yields information on peak broadening, peak position, peak intensity, and peak asymmetry, which allows furthering examination of defects, grain size and internal strain. More details about the data treatment will be illustrated in Section 2.4.4 and Section 2.4.5.

2.4.2 Material Science Beamline at the SLS

The Swiss Light Source (SLS) at the Paul Scherrer Institute (PSI) is a third-generation synchrotron light source operated at energy of 2.4 GeV. In this thesis, all *in situ* mechanical experiments were performed at the powder diffraction station (PD) of the materials science (MS) beam line at the SLS.

Compared with conventional laboratory sources, synchrotron X-ray beams (energy resolution $\Delta E/E \sim 10^{-4}$) have high collimation and monochromaticity that improve the angular resolution of the acquired patterns, and high brilliance that reduces measurement times by several orders of magnitude. The latter allows researchers studying the dynamics of samples on the timescale of seconds.

The MS beamline underwent an upgrade in late 2010. The original wiggler source was replaced with a cryogenically-cooled permanent-magnet undulator (CPMU). The CPMU produces divergent radiation and allows accessing to high photon energies from the storage ring. Also, in order to adapt to the new X-ray source, the entire front-end and optics at MS beamline were redesigned. Figure 2-11 schematically displays the most important beamline components. Their abbreviations are briefly illustrated in Table 2-4. In Figure 2-11a, as it can be seen, the conversion of white beam (in purple) to the monochromatic beam (in yellow) is operated through the optics lying between 20 and 31 m. Figure 2-11b is a schematic of new optics set-up, in which the two mirrors are downstream of a double-crystal Si (111) monochromator (DCM). The powder diffractometer (PD) is positioned at 32.8 m with respect to the centre of the CPMU (U14). Compared with wiggler source, the improved brilliance from the CPMU resulted in an order of magnitude improvement in diffraction intensity, whereas the increased transverse coherence lengths opened up the possibility of performing coherent diffraction imaging in the Bragg geometry. More details on the design of upgraded MS beamline are published in a technical paper [128].

2.4 X-ray powder diffraction

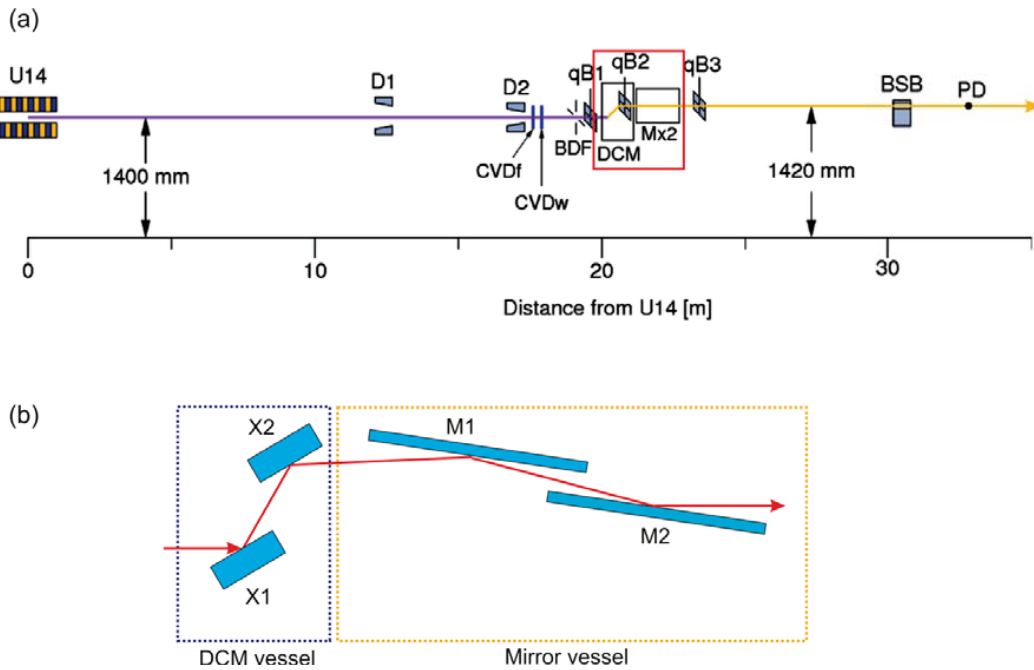


Figure 2-11 (a) Block diagram of the positions of the most important beamline components, the abbreviations of which are briefly illustrated in Table 2-4. The white beam is shown in purple, and the monochromatic beam in yellow. (b) A schematic of the optics set-up (reproduced from [128]).

Table 2-4 The most important components at MS beamline layout.

Abbreviation	Component
U14	U14 CPMU
D1,D2	diaphragm 1,2
CVDf	CVD diamond filter: absorbs soft X-rays
CVDw	CVD diamond window: vacuum protection for front-end
BDF	Beam-defining slits
qB1(2,3)	Three quadrant CVD-diamond beam position monitors
DCM	Double-crystal monochromator
Mx2	Double mirror chamber
BSB	Bremsstrahlung blocker: protection against Bremsstrahlung originating in the storage ring
PD	Centre of powder diffractometer

2.4.3 *In situ* experiments

Experimental setup

All *in situ* experiments were carried out with MTM or K&W at the powder diffraction station at MS beamline. Figure 2-12 and Figure 2-13 provide an overview of the *in situ* setups for tension and compression mode. In each case, the machine is mounted on a goniometer that provides two translations

and one rotational degree of freedom. For the MTM the conventional setup as described in Ref. [124] was used. For the K&W deformation rig a specific holder had to be designed, as shown in Figure 2-13a and b.

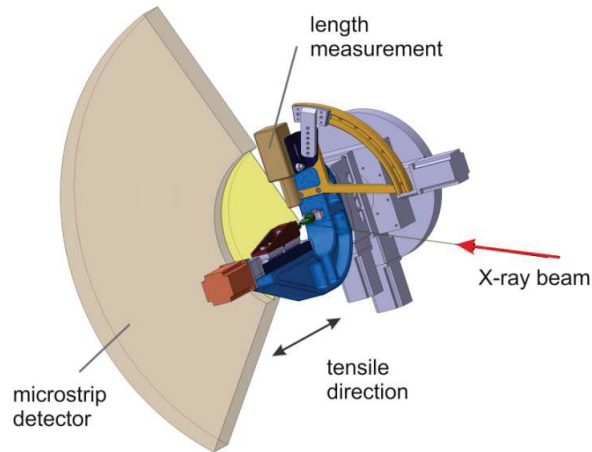


Figure 2-12 *In situ* tensile deformation apparatus at the MS beamline.

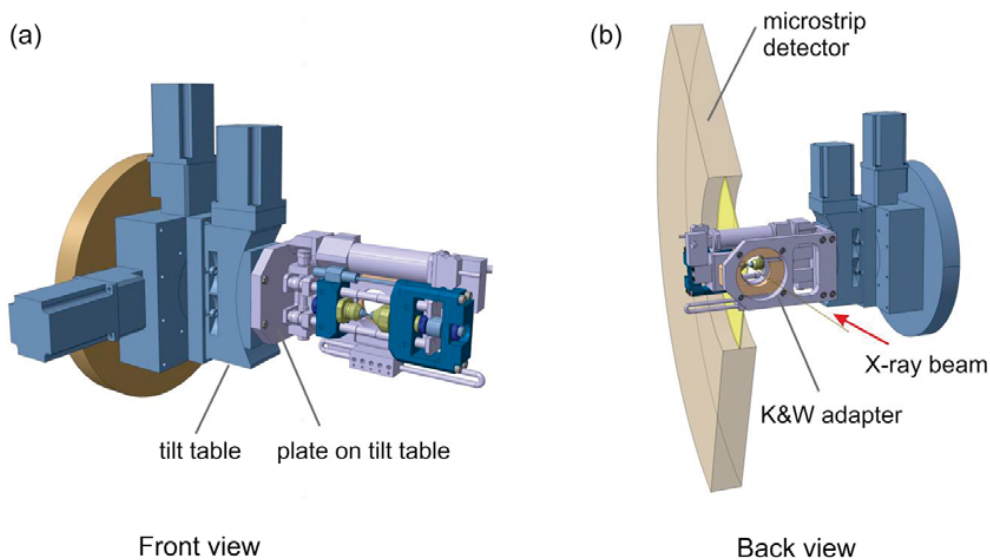


Figure 2-13 *In situ* compression deformation apparatus at the MS beamline: (a) front view, and (b) back view at the connection between K&W machine and goniometer.

During *in situ* deformation, the machine has a fixed position and the specimen is continuously deformed and illuminated by the incoming monochromatic X-ray beam. The diffracted beam is acquired with a one-dimensional position-sensitive multistrip detector MYTHEN. This detector is designed for time-resolved experiment, allowing continuous measurement of X-ray diffraction patterns spanning 120° with an angular

resolution of 0.0039° . In the thesis, the typical acquisition times for one full diffraction spectrum is 10 s. More details on the detector can be found in Refs. [128][129].

Diffraction geometry

Figure 2-14 displays the scattering geometry used in this work. Here the angle between the incoming X-ray beam and a specimen is fixed. In such geometry, a grain initially contributing to a diffraction peak may lose its diffraction condition during loading. Figure 2-14a represents a non-deformed state, of which grain 1 and grain 3 respectively fulfil the Bragg condition for the (111) plane and (400) plane. Once a force perpendicular to the viewing plane is applied on the specimen, the corresponding change of the lattice spacing (e.g. due to poisson response) alters the Bragg diffraction condition. Under the condition of tension, the lattice spacing is reduced as illustrated in Figure 2-14b. As a result, grains 2 and grain 4 now contribute to the (111) and (400) peaks respectively, and shift peak position towards larger angle. An opposite change is seen in compression, in which diffraction peaks shift towards smaller angle due to an increase of the lattice spacing. Consequently, a large amount of grains need to be illuminated in order to have a constant number of grains that fulfil the Bragg equation during deformation. This necessary condition is usually fulfilled for specimens with grain sizes below 1 μm . More information on this topic can be found in Refs. [18][123][124].

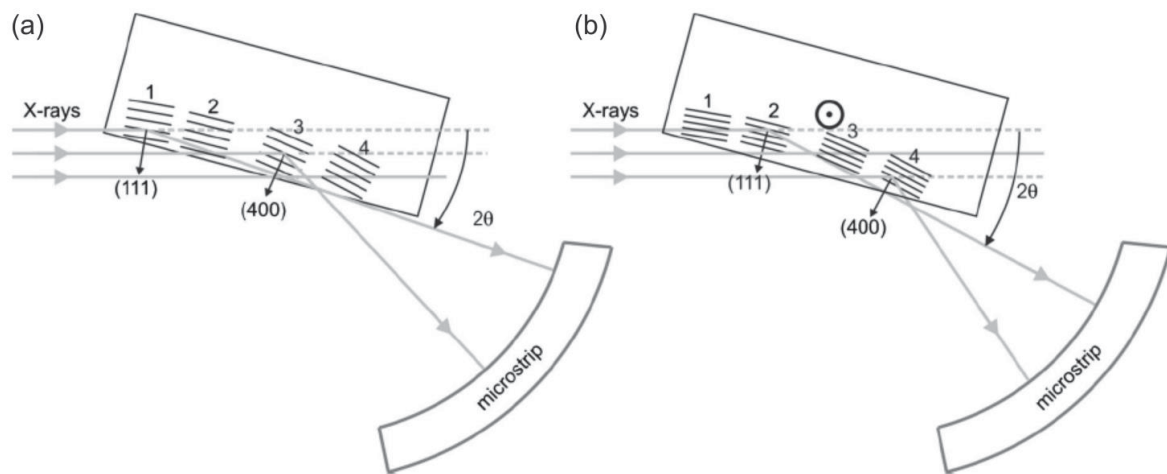


Figure 2-14 The scattering geometry for X-ray diffraction: (a) before deformation, and (b) under tension.

Additionally, this diffraction geometry endows each set of lattice planes $\{hkl\}$ being diffracted with a unique direction of scattering vector. This can lead to bias in the estimation of grain size when a Williamson-Hall (WH) analysis on the $\{111\}$ -grain family is performed (see also Section 2.4.5). Figure 2-15a demonstrates this issue schematically. The scattering vectors for the $\{111\}$ and $\{222\}$ grain family are not parallel to each other. As a consequence, they probe along different directions in the grains. When the grains are not equiaxed along this direction this may lead to a wrong estimation of grain size and RMS strain. This can be avoided by performing two measurements, during which the sample is rotated such that the scattering

vectors of the two grain families are parallel to each other (Figure 2-15b). For the WH analysis cited within this thesis the second procedure was used. Here 50 diffraction patterns were recorded for each alignment of the sample in the beam.

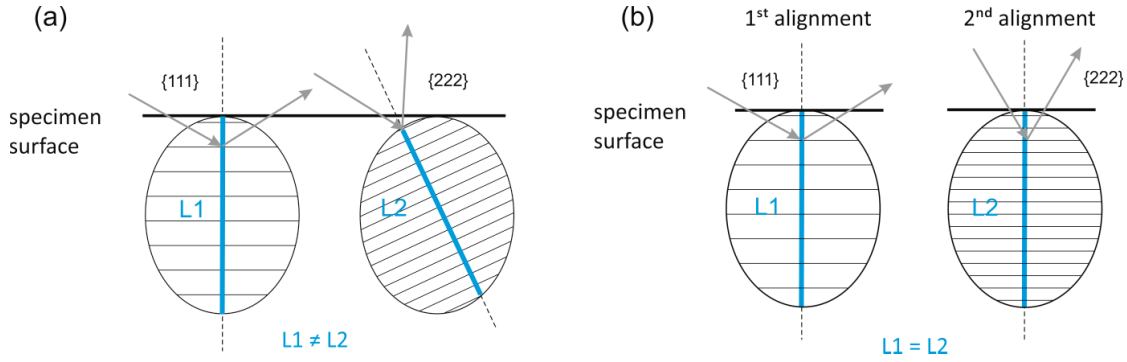


Figure 2-15 A schematic illustration of grain size measurement during *in situ* deformation: (a) under the condition of a fixed angle, the estimation of coherent scattering length (seen as grain size) from Willison-Hall analysis use {111} and {222} diffraction peaks that differ in the direction of scattering vector. (b) After the alignment of the scattering vector in the same direction, the accuracy of measurement can be improved.

Resolution function

The resolution function is associated with the instrumental broadening determined by beam size, specimen geometry, and diffraction angle. In the case of tensile test on MTM machine, a mini dogbone-shaped specimen is fully illuminated by incoming beam due to its small cross-section, as shown in Figure 2-16a. Thus, the width of the diffracted beam w_d is estimated by

$$w_d = W \sin(2\theta - \alpha) \quad (2-14)$$

where W is the specimen width, θ the diffraction angle, and α the angle between incoming beam and the specimen. In the case of compression test on K&W machine, the specimen geometry is relatively large so that the width of the diffracted beam w_d is determined by the beam size (typically a few hundred micrometres), as shown in Figure 2-16b. The aforementioned equation (2-15) can be rewritten as

$$w_d = W_{beam} \sin(2\theta - \alpha) \quad (2-15)$$

where W_{beam} is the illuminated size on the specimen.

Thus, the width of the diffracted beam w_d increases with increasing diffraction angle and W or W_{beam} . Fortunately, the peak broadening for NC materials with grain sizes of a few tens of nanometers is at least one order of magnitude larger compared to the resolution function. Therefore its contribution is ignored in this work [124].

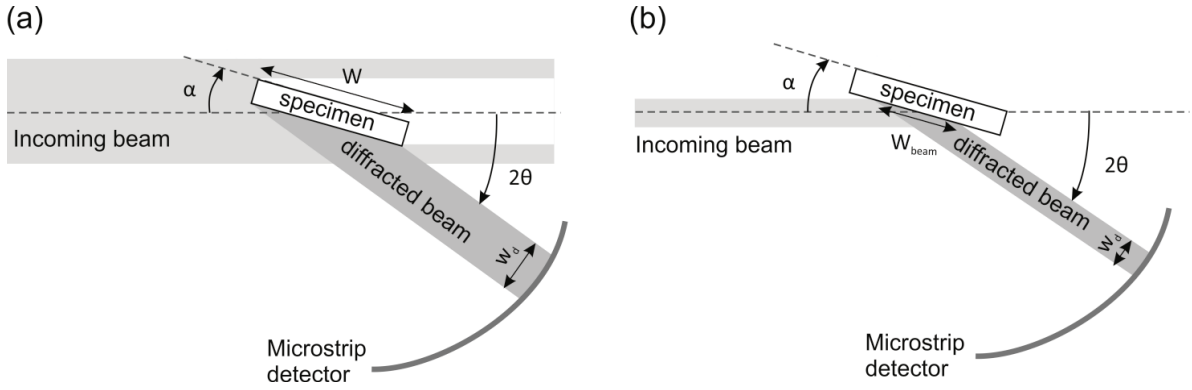


Figure 2-16 Influence of the specimen geometry on the instrumental broadening: (a) a typical case for a mini dogbone-shaped specimen used in MTM, and (b) a typical case for a cuboid specimen used in K&W. This figure is reproduced from Ref. [123].

2.4.4 Peak profile fitting

The raw data recorded from powder diffraction is stored in terms of diffracted intensity versus diffraction angle 2θ . For each full spectrum, freestanding peaks of {111}, {200} and {220} are fitted separately; {311} and {222} peaks with peak position close to each other are fitted in a 2-peak model. In this thesis, a split Pearson-VII function plus a linear function as background is applied for peak profile fitting. This function has following analytical shape:

$$P(\theta) = H_{peak} \left[1 + (2^{1/M_R} - 1)(10^{-\beta} + 1)^2 \left(\frac{\theta - \theta_0}{w} \right) \right]^{-M_R} \quad \text{if } \theta \geq \theta_0 \quad (2-16)$$

$$P(\theta) = H_{peak} \left[1 + (2^{1/M_L} - 1)(10^{-\beta} + 1)^2 \left(\frac{\theta - \theta_0}{w} \right) \right]^{-M_L} \quad \text{if } \theta < \theta_0 \quad (2-17)$$

where θ is the diffraction angle, θ_0 the angle corresponding to peak maximum, H_{peak} the peak height, w the full-width at half-maximum (FWHM), β the asymmetry parameter, and M_R and M_L the left and right decay exponents, respectively. For $M_{R,L} \rightarrow \infty$ the Pearson-VII tends to a Gaussian profile; for $M_{R,L} = 1$ it resembles a Cauchy (Lorentzian) profile. Further information on the peak profile fitting can be found in paper[18][124].

2.4.5 Extracting structural parameters

Grain size and RMS microstrain

For a diffraction peak at a certain angle 2θ , size and strain broadening are two main factors that determine the peak width. In this thesis, Williamson-Hall method is utilized, allowing separating the individual contributions of these two based on their different dependence on the diffraction angle θ .

The size broadening $\delta\theta_{size}$ arises from incomplete cancelling of small deviations from the Bragg angle θ , and can be described by the formula:

$$\delta\theta_{size} = \frac{\lambda}{L_{coh} \cos \theta} \quad (2-18)$$

Here, L_{coh} is the coherent scattering length that is parallel to the diffraction vector.

The strain broadening $\delta\theta_{strain}$ is caused by a distribution of lattice spacing. It can be denoted by the RMS strain $\langle \varepsilon^2 \rangle^{1/2}$, i.e. the variations around the average strain. The $\delta\theta_{strain}$ is written as

$$\delta\theta_{strain} = 4e \tan \theta \quad (2-19)$$

Here, e is an upper limit for the inhomogeneous strain. The commonly used value $\langle \varepsilon^2 \rangle^{1/2}$ equals to $4e/5$.

The aforementioned equations with the peak position and the peak width in diffraction angle θ can be further converted in terms of the scattering vector s

$$s \equiv \frac{2 \sin \theta}{\lambda} \quad (2-20)$$

that is independent of the photon energy E ($E = hc/\lambda$, Planck's constant h , speed of light c).

The resulting size broadening is rewritten as

$$\delta s_{size} = \frac{1}{L_{coh}} \quad (2-21)$$

and strain broadening as

$$\delta s_{strain} = 2es \quad (2-22)$$

It is noted that size broadening in equation (2-21) is independent of scattering vector s , whereas strain broadening in equation (2-22) is linear proportional to s value. To separate the size and strain contributions from the total peak broadening δs_{total} a Cauchy-Gaussian method is utilized in this thesis. It is assumed that the functional shape of Bragg peak profiles induced by size broadening is described by a Cauchy distribution whereas strain broadening exhibits a Gaussian profile [130][131]. Thus, δs_{total} is given by the convolution of these two contributions and can be written as:

$$\delta s_{total} = \delta s_{size} \left(\frac{\exp(-(\delta s_{size}/\delta s_{strain})^2/\pi)}{1 - \operatorname{erf}\left(\sqrt{2/\pi} (\delta s_{size}/\delta s_{strain})\right)} \right) \quad (2-23)$$

where the $\operatorname{erf}(x)$ is defined by

$$\operatorname{erf}(x) \equiv \frac{1}{\sqrt{2\pi}} \int_0^x e^{-t^2/2} dt \quad (2-24)$$

This relation can be approximated as

$$\frac{\delta s_{size}}{\delta s_{total}} = 1 - \left[\frac{\delta s_{strain}}{\delta s_{total}} \right]^2 \quad (2-25)$$

2.4 X-ray powder diffraction

with an error of at most 10 % according to Ref. [132]. By resubstituting equations (2-21) and (2-22) it results in

$$\left[\frac{\delta S_{total}}{s}\right]^2 = 4e^2 + \frac{1}{L_{coh}} \left[\frac{\delta S_{total}}{s^2}\right] \quad (2-26)$$

By plotting $\left[\frac{\delta S_{total}}{s}\right]^2$ versus $\left[\frac{\delta S_{total}}{s^2}\right]$ in a linear fit, one can obtain the coherent scattering length L_{coh} from the slope $1/L_{coh}$ and the RMS strain $\langle \varepsilon^2 \rangle^{1/2}$ from the intercept $4e^2$.

It is suggested that the Williamson-Hall analysis should be applied on the peaks from the same diffraction family due to a directional strain field caused by defects, such as dislocations. In this thesis, {111}-grain family was selected. Other methods of extracting the size and strain contribution, such as Warren-Averbach method can be found in Refs. [130][131].

Internal stresses in relation to peak profile

Based on the length scales of grain size, the internal stresses in polycrystalline materials can be distinguished into three types: macrostress σ_I , intergranular microstress σ_{II} , and intragranular microstress σ_{III} . Plastic deformation during *in situ* X-ray diffraction allows following the evolution of these internal stresses. Table 2-5 provides a description of each stress type as well as its influence on the X-ray diffraction profile, in particular in terms of peak position and peak broadening. Moreover, by following the change of peak position and peak broadening during deformation, one can obtain the information on structure evolution. The details are explained in the paragraphs below.

Table 2-5 The classification of internal stresses and their influence on the peak profile (peak position, and peak width).

Internal stress types		Definition	Influence on peak profile	
			Peak position	Peak broadening
σ_I , Type I	Macrostress	Homogeneous over a very large number of crystal domains	√	
σ_{II} , Type II	Intergranular microstress	Reflects average stress variations from one grain to another	√	√
σ_{III} , Type II	Intragranular microstress	Reflects the inhomogeneous stress within a grain		√

Evolution of lattice strain

According to Bragg's law, the peak shift during *in situ* loading reflects the change of lattice spacing. For a given crystallographic direction hkl , the resulting lattice strain ε_{hkl} can be derived from

$$\varepsilon_{hkl} = \frac{d_{hkl} - d_{0,hkl}}{d_{0,hkl}} \quad (2-27)$$

Here $d_{0,hkl}$ is the reference value before applying the stress.

By substituting equation (2-13) in equation (2-27), ε_{hkl} in units of microstrain is written as

$$\varepsilon_{hkl} = -\cot(\theta_{hkl}) \Delta\theta_{hkl} \times 10^6 \quad (2-28)$$

where $\Delta\theta_{hkl}$ is the deviation of the peak position θ_{hkl} from the reference value. In the elastic deformation regime, the lattice strain is linearly proportional to the applied stress; as soon as the plastic deformation sets in, it will deviate from linearity. Depending on the deflection direction, one can obtain the information of load transfer among the grains for a single-phase material [133].

Evolution of peak broadening

In this thesis, the usage of different definitions for the diffraction peak width is case dependent. For grain size and RMS microstrain analysis, the integral width IW is used as it is defined in Williamson-Hall method. In the case of *in situ* deformation, the evolution of peak broadening is presented in terms of the FWHM, the usage of which is to be consistent with literature. In addition, FWHM data exhibits less noisy than the IW because the statistical error of the latter comes from both integral area and the peak intensity. The FWHM in terms of scattering vector s is written as

$$\delta s_{hkl} = 2 \cos \theta_{hkl} \delta\theta_{hkl} / \lambda \quad (2-29)$$

where $2\delta\theta_{hkl}$ is the measured FWHM in units of rad.

The interpretation of peak broadening can be described as follows:

- For small-grained materials, the peak broadening is a convolution of multiple contributions. The most important ones are: (1) the coherent scattering length that is related to the grain size, twin density, and stacking fault density, and (2) elastic strain variations that are either caused intragranularly by defects (for instance dislocations) in the grain interior or intergranularly by inhomogeneous strains among the grains.
- During an *in situ* continuous loading, the evolution of peak broadening is a net balance between multiple contributions. On the one hand, the peak width is expected to increase when defects (such as dislocations, twins etc.) are involved or when different grains experience an increasing different average stress. It was shown by L. Li *et al.* that in NC Ni the signature of the evolution of intergranular strain conforms with dislocation slip [69]. On the other hand, GB-mediated mechanisms play an important role in the recovery of defects as well as internal stresses, which leads to a reduction of the diffraction peak width [95]. In addition, a decline of peak width may be ascribed to an increase in coherent scattering length when deformation mechanisms such as grain coarsening or detwinning are triggered during loading [52][54][91][134][135][136].

2.5 Molecular dynamic simulations

2.5.1 Molecular dynamics

MD involves the solution of Newton's equation of motion for an N-atom system:

$$m_i \ddot{\tilde{r}}_i(t) = F(\tilde{r}_1, \dots, \tilde{r}_N) = -\tilde{\nabla}_i V(\tilde{r}_1, \dots, \tilde{r}_N) \quad (2-30)$$

where m_i is the atomic mass, F the acting force on the atom, \tilde{r}_i the position of the i^{th} atom, and V the potential energy. Since the precise atom dynamics is governed by N non-linearly coupled differential equations, a numerical approach involving the discretisation of time is employed to evolve the system through time. For example, by approximating the acceleration via a simple finite difference representation one obtains

$$m_i \frac{[r_i(t + 2\Delta t) - 2r_i(t + \Delta t) + r_i(t)]}{\Delta t^2} = -\tilde{\nabla}_i V(r_1(t), \dots, r_N(t)) \quad (2-31)$$

from which a new configuration at time $t + 2\Delta t$ can be derived from the previous configurations at time $t + \Delta t$ and t . To integrate, the Gear predictor/ corrector integrators [137] is used. Such finite-difference or integrator methods generally employ a time-step of the order of a femto-second. The initial velocities of the atoms are assigned according the desired temperature T using the principle of equipartition of energy:

$$\frac{3N}{2} k_b T = \frac{1}{2} \sum_i m_i \dot{\tilde{r}}_i \cdot \dot{\tilde{r}}_i \quad (2-32)$$

Here, k_b is the Boltzmann constant. More details on the MD simulation algorithm can be found in Ref. [137].

2.5.2 Simulation procedure

MD simulations of stress reduction were performed on a NC Al sample (Al17) that contains 15 randomly orientated grains with an average grain size of 12 nm ($\sim 10^6$ atoms) in an orthonormal simulation box of the initial size $27.5 \times 27.5 \times 27.5 \text{ nm}^3$. The actual MD simulation work was carried out with Large-scale Atomic/ Molecular Massively Parallel Simulator (LAMMPS) code [138][139] by Dr. Christian Brandl in Karlsruhe Institute of Technology. The initial sample was geometrically constructed using the Voronoi procedure [140] under full 3D periodic boundary conditions. This procedure produces a log-normal grain size distribution as reported for experimental results, however, creates an energetically unfavourable GB network and local GB structures, which are subsequently locally relaxed by molecular statics, i.e. molecular dynamics with a quenching condition, and equilibrated for 100 ps at zero pressure MD [14] at 300 K temperature by the Nose-Hoover thermostat throughout all dynamic simulations. In the past, this configuration has been studied extensively in terms of its deformation behaviour under monotonic loading [23].

Sample consideration

Due to the restrictions of the simulation timescale, the selection of aforementioned simulation box size is a compromise between various opposite considerations:

- Having enough grains for intergranular accommodation activity.
- Having large enough grain size for observing dislocation activity.
- Having long enough creep periods for observing the transient responses.
- Several stress reduction tests with different magnitudes of stress drops to be carried out.

Additionally, Al was chosen instead of Ni, as in Ni predominately only leading partial dislocation activity is observed within the timescale of the simulations. In Al the emission of full dislocations has been observed

[20]. The embedded atom method (EAM) potential for Al of Y. Mishin *et al.* [141] was used here to model the interaction between atoms.

In general, much higher applied stresses (2-3 times higher) and strain rates ($> 10^7$ /s) in MD simulation facilitate dislocation activity and limit the role of GB accommodation mainly to the mechanically driven processes. Also, note that the simulated sample typically lacks transgranular and intergranular internal stresses that typically prevail on length scale exceeding the grain size, and lacks impurities as well [142]. Nevertheless, relatively short-ranged (fraction of the grain size) intragranular internal stress by the GBs and triple junction extend into the FCC grain. With this in mind the MD simulation offers a model system that provides more details regarding to deformation mechanisms and defect interaction at the atomic scale rather than reproducing the experimental results obtained by macroscopic *in situ* experiments.

The simulations were performed at a temperature of 300 K where the sample was subject to a uniaxial tensile load along *z* axis. In the course of the simulation, a time-average procedure is generally used to improve the atomic visualization due to thermal fluctuations. In Ref. [23] a time interval of 250 fs was chosen because it is slightly larger than the typical vibration period of an atom. Within this thesis, an alternative method to suppress thermal fluctuation was applied for the analysis: the instantaneous configuration at the required simulation step was quenched by viscous damped dynamics for 250 fs. Since the average lattice constant at 300 K was maintained virtually in a 0 K configuration in the method, i.e. the volume and box shape was kept constant, the overall pressure (trace of the stress tensor) has changed with the imposed temperature by quenching.

2.5.3 Analysis techniques

The output dump files generated by LAMMPS were analysed via the open-source software Open Visualization Tool (OVITO) [143][144] in PSI.

Common neighbour analysis

Common neighbour analysis (CNA) [145] is an effective filtering method to classify atoms based on their local crystalline structural environment. Figure 2-17 displays a cell structure of NC Al sample where FCC atoms are coloured grey, hexagonal close-packed atoms (HCP) red, and other coordinated atoms blue. One can identify structure defects such as GBs, stacking faults, and twins. The presence of a stacking fault is identified by two consecutive {111} planes of HCP atoms and a twin fault by only one single {111} HCP plane.

Displacement vectors

The displacement vector modifier in OVITO calculates the displacement vectors of each atom by subtracting its position in the reference configuration from that of current configuration. All the atomic positions need to be mapped into the same simulation box before this calculation due to the macroscopic, homogeneous deformation of the simulation cell. By eliminating this artificial shift, the calculated vectors reflect only the internal, microscopic displacements of atoms.

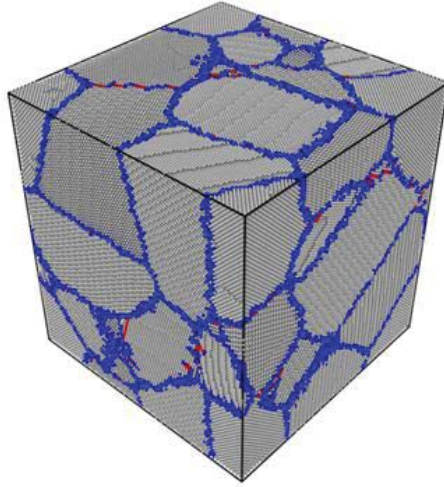


Figure 2-17 A cell structure of the constructed sample, in which atoms are coloured via CNA analysis.

Local hydrostatic pressure

Within MD simulations the virial theorem has been generally used to calculate the global stress tensor, which is in the limit of a large volume and a large number of atoms and represents the bulk homogeneous stress [146]. In order to inspect the spatial variance of the stress field within the sample, the virial theorem will be applied directly to each atom. In the present work, the momentum conserving representation developed by J. Cormier *et al.* [147] was utilized to compute the local stress quantities. A volume element around each atom with radius of 4 Å was chosen (as was done in previous investigations [19][23][146]). In the past work [19][23][146], it has been shown that the local hydrostatic pressure is a sensitive indicator for GB structural changes once dislocation activity occurs, such as emission, pinning, and absorption.

Local shear strain

The atomic strain modifier calculates the atomic-level strain tensors based on two configurations of the system: the current configuration with respect to the reference configuration. This requires the same operation of eliminating homogeneous cell deformation as that done for displacement vector in the beginning. After that the local deformation gradient tensor for each particle is calculated from the relative displacements of the atom's neighbours within the given cut-off radius. In this thesis, local von Mises invariant computed by OVITO was utilized to inspect the local shear strain [148].

Chapter 3 Experimental Results

3.1 Plastic deformation of nanocrystalline Nickel

This section reports on *in situ* continuous deformation and load-unload experiments performed on two NC Ni batches, allowing a comparison with previous studies performed on NC Ni obtained from Goodfellow [15][18][94].

3.1.1 *In situ* continuous deformation

Tensile tests

Continuous tensile testing during *in situ* X-ray diffraction was carried out at room temperature with a strain rate $\dot{\epsilon}_{tot}$ of 6×10^{-5} /s.

For NC Ni_35, the mechanical data and *in situ* data are displayed in Figure 3-1a-d. Figure 3-1a shows the stress-strain curve, evidencing first a pronounced strain hardening followed by a constant flow stress before necking. The dashed line is a linear fit in the elastic regime. Due to the length calibration issue in instruments and machine compliance (discussed in Section 2.3.1), the Young's module measured is smaller than the theoretical value of 200 GPa. Figure 3-1b shows the lattice strain as a function of the applied stress. {111}, {200}, {220} and {311} grain families are along the transverse direction. Figure 3-1c shows the deviation from linear behaviour (shown as dashed lines in Figure 3-1b). These deviations are clearly grain family dependent, indicating a load transfer up to 1.4 GPa. At higher stresses, due to elastic anisotropy the softer {200} grain family exhibits a tensile shift, whereas some other grain families go into compression, in particular for {220} grain family. Figure 3-1d displays the corresponding evolution of the FWHM for all grain families. It is evident that the FWHM remains constant up to 0.6 GPa and shows a strong increase when the specimen is loaded to higher stresses.

For NC Ni_65, the mechanical and *in situ* data are displayed in Figure 3-1e-h. The corresponding stress-strain curve in Figure 3-1e demonstrates the same characteristics but a lower value of ultimate tensile strength (UTS). The deviation from linearity is more pronounced in all grain families, with a remarkable tensile deflection of the {200} family after a stress level of 0.6 GPa (see Figure 3-1g). This stress value seems to be also the lower limit for observing a change in FWHM that increases with applied stress (Figure 3-1h).

Figure 3-2 presents the evolution of the FWHM for all grain families as a function of total strain for both batches. Compared with the stress-strain curve, the increase in FWHM is stagnating when the flow stress reaches the maximum.

3.1 Plastic deformation of nanocrystalline Nickel

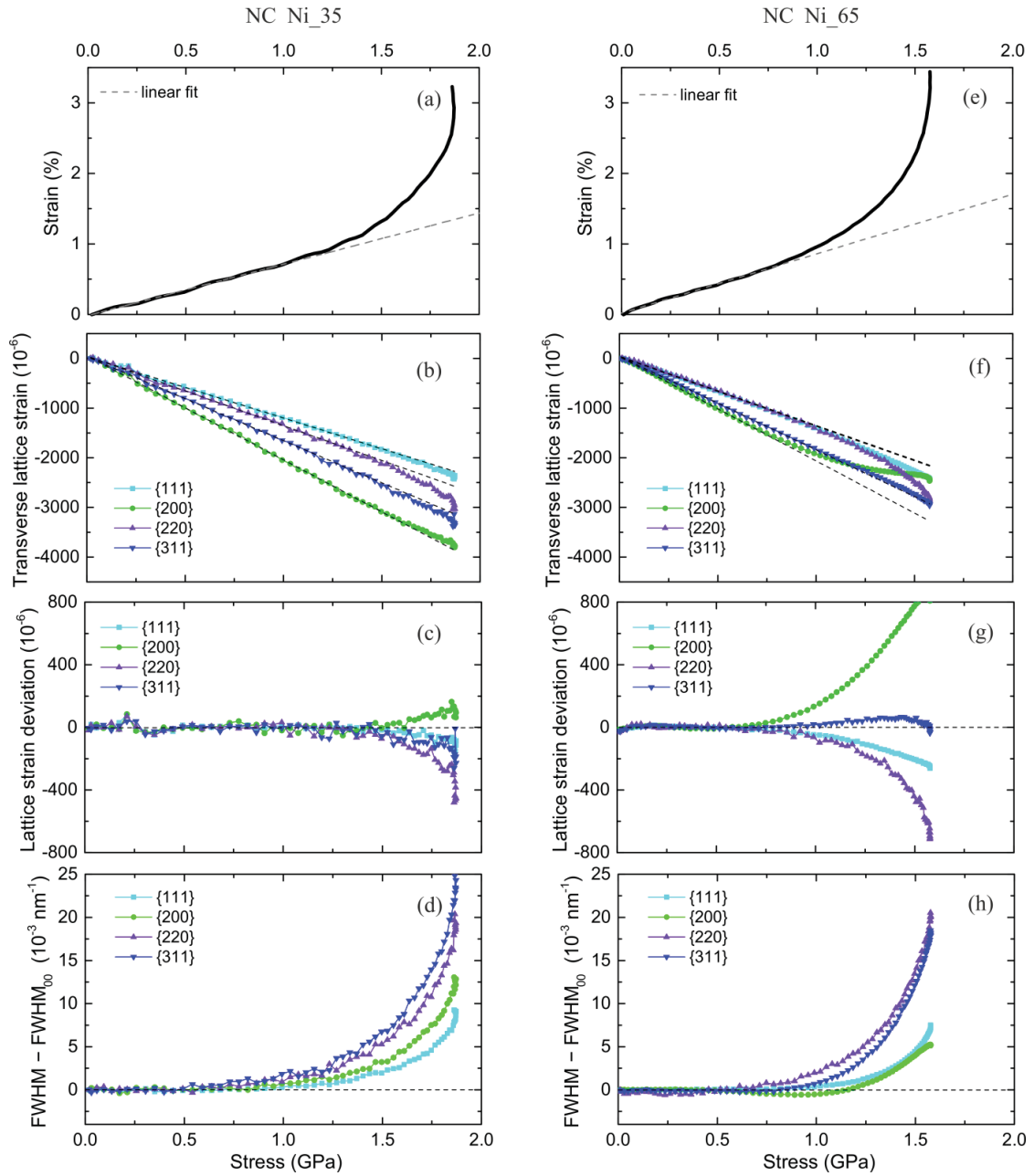


Figure 3-1 Overview of deformation behaviour during the *in situ* continuous tensile tests for Ni₃₅ (a-d) and Ni₆₅ (e-h): (a, e) the stress-strain curves; (b, f) corresponding evolution of the transverse lattice strain for {111}, {200}, {220}, and {311} grain families; (c, g) deviation of lattice strain from the linear fit (dashed line); (d, h) corresponding evolution of FWHM for all grain families.

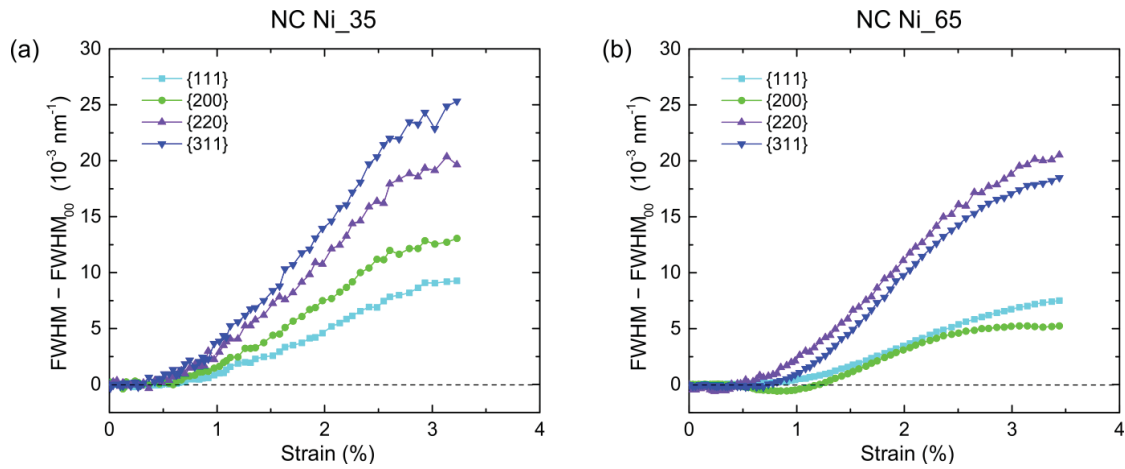


Figure 3-2 The evolution of the FWHM for {111}, {200}, {220}, and {311} grain families as a function of total strain: (a) NC Ni₃₅ and (b) NC Ni₆₅

Compression tests

Continuous compression testing during X-ray diffraction was performed at a constant total strain rate $\dot{\epsilon}_{tot}$ of 10⁻⁴ /s. Figure 3-3a shows the stress-strain curve for NC Ni₃₅. Due to the differences in machine compliance between MTM and K&W and their respective length calibration systems, here the slope in the elastic regime is lower. Nevertheless, a plateau regime is observed. The most interesting result of *in situ* data analysis is the evolution of the FWHM as a function of total strain shown in Figure 3-3b. After the flow stress becomes essentially constant, the peak width of all grain families gets saturated. This result confirms the previous observation from tensile test. Afterwards, some reflections exhibit subsequent reductions in FWHM, which may be associated with grain growth. The *in situ* data recorded for NC Ni₆₅ is unfortunately not valid due to severe distortion on specimen surface.

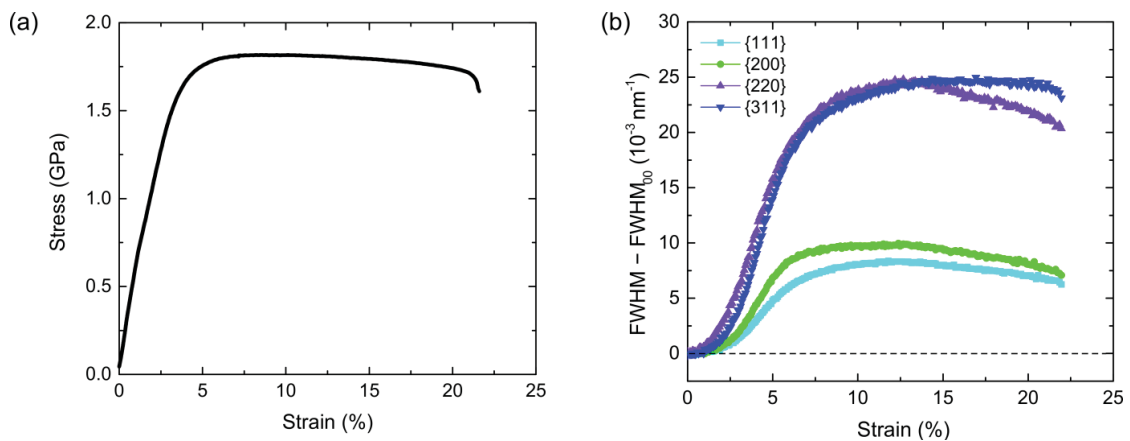


Figure 3-3 NC Ni₃₅: (a) the stress-strain curve of a compression test; (b) the evolution of the FWHM for {111}, {200}, {220}, and {311} grain families as a function of total strain.

3.1.2 Continuous deformation at different strain rates

A series of *ex situ* continuous tensile tests with constant strain rates $\dot{\epsilon}_{tot}$ ranging from 10^{-6} /s to 10^{-3} /s were conducted on both NC Ni batches. The characteristic of the stress-strain curve of NC Ni have been shown in Figure 3-1 (tension) and Figure 3-3 (compression). The constant flow stress can be considered as a quasi-stationary state where there is a balance between different deformation mechanisms. Figure 3-4 presents these quasi-stationary stress values for NC Ni₃₅ (solid) and compares them with the values obtained for NC Ni₆₅ (open). For all strain rates, the material with larger average grain size has lower values for the flow stress, suggesting a Hall-Petch strengthening. For both NC Ni batches the quasi-stationary stress values increase with increasing strain rate. However, this is not the case for NC Ni₅₀Fe₅₀: the maximum flow stress is hardly dependent on the strain rate within the range 6×10^{-7} /s to 3×10^{-2} /s, as reported in Ref. [113]. In this section, deformation in tension was selected because MTM machine with small step size is capable of a wider range of test speeds.

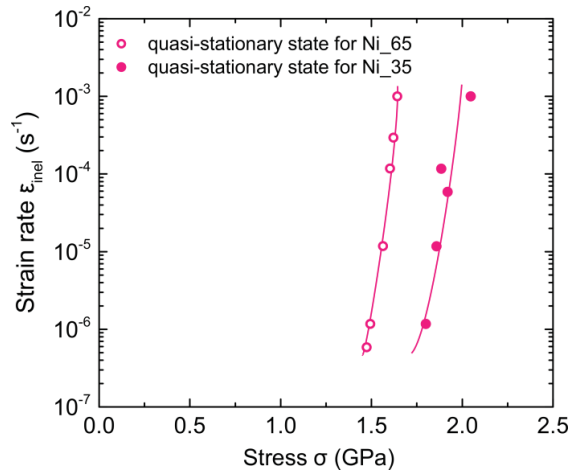


Figure 3-4 The quasi-stationary stress values for NC Ni₃₅ (solid) and NC Ni₆₅ (open) obtained in continuous tensile tests at constant strain rates.

3.1.3 *In situ* load-unload deformation

Tensile tests

A series of load-unload cycles during X-ray diffraction was performed, which allows investigating the evolution of residual lattice strain as well as peak broadening. Figure 3-5a and b display the corresponding stress-strain curves for NC Ni₃₅ and Ni₆₅. In both tests, the first load-unload cycle starts in the elastic regime (< 0.5 GPa) whereas the last load-unload cycle ends near the maximum flow stresses. For each cycle, the specimen after unloading was kept at a macrostress-free state for 20 min.

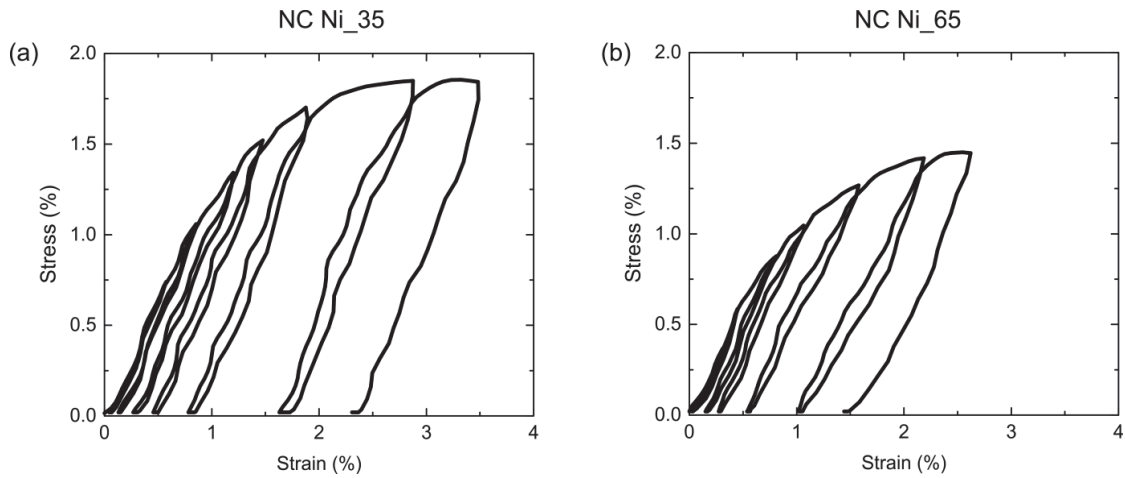


Figure 3-5 The corresponding stress-strain curves of a series of load-unload cycles for (a) NC Ni₃₅ and (b) Ni₆₅.

For NC Ni₃₅, given the stress-time relation in Figure 3-6a, the corresponding evolution of the lattice strain, and the FWHM of {111}, {200}, {220}, {311} diffraction peaks are displayed in Figure 3-6b and c. Similar as what has been observed before [94][113], three regimes may be distinguished based on the evolution of the lattice strain and the peak broadening: I-elastic, II-microplastic and III-macroplastic regime.

In the microplastic regime, there is hardly any change in lattice strain but clearly a decrease in peak broadening associated with structural relaxation upon loading. Once entering the macroplastic regime, both lattice strain and peak broadening are changing in the unloaded state. The observation of residual lattice strains after unloading from 1.5 GPa indicates the development of intergranular strains. In the last two cycles, the specimen was loaded to the maximum flow stress. Upon unloading the extra recovery in FWHM obtained during previous load cycles disappears to a great extent: the {200} and {220} reflections remain still a bit narrower compared to their initial values, but the {311} has returned back, even slightly increased relative to the non-deformed state.

For NC Ni₆₅, the corresponding mechanical and *in situ* data sets are shown in Figure 3-6d-f. Here, the development of the residual lattice strain starts already at low stresses, suggesting an early onset of plastic deformation. Compared to Ni₃₅, Ni₆₅ generates remarkably higher amounts of residual stress (internal strain) after unloading from the macroplastic regime. The difference has to be attributed to a larger average grain size, but the strong {100} texture along the transverse direction might also play an important role.

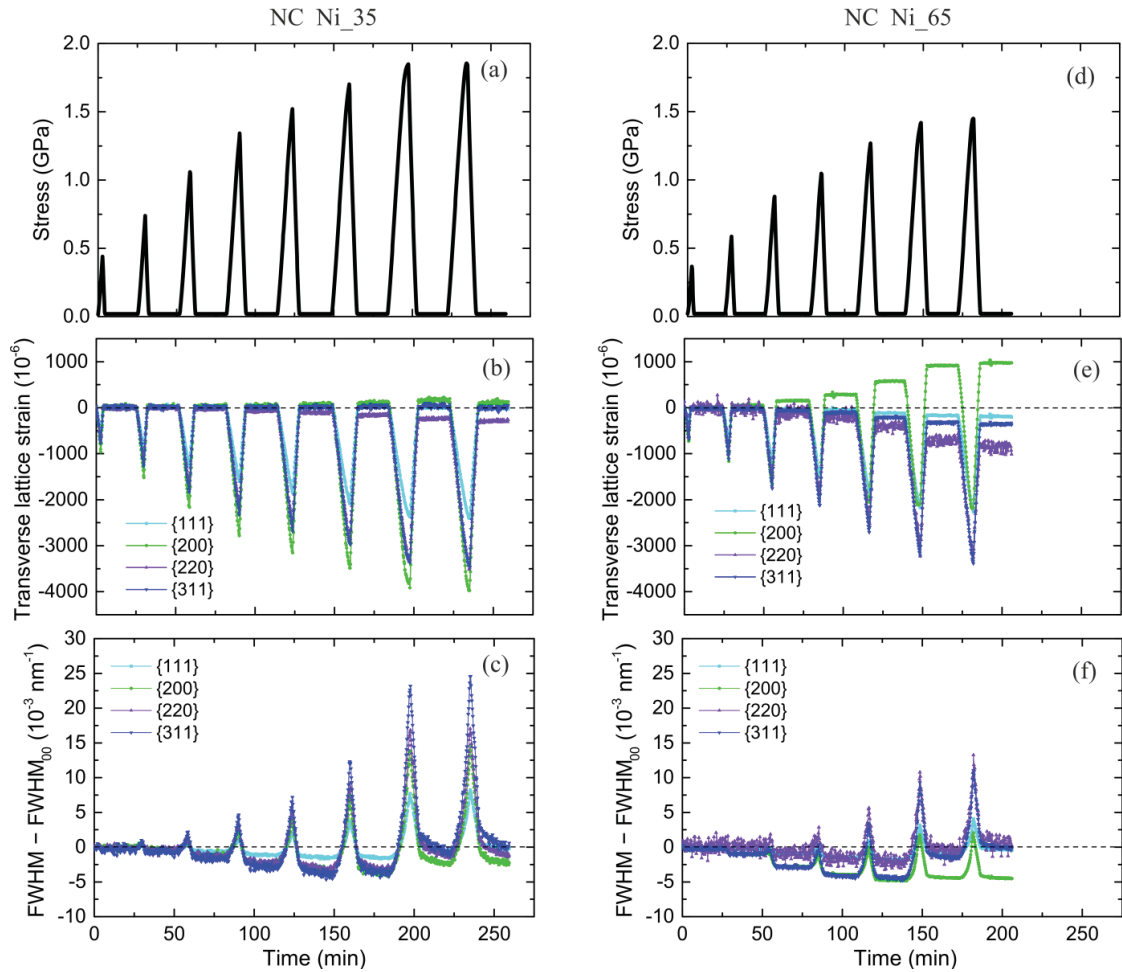


Figure 3-6 Overview of deformation behaviour during *in situ* load-unload tensile tests for Ni₃₅ (a-c) and Ni₆₅ (d-f): (a, d) the stress-time relation; (b, e) corresponding evolution of the lattice strain for {111}, {200}, {220}, and {311} grain families; (c, f) corresponding evolution of the FWHM for all grain families.

Compression tests

Further investigation of peak broadening in the plateau regime (constant deformation resistance) is feasible under the condition of compression. Figure 3-7a displays the corresponding stress-strain curve for the NC Ni₃₅, where the first load-unload cycle starts at 1.5 GPa whereas the remaining cycles are in the plateau regime. Figure 3-7b shows the evolution of the FWHM as a function of time. There is an extra recovery of FWHM for all grain families upon first unloading. Then upon unloading from the next cycles, the recovery observed for {111} and {311} grain families vanishes and the FWHM of {220} grain family increases well above its original value before deformation.

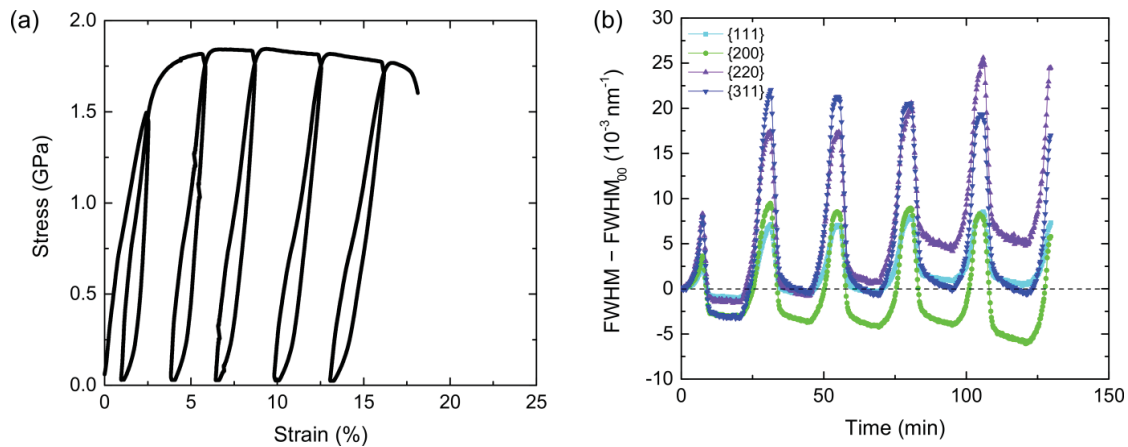


Figure 3-7 NC Ni₃₅: (a) the stress-strain curve of a series of load-unload cycles in compression; (b) the evolution of the FWHM for {111}, {200}, {220}, and {311} grain families as a function of time.

3.1.4 Summary

The measurements of *in situ* continuous and load-unload deformation on NC Ni batches confirm the early findings performed on NC material from Goodfellow [15][18][94], demonstrating that it is a characteristic behaviour for NC Ni. In addition, the following results have been obtained

- *In situ* continuous deformation in tension and compression confirm that the peak widths for all grain families get saturated after the flow stress becomes essentially constant.
- For NC Ni, the quasi-stationary flow stress, i.e. the constant flow stress reached in continuous deformation is strain rate dependent. For a given strain rate, the quasi-stationary flow stress of NC Ni₆₅ is always lower than that of NC Ni₃₅, suggesting a Hall-Petch strengthening.
- NC Ni₆₅ exhibits an earlier onset of plastic deformation and generates remarkably higher amounts of residual stress (internal strain) upon unloading from the macroplastic regime. This has to be attributed to two microstructural differences: a larger average grain size and a stronger {100} texture.

3.2 Stress reduction tests on nanocrystalline Nickel

To explore the interplay between the deformation mechanisms responsible for the development of a constant deformation resistance in NC metals, stress reduction tests were performed. This technique was combined with *in situ* X-ray diffraction, allowing following the structure evolution and capturing the underlying deformation mechanisms that control the strength. Stress reductions tests were carried out in the conventional way (Section 3.2.1) and subsequently in the modified ways (Section 3.2.2 and Section 3.2.3).

3.2.1 Conventional stress reduction tests

Figure 3-8 provides a schematic of the principle of conventional stress reduction tests. Each specimen was first strained to a pre-defined stress σ_0 at a constant loading rate 10^{-3} /s except mentioned otherwise. Then

3.2 Stress reduction tests on nanocrystalline Nickel

upon reaching σ_0 the specimen was fast unloaded by a certain amount of stress $\Delta\sigma$, and allowed to creep at the reduced stress σ_r , for a certain period of time. The ratio between these two stress levels is denoted by the relative reduced stress $R = \sigma_r / \sigma_0$, which is used to compare the transient behaviour of materials with different microstructures. In the case of a tensile test, it was chosen to perform the stress reduction tests at a stress level prior to reaching the quasi-stationary regime. This was done to avoid the influence of necking. In the case of a compression test, larger strain can be achieved so that stress reduction could be carried out at a strain well within the quasi-stationary state. At the end of the creep period the specimen was reloaded with the same initial loading rate of 10^{-3} /s until fracture.

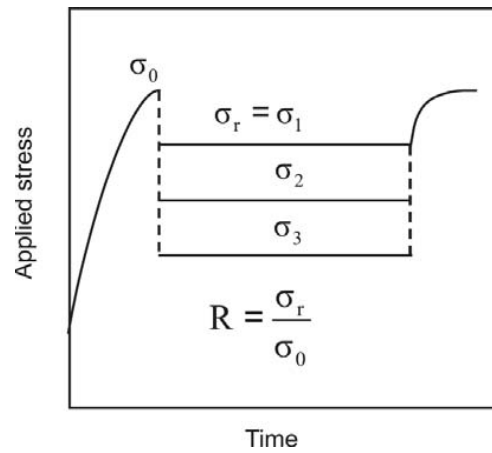


Figure 3-8 Schematic representation of a series of conventional stress reduction tests: the specimen is first strained to a pre-defined stress σ_0 reached with a constant loading rate, followed by a fast stress reduction and creep at a reduced stress σ_r . Finally, at the end of creep the specimen is reloaded until fracture.

Tensile tests

Table 3-1 provides an overview of the conventional stress reduction experiments that have been done on NC Ni batches. Note that all tests were performed in the macroplastic regime, the onset of which can be either determined from *in situ* load-unload testing (Section 3.1.3) or the yield criterion defined by L. Thilly *et al.* [149]. Using Thilly's criterion, a relative high value 1.6 GPa for NC Ni_35 and 1.2 GPa for NC Ni_65 was obtained.

Table 3-1 Overview of all conventional stress reduction tests done on NC Ni batches.

Batch	Number of specimens	σ_0 (GPa)	R	Creep time	Instrument
NC Ni_35	12	1.75	0.1 ~ 1	30 min	<i>in situ</i>
	1	1.75	0.67	60 min	<i>in situ</i>
	1	2	0.82	60 min	<i>in situ</i>
	1	2	0.70	165 h	<i>ex situ</i>
NC Ni_65	11	1.5	0.18 ~ 1	30 min	<i>in situ</i>

Creep after stress reduction

For NC Ni₃₅, 12 specimens were employed in the standard *in situ* stress reduction tests series (see 1st row in Table 3-1). Stress reductions with different magnitudes were carried out at $\sigma_0 = 1.75$ GPa; at each reduced stress level the specimen was allowed to creep 30 min during *in situ* X-ray diffraction. Figure 3-9a and b summarizes the stress-dependent transient behaviour for R ranging from 1 to 0.1. Note that the specimens of the tests with $R = 1$ and $R = 0.96$ were pre-deformed under the constant loading strain rate $\dot{\epsilon}_{tot}$ of 10^{-4} /s whereas the others were deformed at 10^{-3} /s.

Figure 3-9a and Figure 3-9b describe the evolution of the inelastic strain and the FWHM of the {311} diffraction peak as a function of time, respectively. The {311} peak was chosen because both simulations and *in situ* experiments show that the {311} peak exhibits the greatest increase in peak width when the microstructure of the sample is dominated by dislocations [18][150]. Two distinguished behaviours of the initial inelastic strain rate $\dot{\epsilon}_{r,i}$ can be recognized immediately after the stress drop. When the stress drop is mild the specimen continues to deform plastically in a forward direction, i.e. $\dot{\epsilon}_{r,i} > 0$, however, with decreasing inelastic strain rate $\dot{\epsilon}_{inel}$. At larger stress drops the immediately measured strain rate is negative, i.e. $\dot{\epsilon}_{r,i} < 0$, evidencing the dominance of anelastic back flow. After sufficient relaxation of the internal back stresses driving the back flow, forward straining is observed again, at least when the stress drop is not too large. This positive strain rate $\dot{\epsilon}_{inel}$ reaches a relative maximum $\dot{\epsilon}_{r,max}$ after which $\dot{\epsilon}_{inel}$ decreases further with increasing creep time. Figure 3-10 schematically illustrates different definitions of strain rate as mentioned above. For the lowest R (largest stress drop) no forward straining is observed, but this might be due to a too short measuring time.

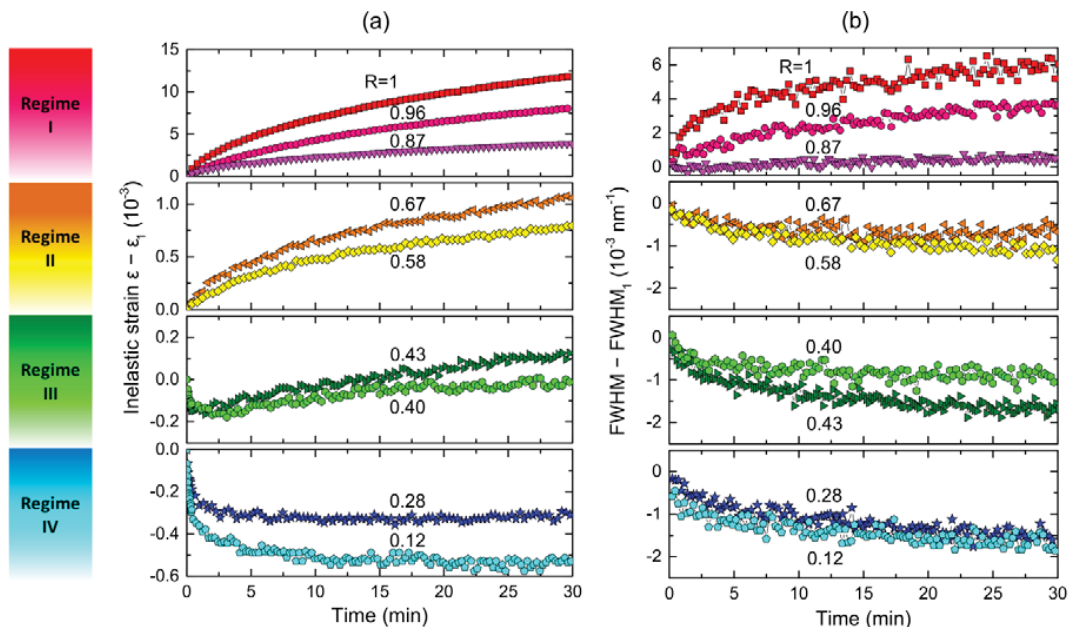


Figure 3-9 Results of the standard *in situ* stress reduction tests series on NC Ni₃₅. Transient responses in dependence of R for $\sigma_0 = 1.75$ GPa: (a) the inelastic strain, and (b) the FWHM of the {311} diffraction peak as a function of creep time. ϵ_1 and FWHM₁ refer to the values at the beginning of creep.

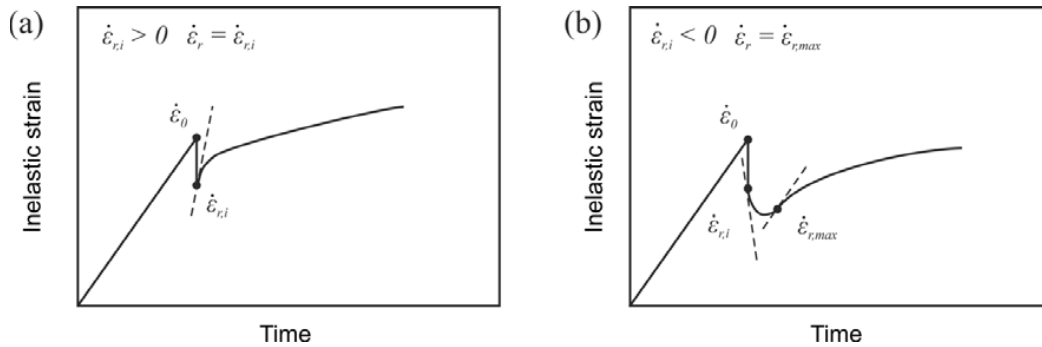


Figure 3-10 Schematic illustration of different definitions of strain rate during transient creep: (a) $\dot{\epsilon}_{r,i} > 0$ and (b) $\dot{\epsilon}_{r,i} < 0$

Combining the aforementioned inelastic strain behaviours with the signatures for the FWHM, four regimes can be recognized. In Regime I, corresponding with the smallest stress drops, positive inelastic strain is measured together with an increase in FWHM. In Regime II, corresponding with slightly larger stress drops, still positive inelastic strain is produced, but the FWHM decreases. At larger stress drops, Regime III, a transient behaviour is observed where first negative and then positive inelastic strain is produced both accompanied by a reduction in FWHM. At the largest stress drops, Regime IV, the inelastic strain seems to be always negative during the time of observation and is combined with a reduction in FWHM.

Inspection of the behaviour of the FWHM in Regime II hints to an increasing FWHM at the end of the 30 min creep regime. Therefore, two additional *in situ* stress reduction experiments were carried out in Regime II with different values of reduced stress and different values of initial plastic strain, both followed by a creep period of 60 min (see 2nd and 3rd row in Table 3-1). This is schematically sketched in Figure 3-11a.

Figure 3-11b shows the corresponding results of the first *in situ* test with $R = 0.67$, whereby the evolution of the strain rate $\dot{\epsilon}_{inel}$ (black curve) and the FWHM (blue curve) are plotted as a function of inelastic strain. Here, using strain as abscissa instead of time has the advantage of evidencing the structural development, in particular during transient creep with long periods of time. It can be seen that while the strain rate (black curve) decreases continuously, the FWHM of the {311} diffraction peak starts to increase again after a plastic strain of approximately 1×10^{-3} was produced. This cross-over in the peak broadening could not be observed for the other diffraction peaks which remain decreasing.

The second *in situ* test with $R = 0.82$ was carried out after reaching a flow stress of 2 GPa, corresponding to a larger plastic strain at the moment of the stress drop. Figure 3-11c shows the corresponding behaviour of the strain rate (black curve) and the FWHM of the {311} diffraction peak (blue curve). Also here the strain rate remains decreasing, while the FWHM first decreases and then increases. For this specimen such behaviour is observed for all diffraction peaks. The strain at which the FWHM starts increasing again is larger in this specimen, suggesting that the strain produced by mechanisms that reduce the FWHM depends not only on the reduced stress, but probably also on the amount of plastic strain obtained prior to the stress drop.

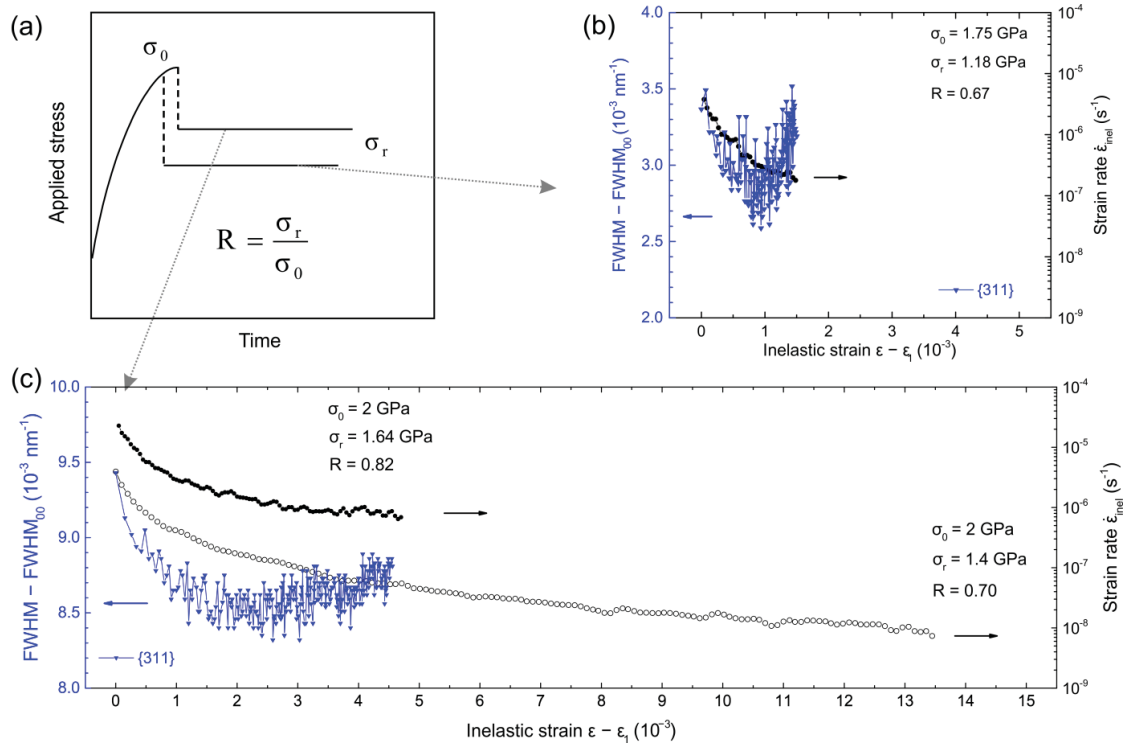


Figure 3-11 Results of *in situ*/*ex situ* stress reduction experiments with long creep times on NC Ni₃₅: (a) the schematic representation of the *in situ* experiments; (b) and (c) the evolution of the strain rate (black curve) and the peak broadening (blue curve) for the 60 min stress reduction tests performed at $\sigma_0 = 1.75 \text{ GPa}$ and $\sigma_0 = 2 \text{ GPa}$ with R values of 0.67 and 0.82, respectively. Also shown in (c) is the evolution of the strain rate (black open symbols) for a 165 hours creep period test with R value of 0.70. FWHM₀₀ refers to the value at non-deformed state.

It is important to note that in all the tests carried out in Regime I and II where immediate positive strains are measured, the strain rate $\dot{\epsilon}_{inel}$ always decreases and no increase in strain rate after a certain amount of creep time is observed. Such an increase was typically observed in CG materials [115][117][120]. To be sure that this is not related to the restriction of creep time during an *in situ* experiment, an *ex situ* creep test was carried out during 165 hours (4th row in Table 3-1). A specimen was deformed up to 2 GPa followed by a stress drop to 1.4 GPa ($R = 0.7$). The initial transient strain rate is $\dot{\epsilon}_{r,i} = 4 \times 10^{-6} / \text{s}$. The evolution of the strain rate as a function of inelastic strain is added in Figure 3-11c (black open symbols). At the end of the creep experiment the inelastic strain reached 1.4 % with a continuously decreasing strain rate that finally dropped to $\sim 10^{-8} / \text{s}$. Interestingly, the strain rate seems not to reach a quasi-stationary value after 165 hours of creep time. To observe the quasi-stationary rate larger strains need to be produced.

For NC Ni₆₅, the standard *in situ* stress reduction tests series were carried out at $\sigma_0 = 1.5 \text{ GPa}$, which is slightly below the UTS of 1.6 GPa attained at $\dot{\epsilon}_{tot}$ of $10^{-3} / \text{s}$. Figure 3-12 summarizes the stress-dependent transient behaviours for R ranging between 1 to 0.1: four regimes can be categorized based on the evolution of the inelastic strain (Figure 3-12a) and the change of the FWHM of {311} diffraction peak (Figure 3-12b) during creep periods of 30 min. They exhibit similar characteristics to those of NC Ni₃₅. The non-monotonic change of FWHM is observed for the specimen with $R = 0.91$ after it has been crept for 10 min only.

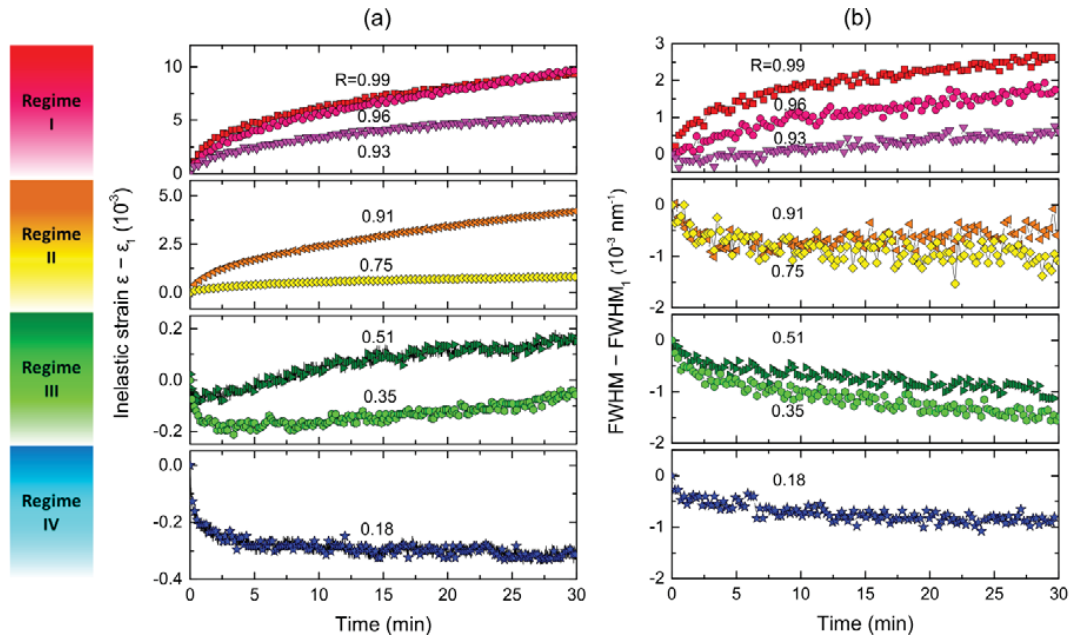


Figure 3-12 Results of the standard *in situ* stress reduction tests series on NC Ni₆₅. Transient responses in dependence of R for $\sigma_0 = 1.5$ GPa: (a) the inelastic strain, and (b) the FWHM of $\{311\}$ diffraction peak as a function of creep time. ε_1 and FWHM_1 refer to the values at the beginning of creep.

Stress dependence of creep rate

Assuming that the microstructure does not change during the sudden stress drop, it is possible to derive the stress dependence of the initial creep rate at constant microstructure. In Figure 3-13, the normalized forward creep rate $\dot{\varepsilon}_r/\dot{\varepsilon}_0$ as a function of normalized stress σ/σ_0 is plotted on a semi-logarithmic scale. The data points in NC Ni₃₅ (only tests with $\sigma_0 = 1.75$ GPa are considered) and Ni₆₅ are respectively represented by solid and open symbols; the colours refer to three different regimes observed in Figure 3-9 (for NC Ni₃₅) and Figure 3-12 (for NC Ni₆₅). According to different definitions of strain rate illustrated in Figure 3-10, $\dot{\varepsilon}_r$ equals $\dot{\varepsilon}_{r,i}$ in Regimes I and II, while in Regime III $\dot{\varepsilon}_r$ is the maximal forward strain rate $\dot{\varepsilon}_{r,max}$ after stress reduction and anelastic back flow; σ_0 , $\dot{\varepsilon}_0$ refer to the values just prior to the stress reduction. Since positive strain rate $\dot{\varepsilon}_{r,max}$ in Regime III (green) was measured only after a time interval of a few minutes where anelastic back flow and recovery have modified the microstructure, the term “constant structure” is not exact with regard to fast changing parameters like dislocation density and internal stress distribution. Still, it is an acceptable presumption, which allows investigating the individual contribution from multiple deformation mechanisms.

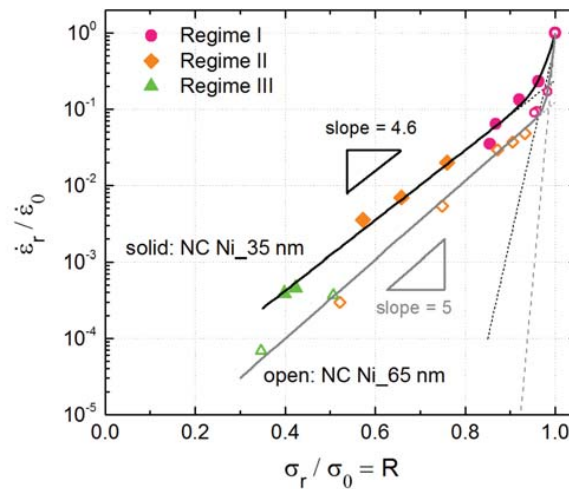


Figure 3-13 For NC Ni₃₅ (solid symbols) and NC Ni₆₅ (open symbols), the normalized forward creep rate $\dot{\epsilon}_r / \dot{\epsilon}_0$ as a function of normalized stress σ_r / σ_0 is plotted on a semi-logarithmic scale. Each group of data is fitted by a sum of two exponential functions (dashed lines). The solid line represents the resulting fit.

Inspection of the plots for both materials show that for moderate and large stress drops (Regimes II-III), for which the FWHM always decreases immediately after the stress drop, the logarithm of the creep rate $\dot{\epsilon}_r$ is linearly proportional to the stress (slope 4.6 for NC Ni₃₅ and slope 5 for NC Ni₆₅), independent of whether the drop is done in a regime where there is a continuation of forward flow (Regime II) or in a regime where first anelastic back flow is observed (Regimes III). However, in Regime I where the stress drops are small and the diffraction peak broadens continuously, the fit to the data points (solid line) deviates from linearity and the stress dependence increases. In fact, the $\dot{\epsilon}_r$ data can be described as a sum of two $\dot{\epsilon}_r$ -contributions with different exponential stress dependence as shown by the straight dashed lines in Figure 3-13.

Reloading after stress reduction

After the transient creep period the specimens were reloaded until failure with a loading rate of 10^{-3} /s. Figure 3-14a and b display the corresponding stress-strain curves (black curve) for NC Ni₃₅ and Ni₆₅, both with relative reduced stress $R = 0.87$, evidencing a smooth extrapolation over the stress drop point. Additionally, for both NC Ni batches such a curve is found to coincide approximately with the stress-strain curve obtained from a continuous tensile test at the same loading rate, as indicated by the red dashed curve.

To further explore the influence of stress drops with different magnitudes on the deformation behaviour, the shape of stress-strain curves in particular reloading parts were examined. It is found that most tests obtain a similar stress value at the quasi-stationary state; some scattering may associate with the diversity of specimen and the resolution of measurements. The interpretation of this observation may refer to a strain-path independent quasi-stationary flow stress solely dependent on the strain rate. Also, it indicates that there is no significant grain coarsening after transient creep, otherwise the maximum flow stress would have been reduced according to Hall-Petch law.

3.2 Stress reduction tests on nanocrystalline Nickel

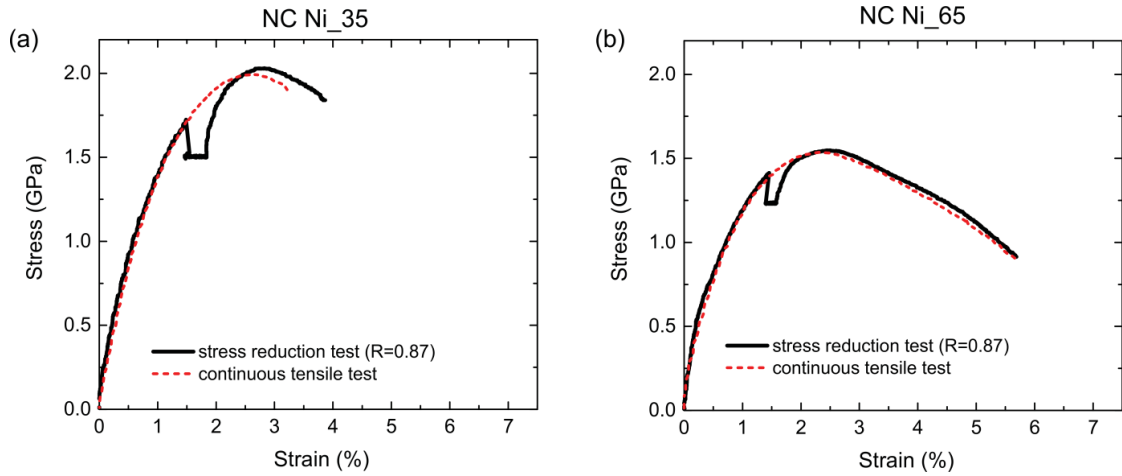


Figure 3-14 stress-strain curves of a conventional stress reduction test (black curve) and a continuous tensile test (red dashed curve) at the same loading rate: (a) NC Ni₃₅ and (b) NC Ni₆₅, both with $R = 0.87$

Compression tests

For NC Ni₃₅, the *in situ* stress reduction experiments in compression were performed at a well-defined quasi-stationary state (a regime without work-hardening). Figure 3-15a shows the stress-strain curve for a compression experiment, in which a small stress drop of $R = 0.93$ was done at a true strain of $> 10\%$, followed by a 30 min creep and reloading until failure. Figure 3-15b shows the corresponding behaviour of FWHM for {111}, {200}, {220}, and {311} diffraction peaks. It is observed that during the creep period the FWHM continuously decreases independent of the magnitude of the stress drop. This is in contrast to the results for tensile experiments, in which the FWHM increases with time after a similar stress drop.

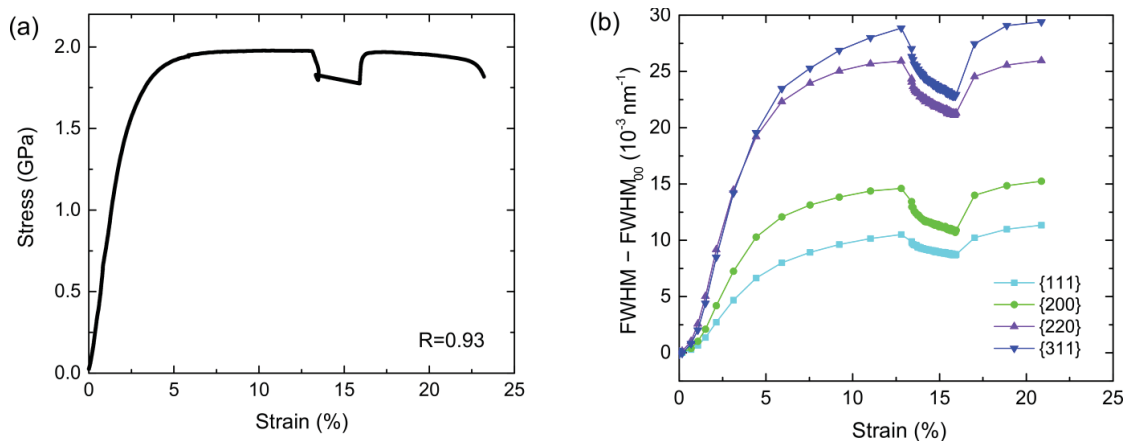


Figure 3-15 Results from an *in situ* stress reduction experiment during compression on NC Ni₃₅: (a) the stress-strain curve and (b) the change of the FWHM with total strain. FWHM_{00} refers to the value at non-deformed state.

Figure 3-16a and b inspect the evolution of the strain rate (black curve) and the FWHM of {311} diffraction peak as a function of inelastic strain. It can be seen that both strain rates and the FWHM monotonically decrease although a larger strain of 2.5 % has been reached

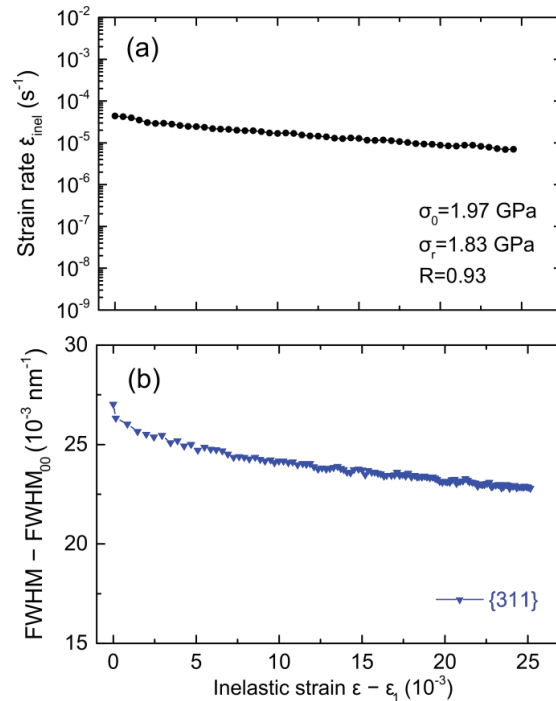


Figure 3-16 The evolution of (a) the strain rate (black curve) and (b) the FWHM of {311} diffraction peak (blue curve) as a function of inelastic strain during transient creep. FWHM_{00} refers to the value at non-deformed state.}

3.2.2 Inserting creep before stress reduction

All conventional stress reduction tests in tension (Section 3.2.1) were carried out prior to the quasi-stationary flow stress, see Figure 3-14. This may lead to a continuation of work-hardening by a net increase of defects even after a limited stress reduction. Inserting a short creep period at σ_0 before stress reduction helps further approach the quasi-stationary state, whereby the results may be comparable to those of stress reduction experiments in compression.

Figure 3-17a shows the stress-time relation of such an experiment performed on NC Ni₃₅: after the specimen was loaded to $\sigma_0 = 1.8 \text{ GPa}$ at $\dot{\epsilon}_{\text{tot}} = 10^{-3} / \text{s}$, the transient periods were composed of four stress-controlled stages that are specified in Table 2-1. Figure 3-17b is the corresponding stress-strain curve. It can be seen that after inserting 1st stage the stress reduction with $R = 0.89$ was performed at an extended strain, 1 % more than that in a conventional stress reduction test as shown in Figure 3-14a.

3.2 Stress reduction tests on nanocrystalline Nickel

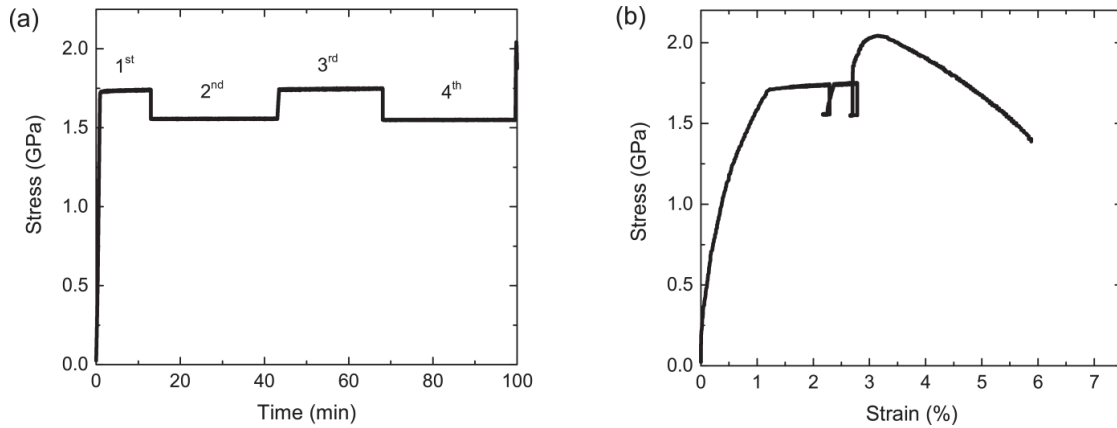


Figure 3-17 A modified stress reduction experiment performed on NC Ni₃₅, in which a short creep period was inserted before the stress reduction so that the quasi-stationary state can be further approached: (a) the stress-time relation and (b) the stress-strain curve.

Table 3-2 A modified stress reduction test in which the transient periods are composed of four different stress-controlled stages.

Transient stages	σ_0 (GPa)	σ (GPa)	R	Creep (min)
1 st	1.8	1.8	1	10
2 nd	1.8	1.6	0.89	30
3 rd	1.6	1.8	1.13	25
4 th	1.8	1.6	0.89	30

Figure 3-18a and b show the corresponding evolution of the strain rate and the FWHM of {311} diffraction peak as a function of inelastic strain. In the 1st and 3rd stage the specimen was crept at 1.8 GPa. The strain rate and the FWHM in the 3rd stage show a continuation of the existing trend in the 1st stage: they respectively decrease and increase with the increasing strain, approaching the quasi-stationary values. Such continuation of the trends would be expected as well for the 2nd and 4th stage where the specimen was crept at 1.6 GPa. However, very limited inelastic strain was produced. Moreover, at this stress level one observes a continuous reduction in FWHM after a small stress drop with $R = 0.89$, which is in agreement with the results obtained from *in situ* stress reduction tests in compression.

3.2.3 Multistep test

In the case of conventional stress reduction tests (Section 3.2.1), a major issue often encountered is that at a low reduced stress where dislocation glide is suppressed enough, the strain rate becomes so low that the full transient response is not accessible during an *in situ* measurement. This is visualized in Figure 3-19: after a large stress reduction the maximum forward strain rate $\dot{\epsilon}_{r,max}$ (black dot) continuously decreases under the constant applied stress during the creep period, as indicated by the blue dashed line. As the specimen is crept further, the strain rate drops out of the timescale of observation so that it can hardly approach the new quasi-stationary line as indicated by the pink solid line.

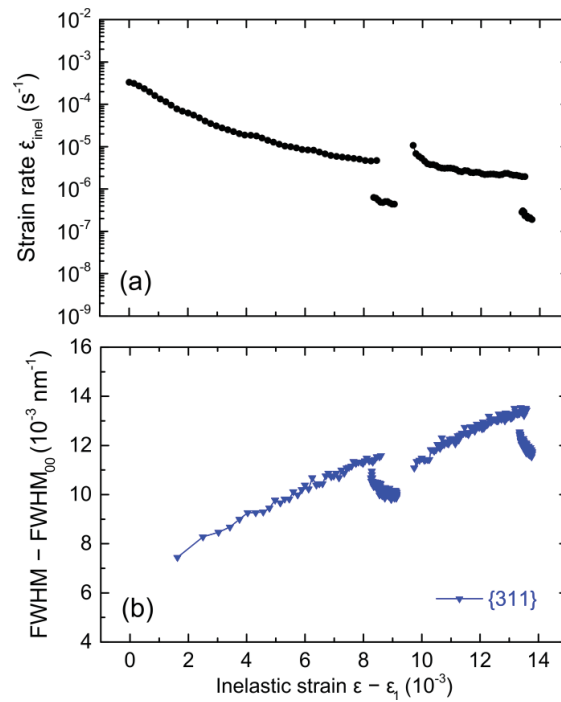


Figure 3-18 The evolution of (a) strain rate and (b) the FWHM of {311} diffraction peak as a function of inelastic strain during transient periods. FWHM₀₀ refers to the value at non-deformed state.

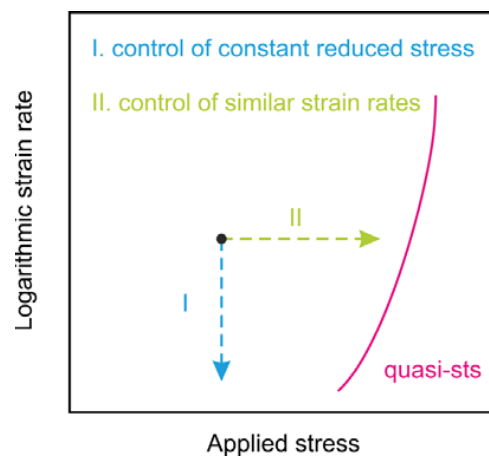


Figure 3-19 Schematic representation of the evolution of strain rates during I. single transient creep in a conventional stress reduction test (blue dashed line) and II. repeated transient creep in a multistep test with each step ending near the creep rate given by the green dashed line. Black dot is the maximum forward strain rate after a large stress reduction. The pink curve is quasi-stationary line.

In order to overcome this issue a new methodology has been introduced. Figure 3-20 is a schematic representation of this so-called multistep test. The operation of deformation during transient is similar to the repeated creep in the paper of J.L. Martin *et al.* [151][152]. After a large stress reduction at σ_0 , the

3.2 Stress reduction tests on nanocrystalline Nickel

applied stress was raised slightly in a series of steps (increased by ~ 35 MPa per step) and held for 20 min to creep at each stress level. The objective is to set a lower bound to the decline of creep rate in each step so that the rate stays within a certain interval. As indicated by the green dashed line in Figure 3-19, the new quasi-stationary state can be approached within measurable time by increasing stress at similar strain rates.

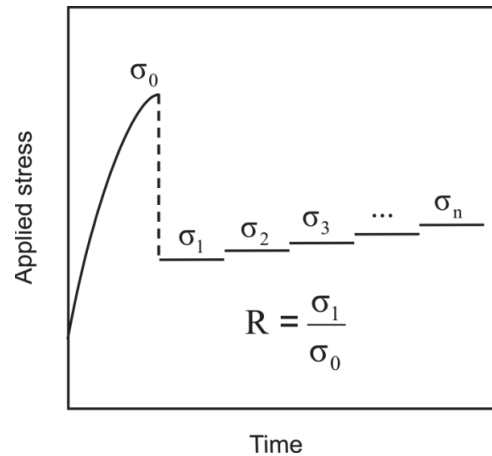


Figure 3-20 Schematic representation of a multistep test: after a large stress reduction, the applied stress is stepwise increased. In the present work, each stress level is held constant for 20 min followed by an increment of ~ 35 MPa per step.

An *in situ* multistep test on NC Ni₃₅ was performed when the specimen was first strained to $\sigma_0 = 2$ GPa with a constant strain rate $\dot{\epsilon}_{tot}$ of 10^{-3} /s. Figure 3-21a-c and Figure 3-22a-c provide an overview of the resulting transient behaviour as function of strain and stress, respectively.

Figure 3-21a shows the stress versus inelastic strain relation, and Figure 3-21b is the corresponding evolution of the strain rate. After the initial large stress reduction with $R = 0.4$ ($\sigma = 0.8$ GPa), a negative strain rate is measured, indicating anelastic back flow. After creeping for a while, the strain rate turns positive and reaches a relative maximum $\dot{\epsilon}_{r,max}$. While keeping the stress constant, the strain rate further decreases until being interrupted by a small stepwise increase in stress. Repeating this step keeps the overall rates between 10^{-7} and 10^{-6} /s; in the last step ($\sigma = 1.68$ GPa), the rate tends to be stabilized after a short decline.

Figure 3-22a represents the same strain rate data as a function of applied stress: the grey line is simply taken from the $\dot{\epsilon}_r$ -curve (solid line) from Figure 3-13 assuming the same $\dot{\epsilon}_r$ - σ relationship for $\sigma_0 = 2$ GPa. It is found that $\dot{\epsilon}_{r,max}$ (red dot) after a stress drop lies on this $\dot{\epsilon}_r$ -curve. Each vertical black line represents a continuous decrease in strain rate at a certain stress level. At the highest creep stress, the strain rate ends up with a value (green dot) approaching the quasi-stationary line (flow stresses given by Figure 3-4 in Section 3.1.2). Thus, the strength evolution in the multistep test covers nearly the whole distance from the $\dot{\epsilon}_r$ -curve to the quasi-stationary strength curve.

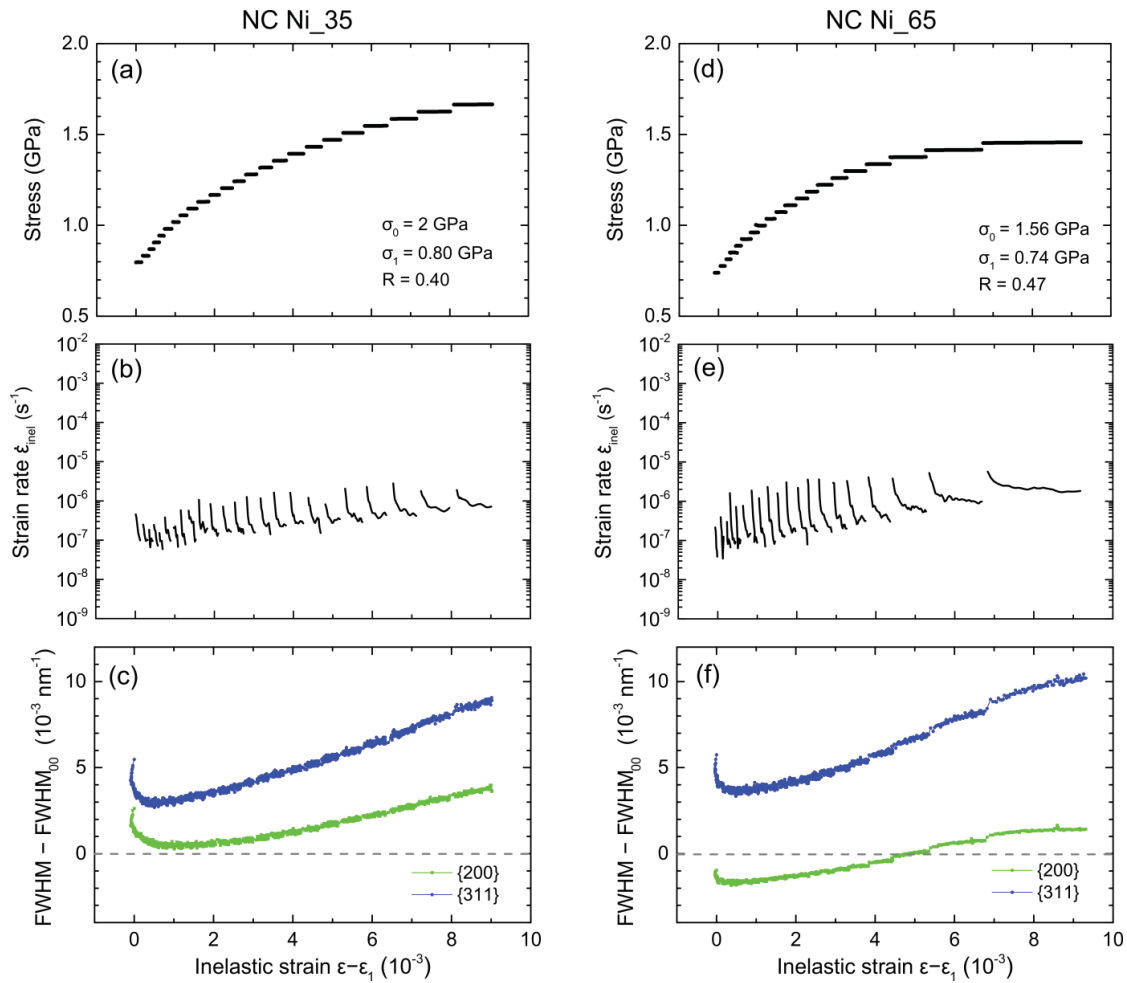


Figure 3-21 Overview of transient behaviour as a function of inelastic strain for the *in situ* multistep tests performed on Ni₃₅ (a-c) and Ni₆₅ (d-f): (a, d) the stress-inelastic strain relation, (b, e) creep rates, and (c, f) the overall change of the FWHM for {200} and {311} peaks.

The corresponding evolution of the FWHM is shown in Figure 3-21c and Figure 3-22b-c: green for the {200} diffraction peak and blue for the {311} peak. Figure 3-21c displays the overall behaviour of the FWHM as a function of the inelastic strain, evidencing a non-monotonic change. Figure 3-22b and c decouple the overall change of the FWHM for {200} and {311} peaks into two contributions: the change of the FWHM during the 20 min creep periods (square symbol) and the change upon each stress increment of ~ 35 MPa (circle symbol). Note that for the first stress increments the FWHM continuously decreases during creep periods; upon further increasing stress till ~ 1 GPa the FWHM stays constant; above 1.3 GPa the creep strain produced at each stress level grows and the change of the FWHM increases with time. In contrast, the evolution of the FWHM upon each stress increment exhibits slightly different behaviour; it is constant but non-zero.

3.2 Stress reduction tests on nanocrystalline Nickel

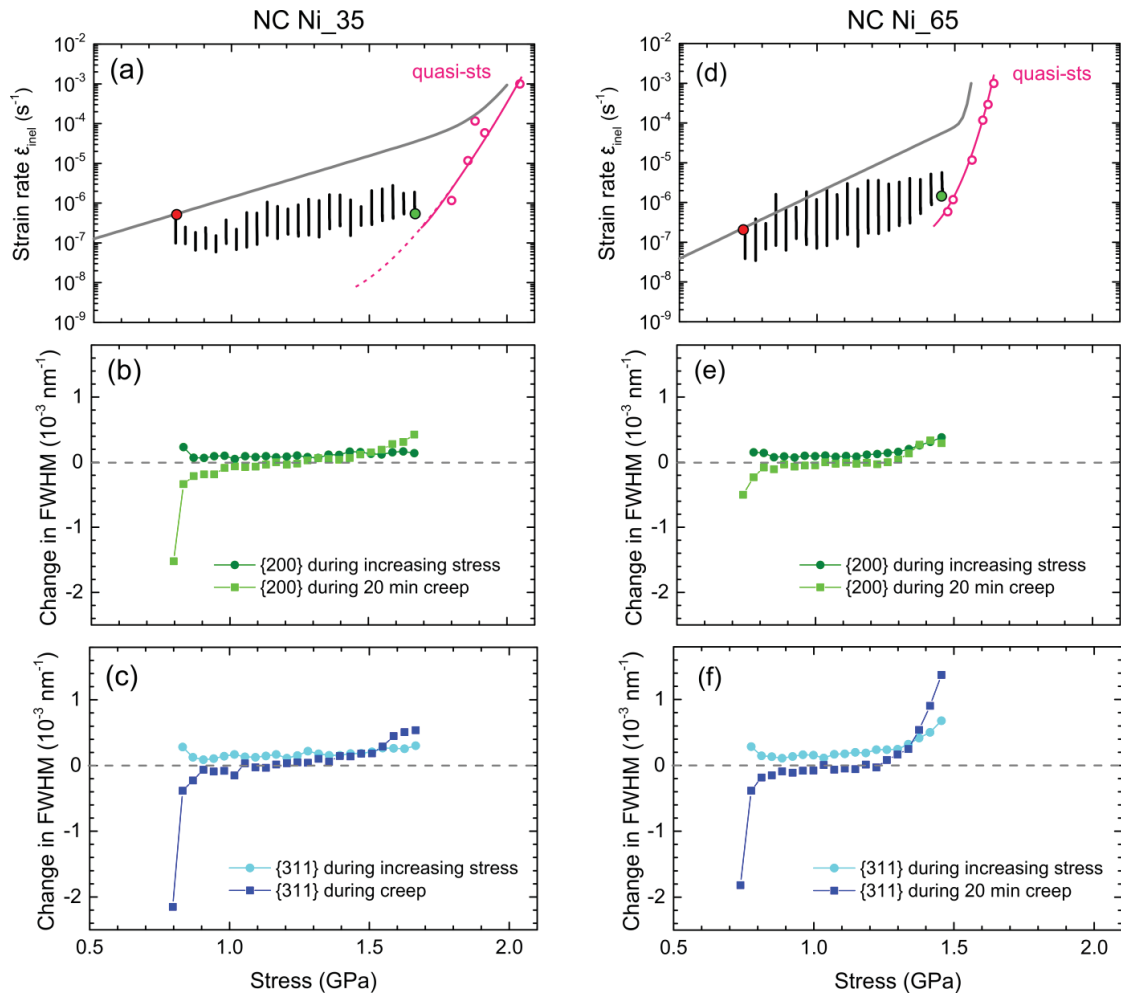


Figure 3-22 Overview of transient behaviour as a function of applied stress for the *in situ* multistep tests performed on Ni₃₅ (a-c) and Ni₆₅ (d-f): (a, d) creep rates, (b, e) and (c, f) decouple the overall change of FWHM for {200} and {311} peaks into contributions from 20 min creep periods (square symbols) and from stepwise stress increasing (circle symbols).

Figure 3-21d-f and Figure 3-22d-f provide an overview of transient responses for an *in situ* multistep test performed on NC Ni₆₅. After the specimen was strained to $\sigma_0 = 1.56$ GPa with a constant strain rate $\dot{\epsilon}_{tot}$ of 10⁻³ /s, a stress reduction with $R = 0.46$ was carried out, followed by repeated creep. The applied stress was stepwise increased from 0.74 to 1.45 GPa. It has been found that the results obtained for NC Ni₆₅ are in qualitative agreement with those for NC Ni₃₅. Quantitatively speaking, when creeping at the highest stress levels, NC Ni₆₅ exhibits a significant increase in the FWHM for the {311} peak (Figure 3-22f) as well as a larger amount of strain generated during 20 min creep (Figure 3-21e). Also for NC Ni₆₅, the evolution of the FWHM upon the stress changes is constant but non-zero up to 1.3 GPa, after which it increases in magnitude.

3.2.4 Summary

The results of stress reduction tests on NC Ni₃₅ and Ni₆₅ show qualitative agreement. The major observations can be summarized as follows:

- **Anelastic backstrain for large stress reductions:** for stress reductions with $R < 0.5$ the immediate strain rate after the stress drop is negative, which produces negative strain (Figure 3-9 and Figure 3-12). Such a sample contraction is the consequence of a negative balance between continuous forward strain and back strain created by backward motion of dislocations, which is probably related to the high internal stresses in NC samples. As a consequence, when using $\dot{\epsilon}_{r,max}$ as done in Figure 3.14, the concept of “constant structure” might be violated.
- **Softening during large/ medium stress reduction:** the forward strain rate $\dot{\epsilon}_r$ after a stress reduction is significantly larger compared to the strain rates corresponding to the quasi-stationary state (given by Figure 3-4). In multistep tests, this is evident from Figure 3-22a and d where the strain rate for each step lies on the left side of the pink curve that represents the quasi-stationary state. In conventional stress reduction tests, this is shown in Figure 3-23a for the case of two tests with $\sigma_0 = 2$ GPa.

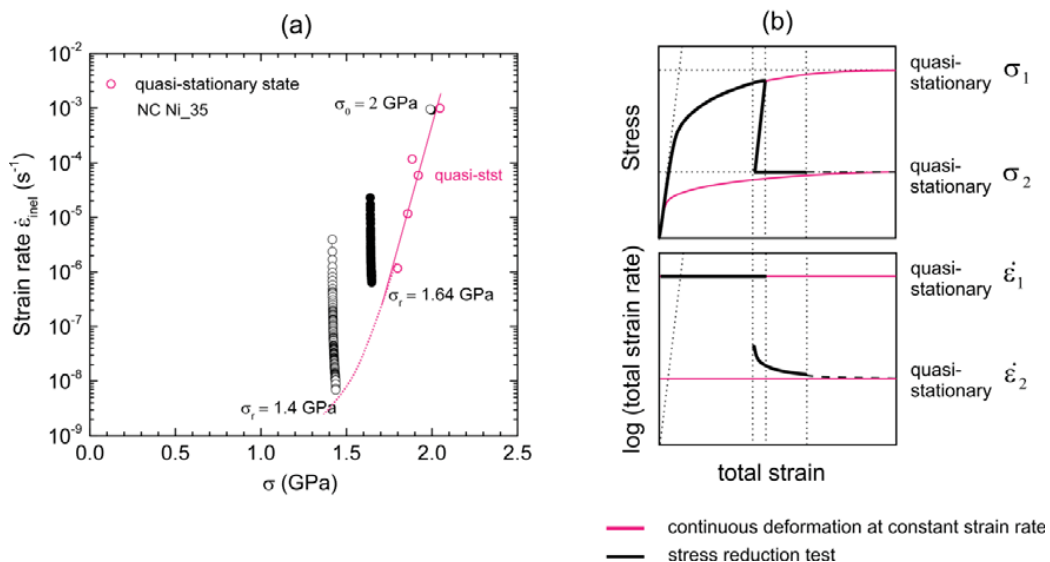


Figure 3-23 (a) The evolution of creep rates as a function of stress for stress reduction tests performed on NC Ni₃₅ with $\sigma_0 = 2$ GPa (see Figure 3-11c). Pink circles: quasi-stationary flow stresses given by Figure 3-4. (b) Schematic of the evolution of the stress (upper) and the strain rate (lower) as a function of total strain in a stress reduction test.

- **The microstructure “hardens” while approaching the quasi-stationary state:** in a multistep test, this hardening effect is evident by a stepwise increase in stress at similar low strain rates. In a conventional stress reduction test, such hardening is visible by a continuous decrease in strain rate at constant stress towards the quasi-stationary state, as shown in Figure 3-23a and b. The latter is a schematic of the evolution of stress and strain rate as a function of total strain.
- **The strain rate can be decomposed into two contributions:** this is evidenced in Figure 3-13, in which each group of data is fitted by a sum of two exponential functions (dashed lines). One of the contributions (right branch) exhibit high stress sensitivity; it is effective at high R values, for which there

is an increase of FWHM observed. The other contribution (left branch) has lower stress sensitivity (slope 4.6 for Ni_35 and slope 5 for Ni_65); it dominates at low R values, for which a reduction in FWHM is observed. At the intersection of the two dashed lines, both mechanisms of strain generation make a comparable contribution to $\dot{\epsilon}_r$.

- **There exist two classes of mechanisms that have opposite effect on the peak broadening:** from the conventional stress reduction tests (Figure 3-9 and Figure 3-12) and the multistep test (Figure 3-22) it is evident that while holding the stress constant the peak width may initially either increase or decrease, depending on the stress level after reduction. For intermediate stress drops the peak broadening exhibits a non-monotonic behaviour: after initial reduction the FWHM increases again.
- **Stress reductions at larger strain evidence a decrease in FWHM even for small R :** in other words, Regime I that was reported in Figure 3-9 is not observed here. Inserting a short creep period before stress reduction or performing a stress reduction in a compression test, allows running the transient at a well-defined quasi-stationary state; whereas in Figure 3-9 all stress drops were performed prior to the quasi-stationary flow stress.
- **The $\dot{\epsilon}$ - σ value near a given quasi-stationary state is similar and independent of strain path:** in a stress reduction test, the quasi-stationary flow stress reached after reloading is similar to that obtained by a continuous deformation test at the same loading rate. Also, the $\dot{\epsilon}$ - σ relationship reached in a multistep test or the flow stress reached in a continuous deformation test performed with a constant low strain rate provides similar $\dot{\epsilon}$ - σ values.

3.3 Stress reduction tests on nanocrystalline Ni₅₀Fe₅₀ alloy

This section reports on the *in situ* stress reduction tests performed on NC Ni₅₀Fe₅₀ alloy, for which both grain size and alloying composition are expected to have influences on the interplay between the deformation mechanisms. All stress reductions were carried out during continuous tensile deformation with loading rate $\dot{\epsilon}_{tot}$ of 10^{-3} /s except when mentioned otherwise.

3.3.1 Conventional stress reduction tests

For NC Ni₅₀Fe₅₀ alloy, the *in situ* conventional stress reduction tests series were carried out after a specimen was strained to either $\sigma_0 = 1.7$ GPa or 1.9 GPa. According to the yield criterion defined by L. Thilly *et al.* [149], macro-plasticity occurs at both stress levels. Table 3-3 provides an overview.

Table 3-3 Overview of all *in situ* conventional stress reduction tests done on NC Ni₅₀Fe₅₀.

Batch	Number of specimens	σ_0 (GPa)	R	Creep time	Instrument
NC Ni_35	10	1.7	0.27 ~ 1	30 min	<i>in situ</i>
	6	1.9	0.6 ~ 1	30 min	<i>in situ</i>

Creep after stress reductions

For $\sigma_0 = 1.7$ GPa, where macro-plasticity just starts, the evolution of the inelastic strain as well as the FWHM of {200} peak during 30 min creep are displayed in Figure 3-24a and b, respectively. The choice of the {200} peak for Ni₅₀Fe₅₀ is justified since it has the same behaviour as the {311} reflection but for this

material a higher signal-to-noise ratio. Inspection of the stress-dependent transient behaviours evidences the presence of three regimes that were also observed in Ni: Regime II, III and IV. Regime I where the FWHM continues to increase after a stress drop is not present in $\text{Ni}_{50}\text{Fe}_{50}$. With other words, no increase in FWHM is observed.

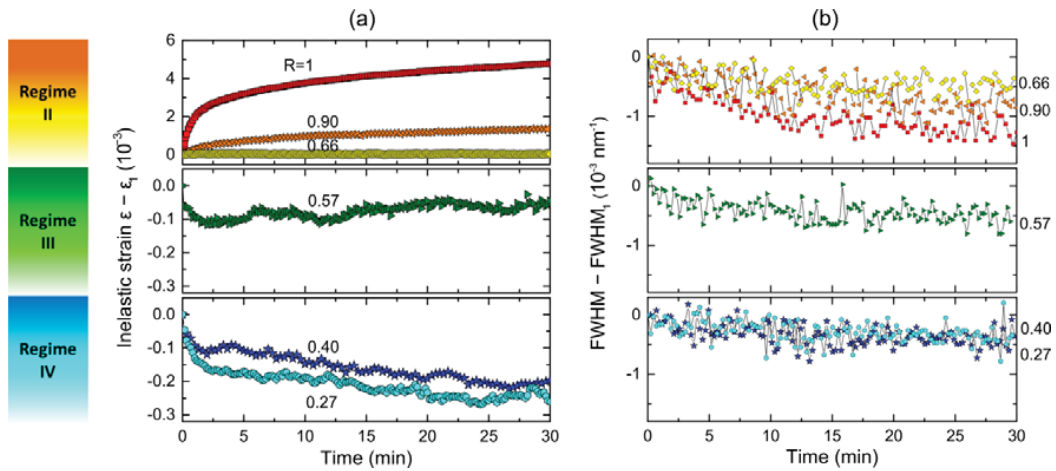


Figure 3-24 Results of standard *in situ* stress reduction tests series performed on NC $\text{Ni}_{50}\text{Fe}_{50}$. Transient responses depend on R for $\sigma_0 = 1.7$ GPa: (a) the inelastic strain, and (b) the FWHM of the {200} diffraction peak as a function of creep time. Three regimes can be distinguished. ϵ_1 and FWHM_1 refer to the values at the beginning of creep.

For the stress reduction tests series performed at $\sigma_0 \sim 1.9$ GPa, a significant change in {200} peak width is detected in comparison to the tests done at $\sigma_0 = 1.7$ GPa. In addition, the behaviour of the different peak families is not the same, in particular at $R = 1$. For this special case, the evolution of the inelastic strain as well as the FWHM for {111}, {200} and {311} diffraction peaks are displayed in Figure 3-25a. Interestingly, the FWHM for {200} peaks exhibits a significantly larger reduction compared to the other diffraction peaks. This peculiar behaviour has been confirmed in multiple experiments (not shown). In order to make a comparison with NC Ni, Figure 3-25b and c display the results for NC Ni_{65} and Ni_{35} at $R \sim 1$. In contrast to the case of NC $\text{Ni}_{50}\text{Fe}_{50}$ the FWHM for all peaks increase with time during the creep period. For Ni_{65} the FWHM of the {200} exhibits the smallest change, whereas for Ni_{35} this is the case for the {111} peak. This is most probably related to the different degree of texture in these two batches (Table 2-2) and will not be commented further.

Stress dependence of strain rate at constant microstructure

For NC $\text{Ni}_{50}\text{Fe}_{50}$, the stress dependence of strain rate after stress drops is shown in Figure 3-26, including the data points for $\sigma_0 = 1.7$ GPa (orange symbols) and 1.9 GPa (blue symbols). Performing a similar approach as for NC Ni, the data fitted with a solid curve is a sum of two exponential functions, shown as two dashed lines: one with slope 6.5 (left branch) and one with a steeper slope (right branch). The latter is drawn with only one experimental point, because the strain rate decreases considerably even after a very small drop 2% ($R = 0.98$). Compared with NC Ni batches, the slope of left branch in NC $\text{Ni}_{50}\text{Fe}_{50}$ is steeper (slope 4.6 for NC Ni_{35} and slope 5 for NC Ni_{65}).

3.3 Stress reduction tests on nanocrystalline Ni50Fe50 alloy

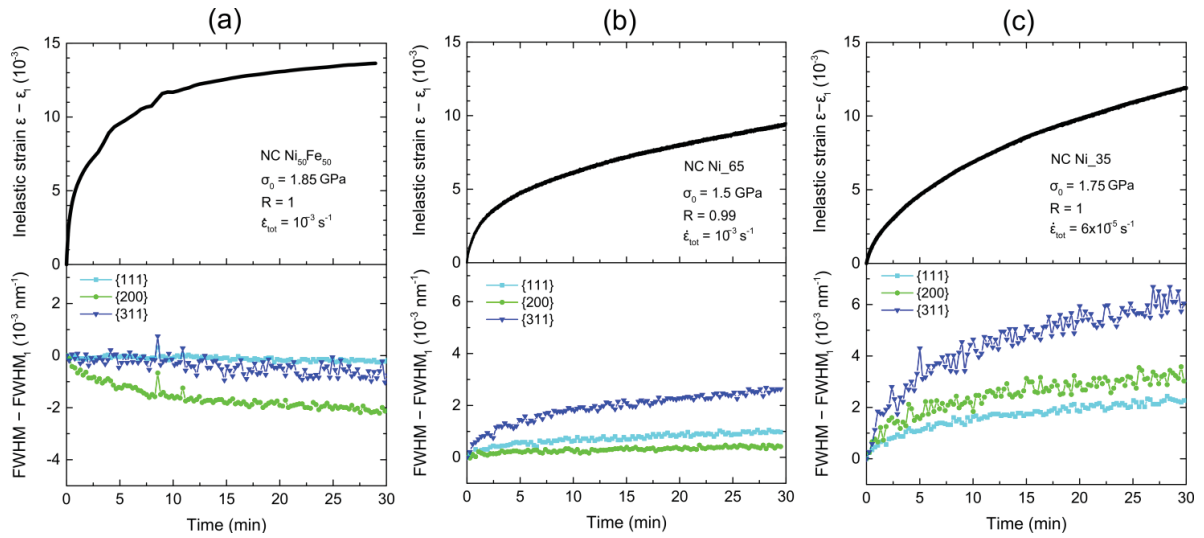


Figure 3-25 Evolution of the inelastic strain and the change of the FWHM for {111}, {200} and {311} diffraction peaks during transient creep at $R \sim 1$: (a) NC Ni₅₀Fe₅₀, (b) NC Ni₆₅, and (c) NC Ni₃₅. ϵ_1 and FWHM₁ refer to the values at the beginning of creep.

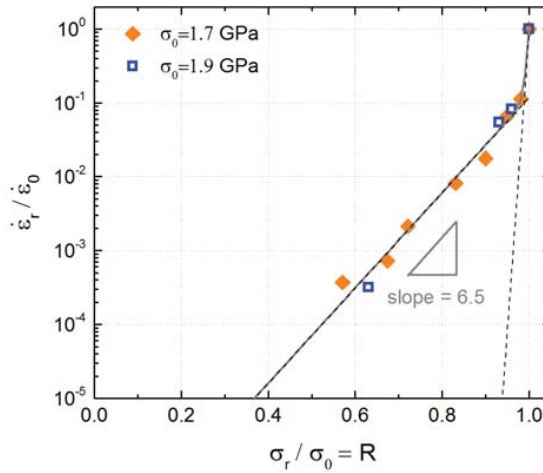


Figure 3-26 For NC Ni₅₀Fe₅₀, the normalized maximum forward strain rate $\dot{\epsilon}_r / \dot{\epsilon}_0$ is plotted logarithmically as a function of normalized reduced stress σ_r / σ_0 . All data points are fitted by a sum of two exponential functions (dashed lines). The solid line represents the resulting fit.

Reloading after transient creep

After the transient creep period the specimens were reloaded until failure with a loading rate of 10^{-3} /s. For NC Ni₅₀Fe₅₀, a yield point phenomenon during reloading is observed. Figure 3-27a shows the stress-strain curve for one stress reduction test with $R = 1$ at $\sigma_0 = 1.8$ GPa (black curve), and compares it with that for a continuous tensile test with the same loading rate (red dashed curve). They coincide with each other

except for the yielding point. Such overshooting is consistent with the previous observations during load-unload cycles and strain rate jump tests, and has been comprehensively discussed in Ref. [121].

In Figure 3-27b, the magnitudes of overshooting were examined by plotting the relative peak height $\Delta\sigma/\sigma$ versus the amount of prior inelastic strain produced before reloading. Here, $\Delta\sigma$ was taken as the difference between peak stress σ_{max} and the flow stress σ evaluated from back-extrapolation. It can be seen that $\Delta\sigma/\sigma$ depends on the strain produced prior to the reloading and increases in magnitude when more inelastic strain has been generated.

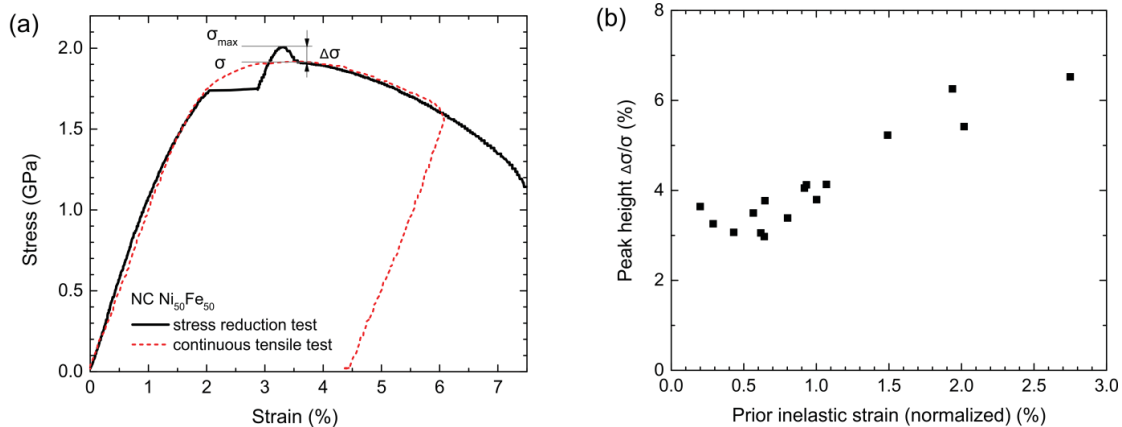


Figure 3-27 NC Ni₅₀Fe₅₀: (a) stress-strain curves for a conventional stress reduction test (black curve) and a continuous tensile test (red dashed curve) performed with the same loading rate. (b) shows the magnitudes of the overshooting plotted versus the amount of prior inelastic strain produced before reloading. The inelastic strain is normalized with respect to the strain produced at 1 GPa.

3.3.2 Multistep test

The *in situ* multistep test on NC Ni₅₀Fe₅₀ was conducted after straining the specimen to $\sigma_0 \sim 1.9$ GPa with a constant strain rate $\dot{\epsilon}_{tot}$ of 10^{-3} /s. Figure 3-28 provides an overview of the transient response after a stress reduction with $R = 0.58$. Figure 3-28a shows the stress-inelastic strain relation where the reduced stress is stepwise increased from 1.1 GPa to 1.8 GPa. Figure 3-28b and d display the strain rates as function of inelastic strain and applied stress. In the latter plot, the grey curve is taken from the $\dot{\epsilon}_r$ -curve (solid line) in Figure 3-26; the pink line is taken from Ref. [113], showing that the maximum flow stresses measured at constant strain rates are very similar. After a large stress reduction, the initial strain rate is negative (anelastic back flow) and reaches $\dot{\epsilon}_{r,max}$ (red dot) after creeping for a while. The $\dot{\epsilon}_{r,max}$ is not far away from the $\dot{\epsilon}_r$ -curve. In contrast to NC Ni, the strain rate in the last step is quite distant from the pink line and showing a continuously decreasing trend. Also, the inelastic strain produced during transients is much less, even for creeping at the highest stress levels.

3.3 Stress reduction tests on nanocrystalline Ni₅₀Fe₅₀ alloy

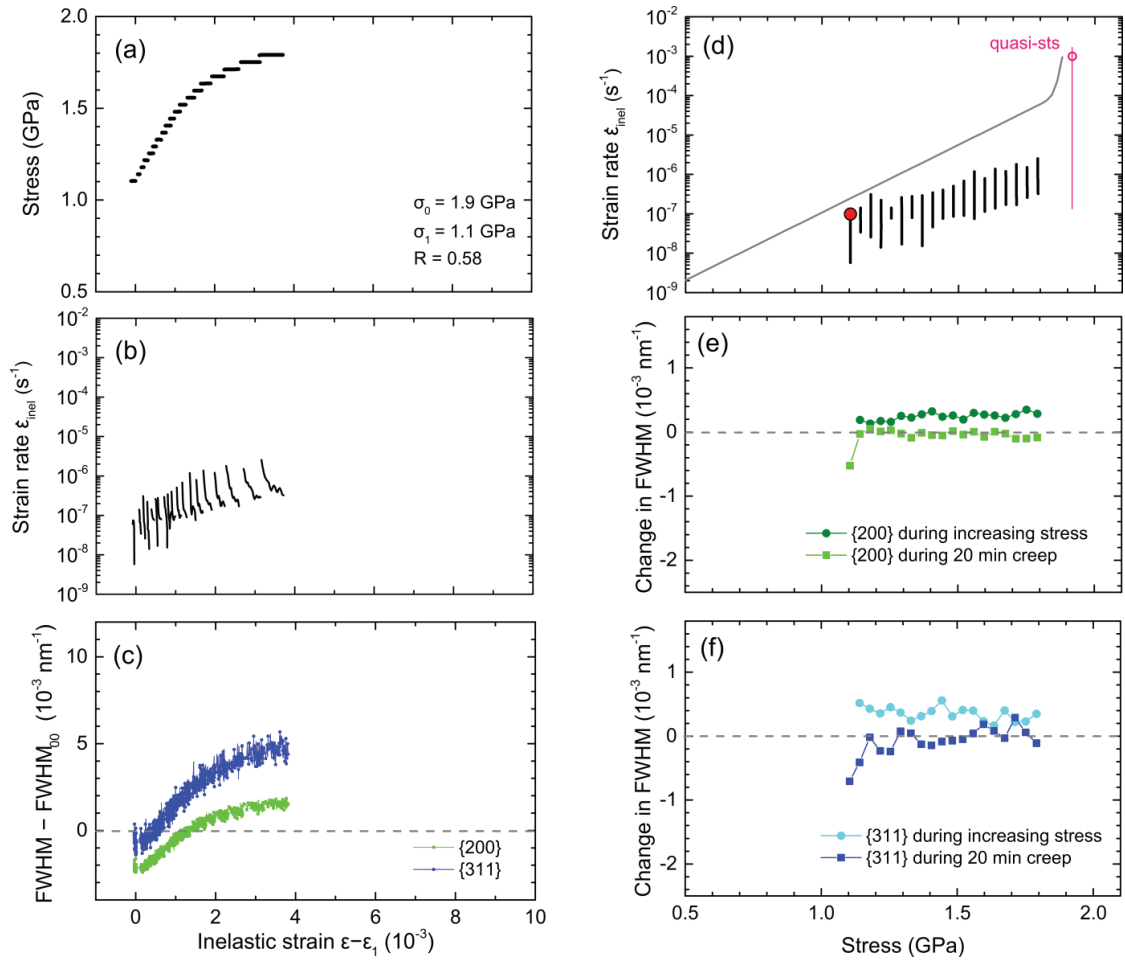


Figure 3-28 Overview of transient behaviour during the *in situ* multistep tests for NC Ni₅₀Fe₅₀: (a) the stress-inelastic strain relation; (b) and (d) creep rates as function of inelastic strain and applied stress; (c) the overall behaviour of the FWHM for {200} and {311} peaks as a function of the inelastic strain; (e) and (f) decouple the overall change of the FWHM into contributions from 20 min creep periods (square symbols) and from stepwise stress increasing (circle symbols), and display the change as a function of the applied stress.

Figure 3-28c shows the corresponding evolution of the FWHM for {200} (green curve) and {311} (blue curve) diffraction peaks. It is noted that the overall shape of FWHM curves are similar to that of stress-inelastic strain relation. This implies that the stepwise increased stress is the main contributor to the change of FWHM during transients. This is demonstrated in Figure 3-28e for {200} peak and Figure 3-28f for {311} peak, in which the two contributions of the FWHM are decoupled (similar to the case of NC Ni in Figure 3-22). Clearly the change in the FWHM is mainly determined by the applied stress, except immediately after the large stress reduction where a reduction in FWHM also occurs during creep. When increasing the stress levels further no significant change in FWHM is observed during the 20 min creep periods.

3.3.3 Summary

Note that the FWHM of the {200} peak is mainly used for Ni₅₀Fe₅₀ due to its qualitatively similar behaviour as the {311} peak but higher signal-to-noise ratio. The results of *in situ* stress reduction tests for Ni₅₀Fe₅₀ show some similarities but also some differences compared to NC Ni.

Similarities are:

- Anelastic backstrain for large stress reductions: this is evidenced when stress reductions with $R < 0.6$ were performed.
- Softening during large/ medium stress reduction: assuming that the pink line in Figure 3-28 represents the quasi-stationary state, the forward strain rate after a stress reduction lies on the left side of the line.
- The microstructure “hardens” while approaching the quasi-stationary state: this is evidenced by a continuous decline in strain rate at constant stress, or by a stepwise increase in stress at similar strain rates.
- The strain rate can be decomposed into two contributions with respective high and low stress sensitivity: for the left branch where the slope is lower, the FWHM always decreases with creep time, showing the presence of GB-mediated mechanisms.

Differences are:

- The lack of Regime I where both strain and FWHM increase after a small stress drop: for NC Ni₅₀Fe₅₀, the stress reductions performed at $\sigma_0 = 1.7$ GPa and ~ 1.9 GPa always observe a reduction in FWHM irrespective of R for
- A peak family dependent FWHM evolution is only observed when the applied stress is kept constant ($R = 1$) at higher σ_0 : this is observed for $\sigma_0 \sim 1.9$ GPa, as shown in Figure 3-25.
- A yield point is observed upon reloading, and the magnitude of the overshooting depends on the strain reached prior to the reloading.
- In a multistep test, there is very limited inelastic strain generated and \a lack of FWHM increase when creeping at high stress levels: after a large stress reduction, the FWHM decreases for initial creep steps; upon further increasing stress, the FWHM hardly changes while keeping the stress constant.

3.4 Grain size evaluation

In order to explore the role of grain coarsening during deformation, the grain sizes during/ after deformation were derived from X-ray diffraction patterns. Post-mortem TEM analysis was also carried out.

3.4.1 *In situ* X-ray diffraction

The grain size evolution during deformation was measured in the *in situ* load-unload cycles (Section 2.4.3). In order to minimize the influence of anelastic back flow on the peak width, the grain size measurement starts after having waited 10 min upon unloading.

Figure 3-29a, c, and e display the stress-strain curves of load-unload cycles for Ni₃₅, Ni₆₅, and Ni₅₀Fe₅₀, and Figure 3-29b, d, and f show the corresponding evolution of grain size as a function of plastic strain. It

3.4 Grain size evaluation

can be seen that the plastic strain achieved through uniaxial tensile testing is in the order of a few percent (< 4 %). In the last unloading cycle, the grain diameter is increased by 4.2 % for Ni_35, 7.3 % for Ni_65, and 12.5 % for Ni₅₀Fe₅₀. Overall, there is only a minor change in grain size.

3.4.2 Post-mortem TEM

Larger strain up to > 20 % can be generated in compression. In order to examine the change in grain size after a larger deformation, post-mortem TEM was performed on one of NC Ni_35 samples that had been continuously deformed in compression (see Section 3.1.1). Figure 3-30a and b display the TEM micrograph as well as the grain size distribution for a lamella taken perpendicular to the sample surface (cross-section), and Figure 3-31a and b show that for a lamella parallel to the surface (in-plane). Table 3-4 provides a comparison of average grain size between non-deformed and deformed state. The grain size in cross-section and in-plane are increased by 40% and 50 % respectively.

3.4.3 Summary

The grain size evolution during/ after deformation can be summarized as follows:

- During uniaxial tensile testing, limited plastic strain is generated (< 4 %) and the change in grain size is minor for all materials investigated.
- During uniaxial compression testing, a modest grain coarsening has been observed when a NC_35 sample was largely deformed up to a total strain ~ 20 %. Figure 3-32 presents the grain size distributions of non-deformed (open symbols) and deformed states (solid symbols) in cumulative percent. This result is in contrast to the observation in Ref. [51] where after a comparable amount of deformation the ED NC Ni specimen from Goodfellow exhibits minor grain growth. Such different behaviours should arise from the materials that contain different amounts of impurities during electrodeposition process.

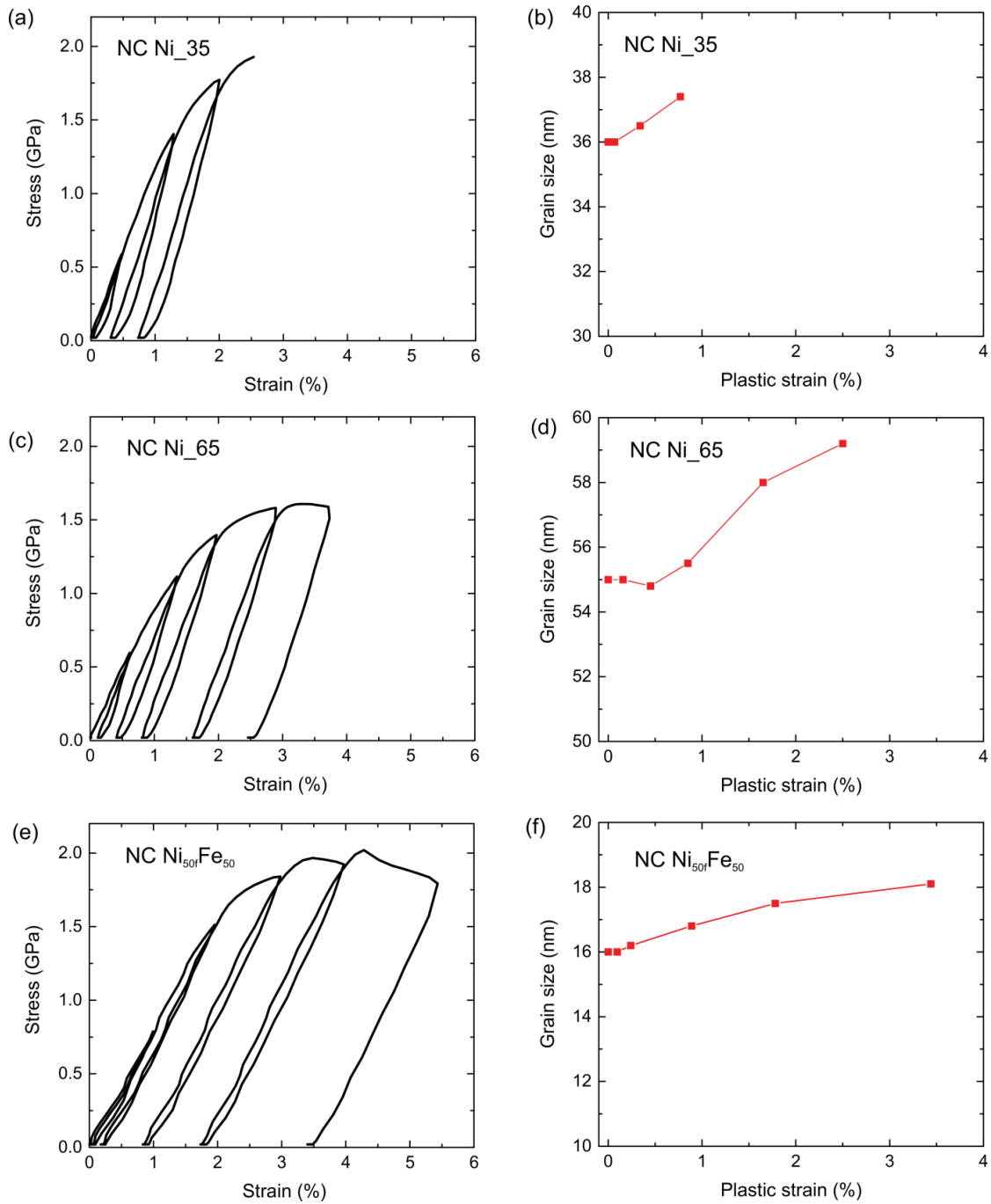


Figure 3-29 Stress-strain curves of load-unload cycles and the corresponding evolution of grain size during/ after deformation measured from X-ray diffraction patterns: (a, b) for NC Ni₃₅, (c, d) for NC Ni₆₅, and (e, f) for NC Ni₅₀Fe₅₀.

3.4 Grain size evaluation

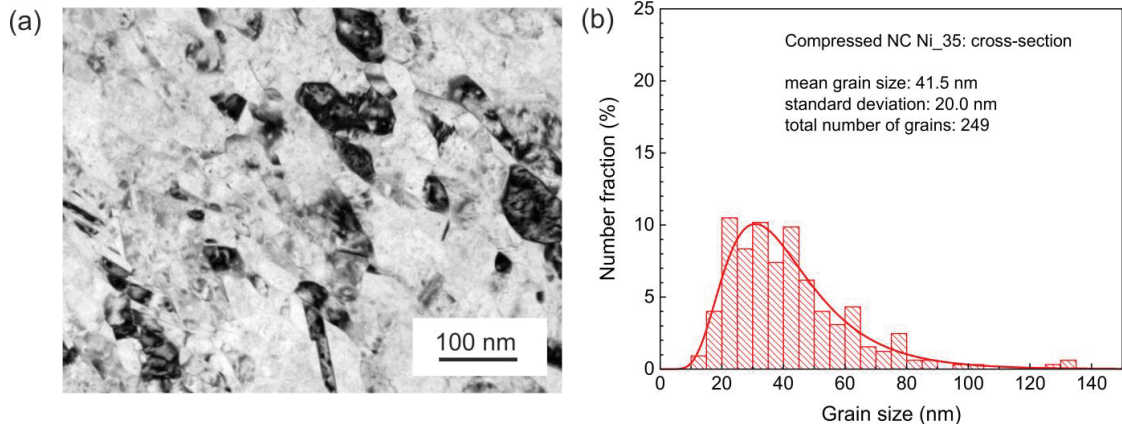


Figure 3-30 Cross-section view of as-deformed NC Ni₃₅ with a total strain up to 20 %: (a) a bright field TEM image and (b) grain size distribution.

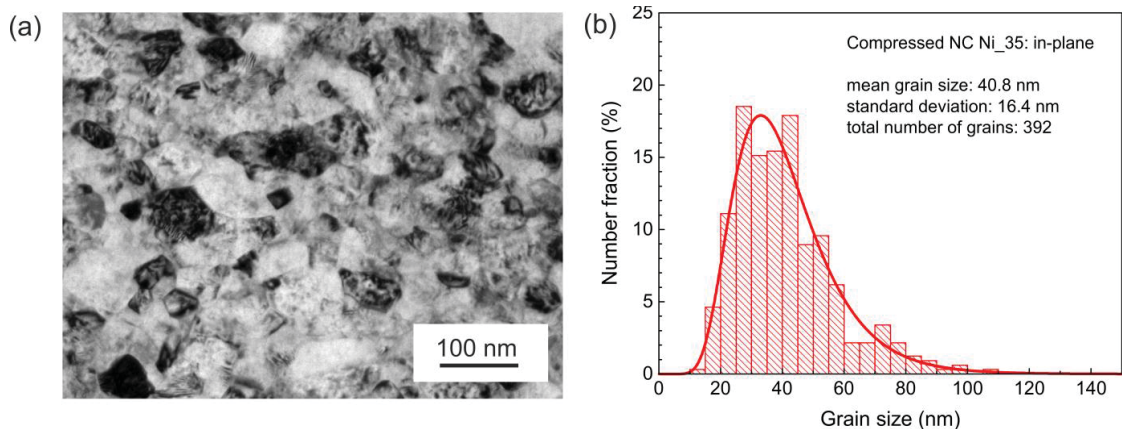


Figure 3-31 In-plane view of as-deformed NC Ni₃₅ with a total strain up to 20 %: (a) a bright field TEM image and (b) grain size distribution.

Table 3-4 A comparison of average grain size between non-deformed and deformed state.

	Cross-section	In-plane
Initial grain size (nm)	29.8 ± 12.2	27.2 ± 12.0
Deformed grain size (nm)	41.5 ± 20.0	40.8 ± 16.4
Increment (%)	40.0	50.0

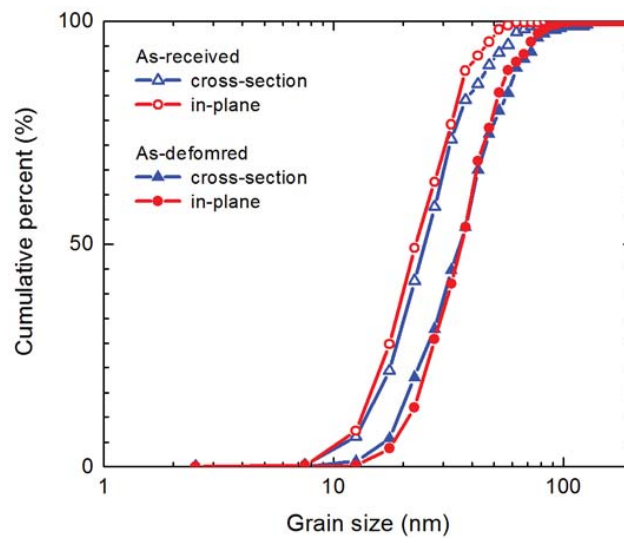


Figure 3-32 Grain size distribution of non-deformed and deformed states presented in cumulative percent.

Chapter 4 Molecular dynamics simulation results

Inspired by the results of experimental transient testing, MD simulations of stress drops were performed. The simulations have been carried out with LAMMPS by Dr. Christian Brandl (Karlsruhe Institute of Technology), and the analysis has been performed in the framework of this thesis. NC Al was simulated instead of Ni because the empirical potential of Al allows evidencing the nucleation of both leading and trailing partial dislocations within the nanosecond simulation time frame [20]. Also, this allows direct comparison with previous simulations in Refs. [13][14][23].

4.1 Overview of stress reduction tests series

Figure 4-1 displays the MD simulated stress-strain curve for a NC Al sample deformed at room temperature at a constant strain rate of 10^8 /s. Conventional stress reduction tests series were carried out when the sample was strained to an engineering strain of 5.2 % where the flow stress reached $\sigma_0 = 1.52$ GPa. Similar to the experiments performed in Section 3.2.1, the relative reduced stress R covers a wide range of values ranging from 0.92 to 0.33. At each reduced stress level the specimen was allowed to creep 1700 ps.

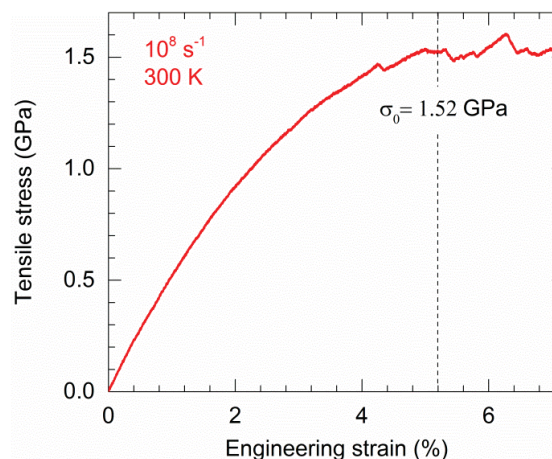


Figure 4-1 A simulated stress-strain curve for a NC Al sample deformed at room temperature at a constant strain rate of 10^8 /s

Figure 4-2a displays the corresponding strain-time curves during creep periods. Notably, these curves are found to be stress-dependent, and exhibit similar trends as those found in the *in situ* experiments. For each

4.1 Overview of stress reduction tests series

relative reduced stress R , Figure 4-2b evaluates the number of mobile dislocations propagating during the creep periods. It is found that after the stress drop, dislocation activity including nucleation and propagation events are largely suppressed with decreasing R . In the case of a moderate stress drop, sometimes freshly nucleated dislocations can propagate after a certain incubation period. For large enough stress drops such as $R = 0.53$ and 0.33 , nucleated dislocations do not propagate anymore. However in one case where the dislocation had already propagated till the middle of the grain, the dislocation was observed to continue to propagate after the stress drop. This is displayed in Figure 4-3: $t = 0$ ps and $t = 4$ ps represent the configurations immediately after the stress drop ($R = 0.53$) and during creep, respectively. For simplicity, here FCC atoms are not shown. The arrow indicates the propagation direction.

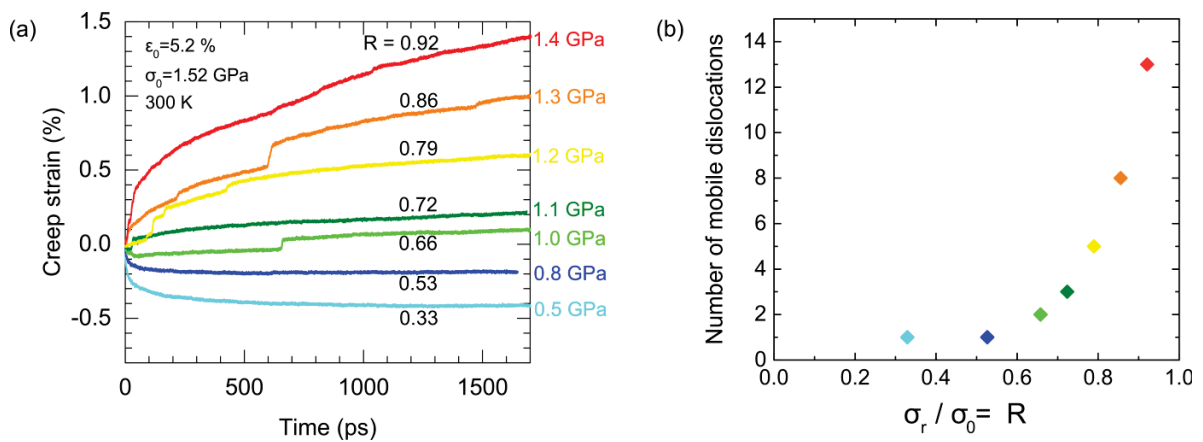


Figure 4-2 (a) For the simulated stress reduction tests series, the trends of strain-time curves during creep periods are found to be R dependent and similar to those of *in situ* experiments. (b) After different magnitudes of the stress drops, the number of mobile dislocations propagating in the grain interiors decreases with decreasing R .

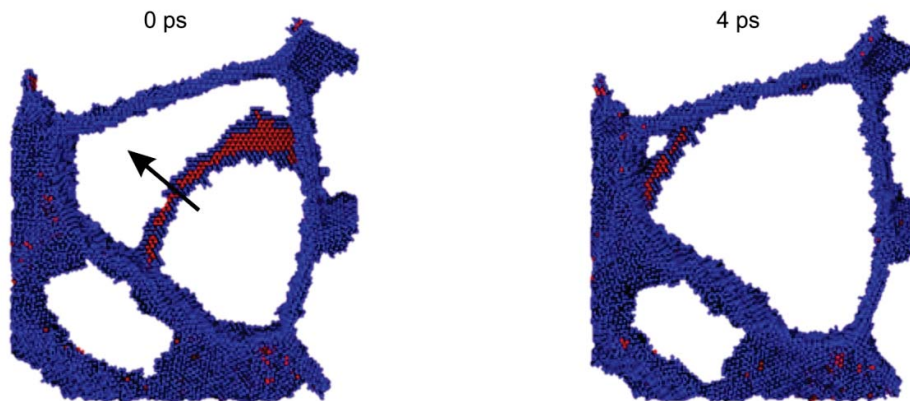


Figure 4-3 After a stress reduction with $R = 0.53$, one dislocation formed during prior deformation sits in the middle of one grain, see $t = 0$ ps. During subsequent creep, this dislocation continues propagating, e.g. $t = 4$ ps, until being absorbed at the GBs. The atoms are coloured based on CNA analysis, see Section 2.5.3. FCC atoms are not shown for simplicity. The black arrow indicates the propagation direction.

4.2 A medium stress reduction with longer creep

4.2.1 Dislocation emission

In addition to the previous stress drops, one additional test with $R = 0.86$ is followed during a longer creep period of 2290 ps. Figure 4-4 shows the creep strain versus time curve. Each pronounced strain burst can be ascribed to the continuous propagation of a dislocation across the grain. It can be seen that in the initial creep period several slip events occur one after another, respectively in the grains of G13, G2, G10, and G8. As the strain rates decline with creep time, strain bursts become more separated in the time and can be associated with slip events in G9 at $t = 850$ ps and in G14 at $t = 2226$ ps.

In the present work, dislocation events in G14 are particularly followed: there are two dislocations Dis1 and Dis2 successively emitted into G14 within a time interval of ~ 800 ps, as indicated by grey arrows in Figure 4-4. However, they propagate very slowly and generate very limited strain. At $t = 226$ ps a remarkable increase of their travelling speed enables them to travel across the grain very fast, leading to the strain burst. The insert in Figure 4-4 presents G14 (centred) and its neighbouring grains. The viewing direction for G14 is perpendicular to the (-111) slip plane.

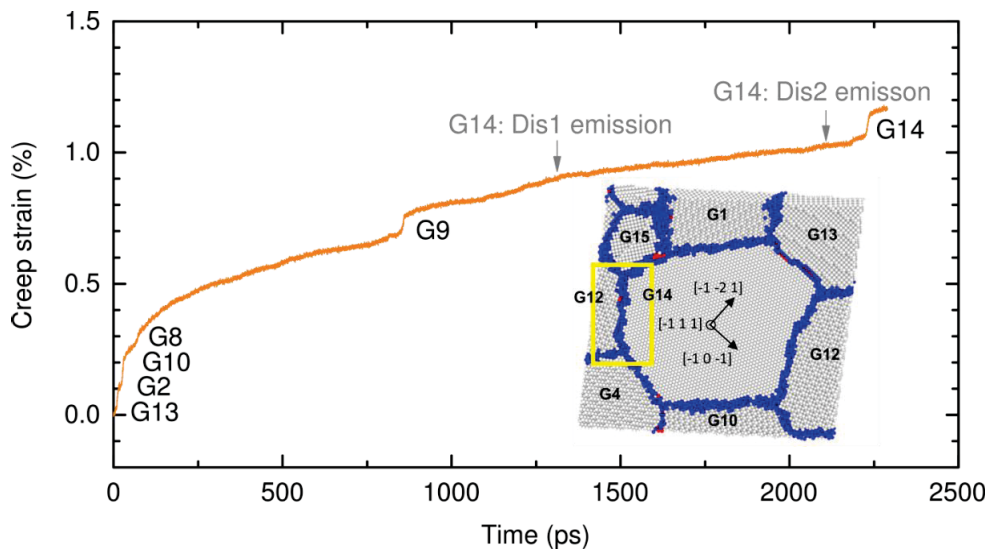


Figure 4-4 Creep strain versus time curve for the additional stress reduction test with $R = 0.86$ followed by a creep period of 2290 ps. Each slip event in the grain is indicated on the curve. The insert presents G14 (centred) and its neighbouring grains. The viewing direction for G14 is perpendicular to the (-111) slip plane. Atoms are coloured based on CNA analysis.

A detailed inspection of dislocation nucleation and propagation was carried out in the rectangular region (yellow) marked on the insert in Figure 4-4. The GB between G12 and G14 (GB 12-14) is a general GB with a twist and a tilt component. Figure 4-5 displays a series of snapshots of this region with 4 atomic layers perpendicular to the viewing direction. The orientation has been adjusted to visualize the continuity of $\{111\}$ lattice planes from G12 to G14.

4.2 A medium stress reduction with longer creep

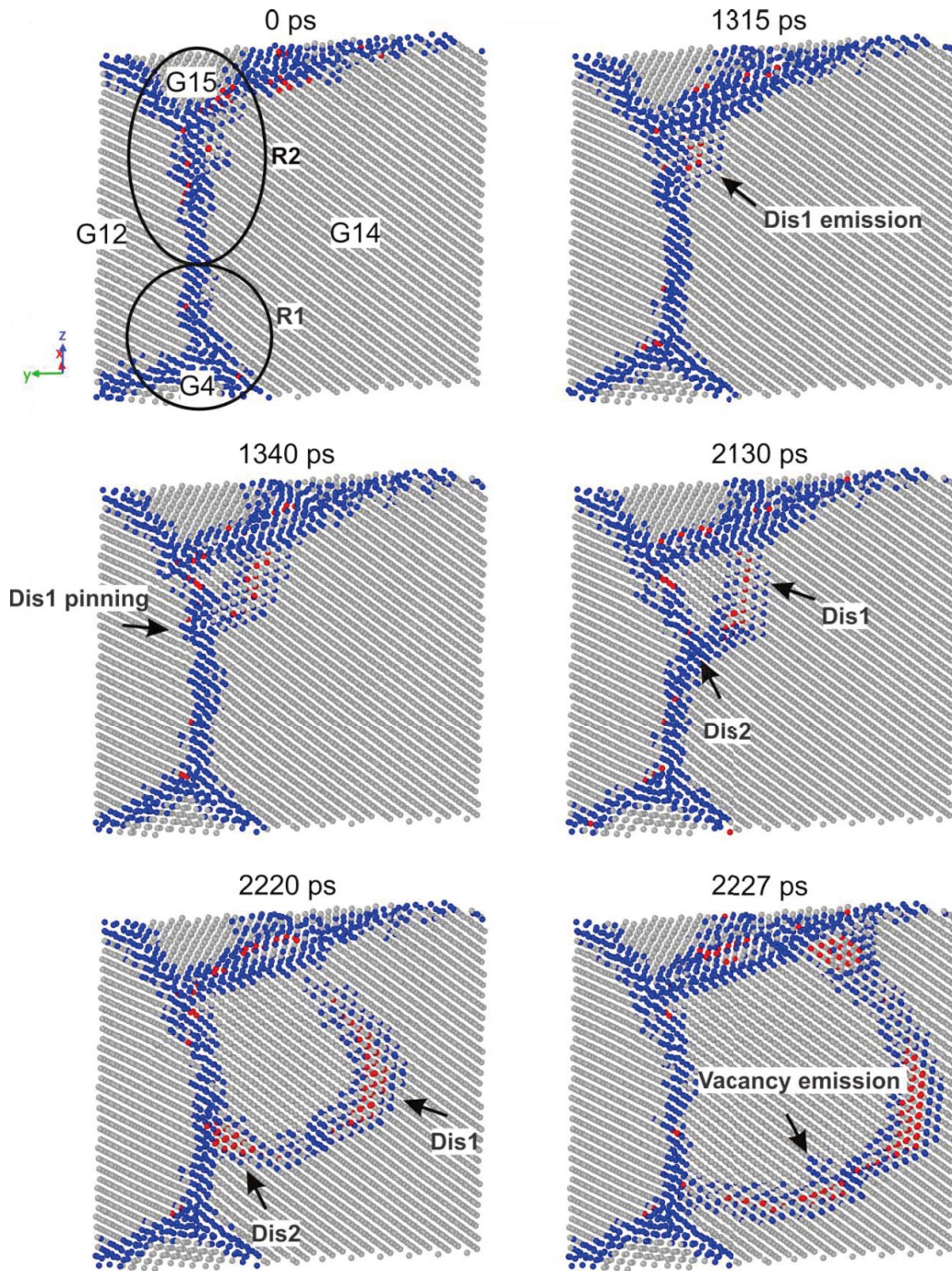


Figure 4-5 Snapshots of a zoom-in of the rectangular region as indicated in Figure 4-4. The arrows indicate different dislocation and GB activity during creep. Atoms are coloured based on CNA analysis.

In Figure 4-5, it is found that immediately after the stress drop ($t=0$ ps) GB 12-14 is relatively planar except for a ledge close to the TJ 12-4-14, as indicated by the circled R1 region. Also, GB 12-14 contains several dislocation embryos that have been already created during prior loading. Only one is capable of

evolving in a full emission of a dislocation into G14 after several trials and errors. This is observed at $t = 1315$ ps when a trailing partial is emitted from the site nearby TJ 12-15-14, i.e. in the circled region R2. After that the full dislocation Dis1 propagates until it stays pinned at $t = 1340$ ps. Further propagation after unpinning occurs only at $t = 2085$ ps. Soon afterwards, a new dislocation Dis2 is freshly nucleated ($t = 2100$ ps) from GB 12-14. The emission of Dis2 is observed to interact with Dis1, causing a local migration of the GB and the formation of another ledge structure, as shown in the snapshot of $t = 2130$ ps. Dis1 and Dis2 have the same Burgers vector but opposite sign on the (-111) slip plane. They are separated by $2d_{111}$, where d_{111} denotes the interplanar spacing of $\{111\}$ planes. Also, the interaction of Dis1-Dis2 forms a jog that is dragged along with the Dis1-Dis2 motion inside G14, e.g. $t = 2220$ ps. At $t = 2226$ ps, Dis1 and Dis2 are observed to travel at a much higher speed across the grain and leave a vacancy behind, e.g. $t = 2227$ ps. The details of the mechanisms are discussed in the paragraphs below.

4.2.2 Dislocation-dislocation interaction

Figure 4-5 has shown that the motion of the jog formed by the Dis1-Dis2 interaction produces a vacancy inside the grain. This process is further inspected in Figure 4-6 where the atomic potential energy at the selected time configurations is followed. The colour bar gives the potential energy ranging from -3.4 eV (blue) to -3.1 eV (red).

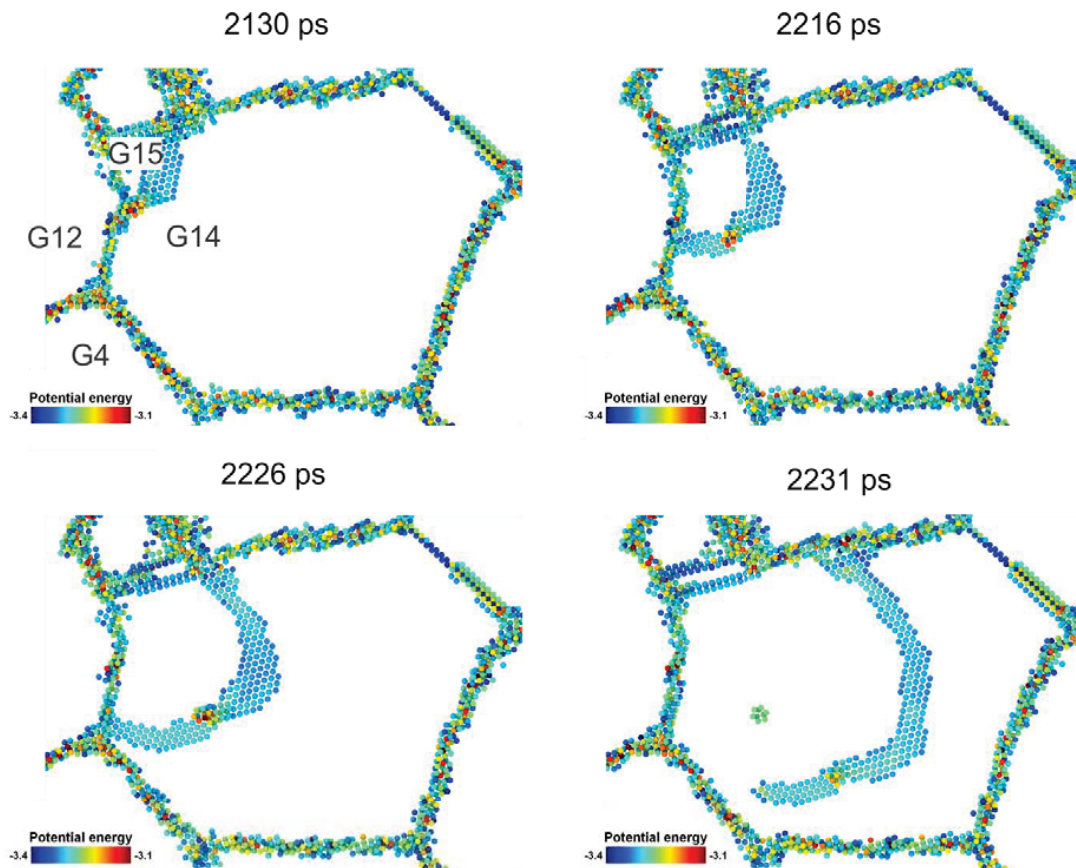


Figure 4-6 Dis1-Dis2 interaction followed by a jog motion producing a vacancy inside the grain. The atoms are coloured based on atomic potential energy analysis. The potential energy ranges from -3.4 eV (blue) to -3.1 eV (red).

4.2 A medium stress reduction with longer creep

In Figure 4-6, it is seen that during their initial interaction at $t = 2130$ ps, a pentagon-shaped point defect containing a partial vacancy is created at the jog. Note that the atoms surrounding this partial vacancy exhibit relatively high potential energy (a maximum value of -3.1 eV) when compared to the value for the non-FCC atoms in the grain interior (-3.36 eV). As the jog is dragged along with the motion of Dis1-Dis2, e.g. $t = 2216$ ps, a vacancy is eventually formed from the prior partial vacancy and emitted at $t = 2226$ ps when Dis1-Dis2 travels at pronouncedly enhanced rates by overcoming the pinning site at the GB 15-14. In the end, Dis1-Dis2 travels across the entire G14 and gets absorbed at the GBs. Here the emission of the vacancy from the jog results in a jog configuration that is energetically more favourable. This is evidenced by a decrease of the atomic potential energy in the jog, e.g. $t = 2231$ ps. Further investigation is required for a better understanding of the mechanisms behind this process.

4.2.3 GB-mediated accommodation

GB dislocations to accommodate misfit

During the creep periods, there is a lot of GB activity, as for instance in region R1 (as indicated in Figure 4-5). Figure 4-7 shows a zoom-in of this region, in which the configurations short after the stress reduction ($t = 0$ ps) and at the time of a full emission of Dis1 ($t = 1315$ ps) are compared in terms of their atomic arrangement and local hydrostatic pressure.

At $t = 0$ ps, there is a clear coherence across the GB between a set of $\{111\}$ planes in G12 and in G14 (dotted lines) separated by a GB dislocation (GBD) as indicated by the yellow line. Close to the dislocation, the GB contains also a ledge. By the time of $t = 1315$ ps, this GBD is observed to move upwards by a distance of $2d_{111}$, the ledge is eliminated, and the TJ 12-4-14 migrates. Inspection of the relative atomic displacement vectors between these two time frames indicates that atomic shuffling and diffusion along the GB (parallel to the loading z axis) are involved. Also, the GBD upwards motion and the removal of the ledge causes an increase of local compressive stress inside G12, represented by reddish colours. In Ref. [13] climb of GB dislocations was already observed, which was associated with the nucleation of lattice dislocations. Here the motion of similar dislocations and the removal of the ledge structure is a clear evidence of GB sliding.

Figure 4-8 provides an overview of GB accommodation after the stress reduction, where the shear strain evolution at the GBs is demonstrated in the simulated box. Three different configurations with time frames of $t = 400$ ps, 1315 ps, and 2290 ps are selected. The colour bar scales the shear strain value ranging from 0 (white) to 0.2% (dark blue). One can clearly see that the development of shear strain at the GBs is quite heterogeneous during the long-term creep periods. This suggests that the GB accommodation processes are strongly dependent on the GB characters.

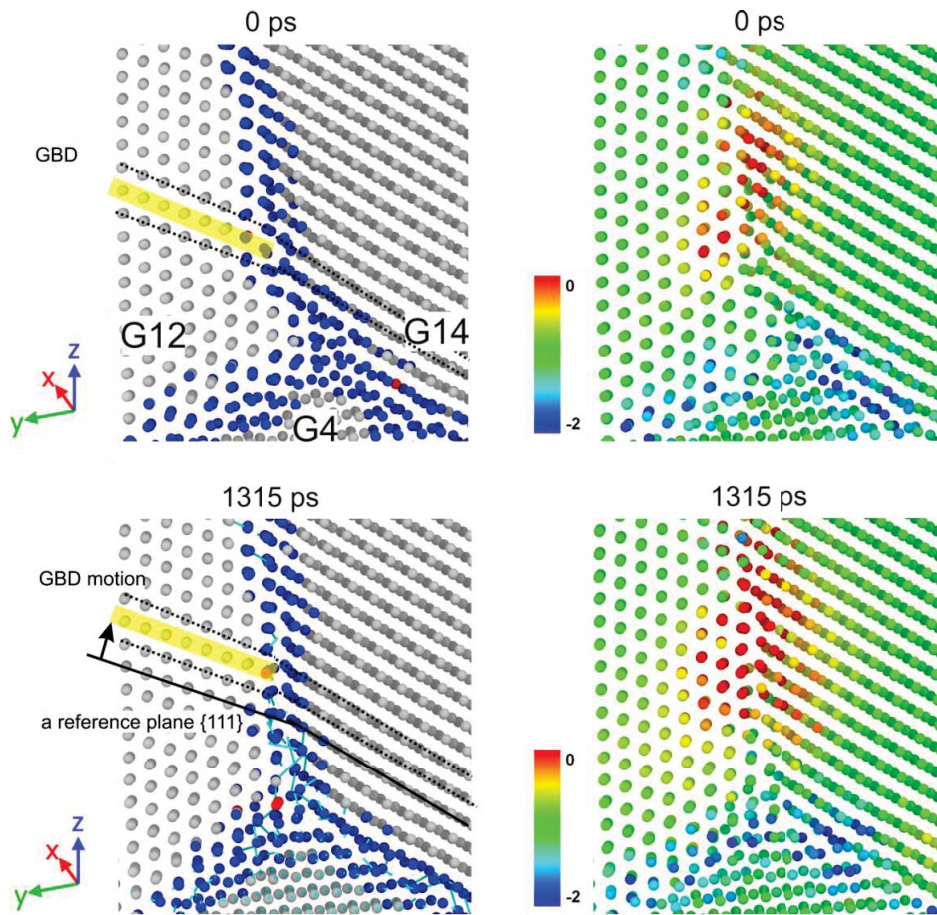


Figure 4-7 Snapshots of a zoom-in of the circled region R1 as indicated in Figure 4-5: $t = 0$ ps and $t = 1315$ ps represent the configurations short after the stress reduction and at the time of a full emission of Dis1, respectively. The analysis of CNA and local hydrostatic pressure are applied. The red colour is representative for compressive stress field while blue for tensile.

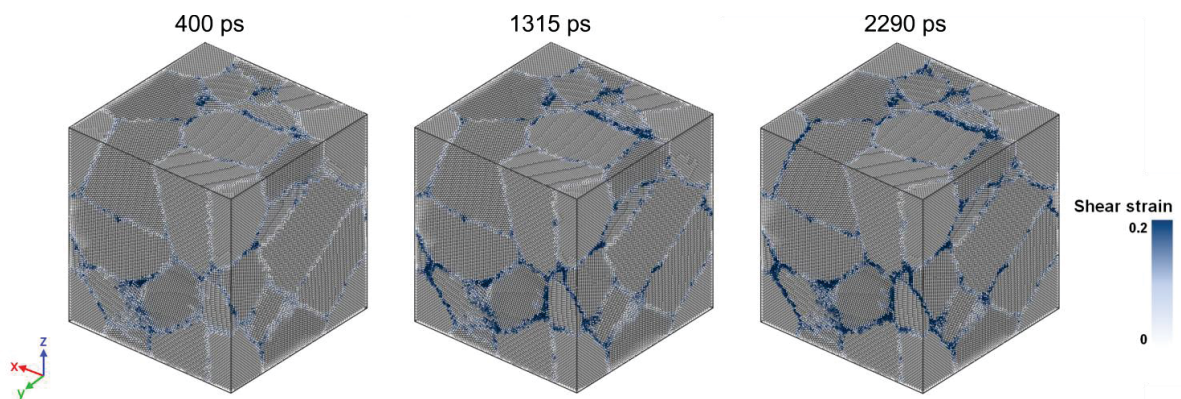


Figure 4-8 After the stress reduction the shear strain at the GBs increases with creep time, and it is heterogeneously developed among the GBs. The colour bar scales the shear strain value ranging from 0 (white) to 0.2% (dark blue)

Misfit region and pinning of lattice dislocation

Figure 4-9 shows a zoom-in of the circled region R2 as indicated in Figure 4-5. Here, another misfit region across $\{111\}$ planes in GB 12-14 is detected as indicated by the yellow transparent ellipse. At $t = 0$ ps, this misfit region is delocalized involving 4-5 $\{111\}$ planes on both sides of GB 12-14. To facilitate the comparison of the misfit region at different time frames, a reference plane (black line) is selected. It is noted that by the time of a full emission of Dis1 ($t = 1315$ ps) the misfit region confines, and a ledge in the GB structure is formed, acting as a pinning site ($t = 1340$ ps) for further propagation of Dis1. When Dis1 unpins at $t = 2085$ ps, the ledge structure in the GB is removed. This is visualized in Figure 4-10 where a comparison of configuration before/ after unpinning is made. Also, the misfit region is confined to a GBD of the same type as the one described previously. Inspection of the relative atomic displacement vectors (light blue in Figure 4-9) indicates an assistance of atomic diffusion along GBs in this process.

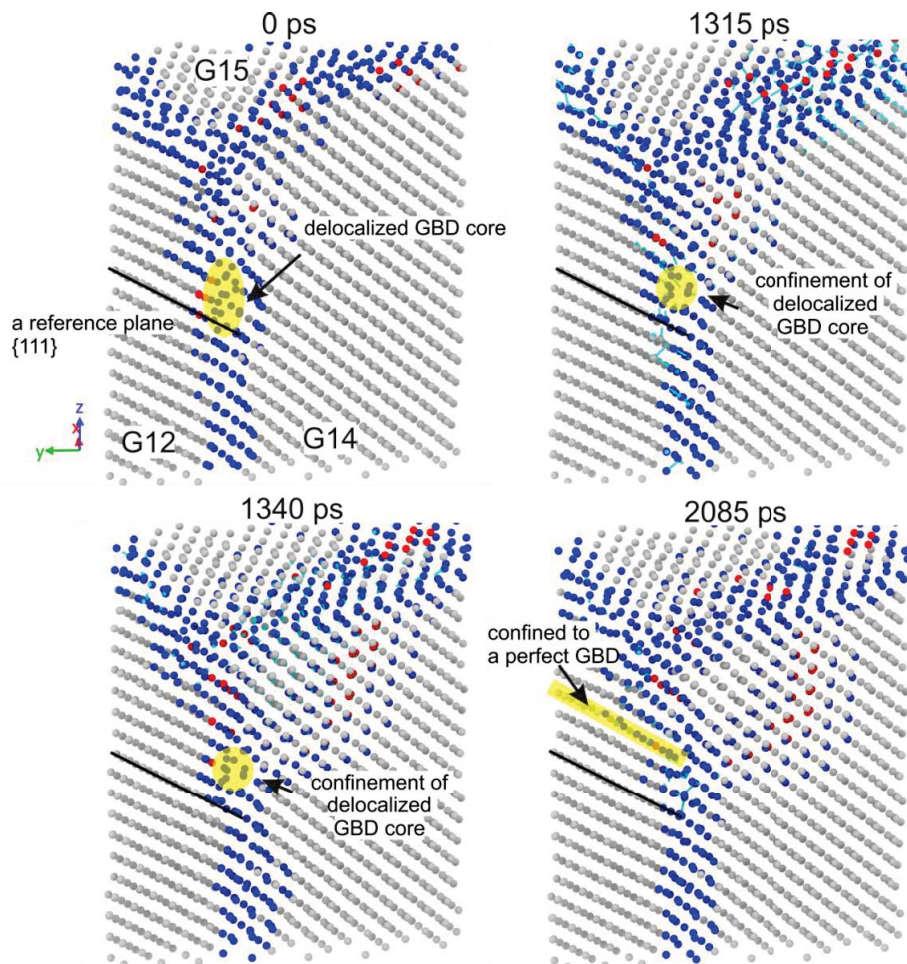


Figure 4-9 Snapshots of a zoom-in of the circled region R2 as indicated in Figure 4-5. The configurations short after the stress reduction ($t = 0$ ps), at the time of a full emission of Dis1 ($t = 1315$ ps), and at the time of Dis1 pinning ($t = 1340$ ps) and unpinning ($t = 2085$ ps) are compared in terms of atomic arrangement (CNA analysis). The atomic displacements (light blue) show the relative change between 1315 ps and 0 ps, 1340 ps and 1315 ps, and 2085 ps and 1340 ps, respectively.

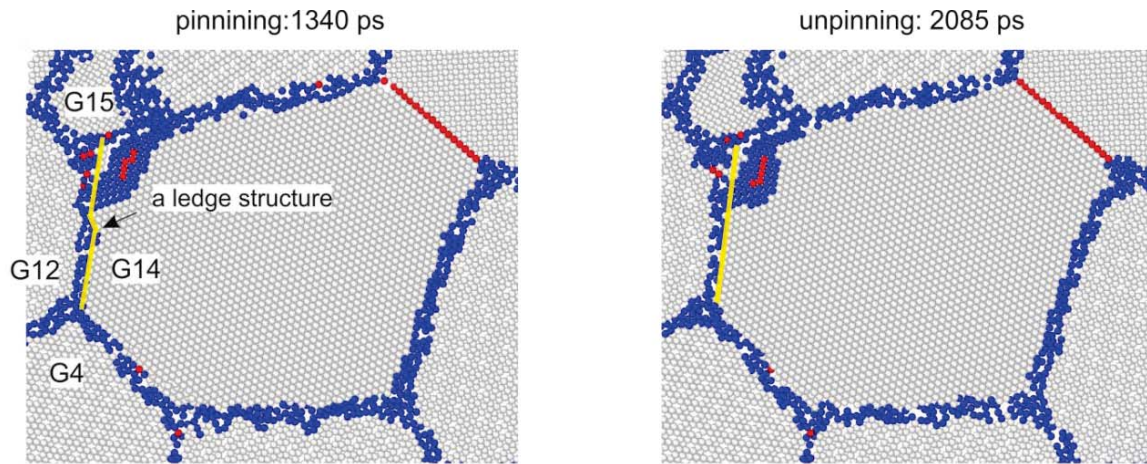


Figure 4-10 Upon Dis1 unpinning a ledge structure in the GB is removed. A viewing direction is perpendicular to the slip plane (-111). Atoms are coloured based on CNA analysis.

Atomic diffusion along GBs

It has been observed that the processes described above involve atomic diffusion along the GB 12-14 plane. In Figure 4-11, further inspection on GB diffusion mechanism is carried out in the rectangular region as indicated in Figure 4-4. The configurations at time frames of $t = 400$ ps, 1315 ps, and 2085 ps are selected. The atomic displacements (light blue) show the relative change between 400 ps and 0 ps, 1315 ps and 400 ps, and 2085 ps and 1315 ps, respectively. It is clearly seen that long diffusion paths occur at different sites of GBs as indicated by the arrows. Compared to the usual high strain rates used in continuous deformation simulations [14][142], the slower strain rates observed after the stress drop enhance these accommodation processes in the GBs.

GB migration

In Figure 4-7 local GB migration associated with removing GB ledge has been observed at the site near TJ 12-4-14. This event occurred prior to a full emission of Dis1. Figure 4-12 demonstrates another event of local GB migration that occurs upon Dis2 nucleation and emission. The same region R1 as indicated in Figure 4-9 is inspected. It is seen that as Dis2 is nucleated from the GB 12-14 at $t = 2100$ ps, GB migrates locally. Dis2 emission interacts with Dis1, and both slip to some extent into the G14. This is accompanied by further local migration of GB 12-14, during which more ledge structures are formed, see $t = 2195$ ps. Once Dis 2 has propagated slightly further at $t = 2196$ ps, part of the migration of GB 12-14 seems to have been recovered. One can assume that this is related to the motion of the jog, it needs however further detailed analysis.

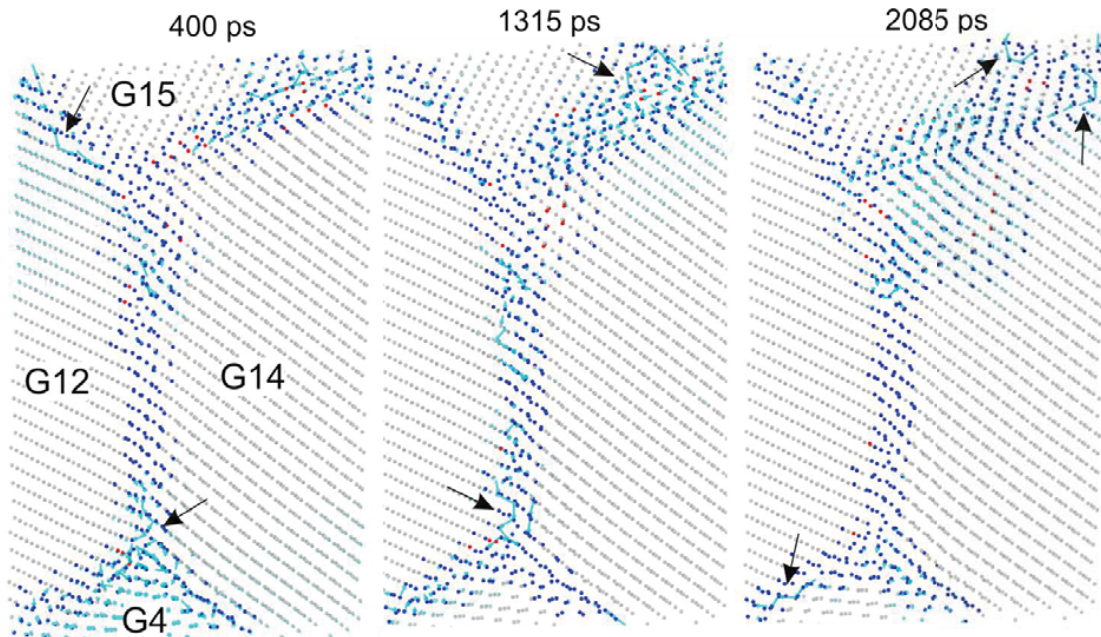


Figure 4-11 Snapshots on the zoom of the rectangular region as indicated in Figure 4-4. The configurations at time frames of $t = 400$ ps, 1315 ps, and 2085 ps are selected ; the atomic displacements show the relative change between 400 ps and 0 ps, 1315 ps and 400 ps, and 2085 ps and 1315 ps, respectively. The arrows mark the sites where long diffusion paths in the GBs occur.

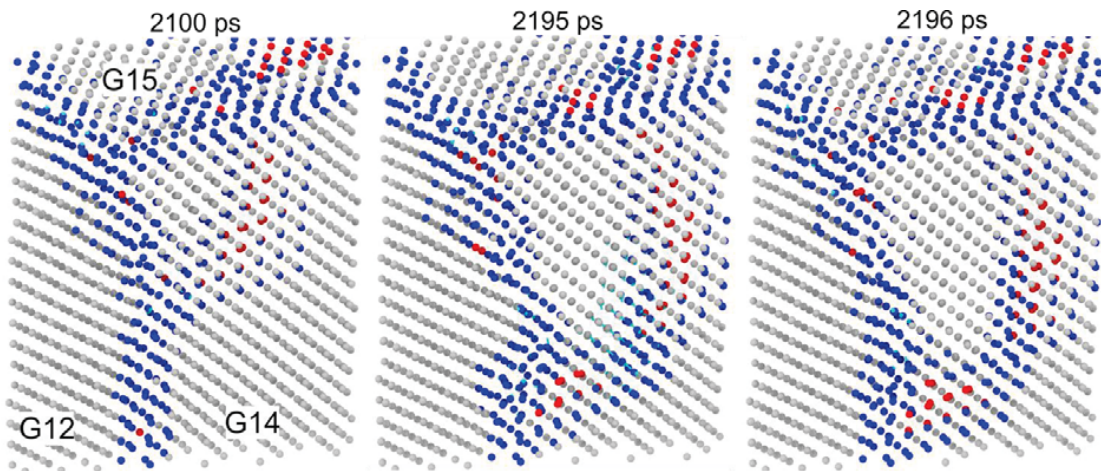


Figure 4-12 Local GB migration that occurs upon Dis2 nucleation and emission. The same region R2 as in Figure 4-7 is inspected.

4.3 Summary

The results of simulated stress reduction tests can be summarized as follows:

- The creep strain versus time curves after stress drops depend on the value of the stress drop, and

exhibit similar trends as those observed in *in situ* experiments: i.e. when the stress drop is mild, there is a continuous forward strain with creep time; as the stress drop becomes larger, an initial anelastic back flow dominates, after which the forward strain continues; for the largest stress drop no forward strain is observed within simulated creep time.

- As the magnitude of the stress drop increases, dislocation activity during creep is largely suppressed: for large enough stress drops, nucleated dislocations cannot further propagate. Only when they have already travelled a large distance across the grain, they seem to be able to further propagate.
- For a moderate stress drop, dislocations can still be emitted after a longer creep time even when strain rates considerably go down. Such dislocation events are associated with the prior occurrence of GB-mediated mechanisms such as GBD motion, GB sliding, GB migration, and atomic diffusion along GBs.
- With these reduced strain rates, it is observed that more than one dislocation can travel at the same time across the grain. The events studied here are Dis1 and Dis2 that have the same Burgers vector but opposite sign. They are separated by $2d_{111}$ and traveling on the (-111) slip plane. Dislocation-dislocation interaction is followed by a jog motion producing a vacancy inside the grain.

Overall, these first results assist the interpretation of the non-monotonic behaviour of the FWHM observed for *in situ* experiments: first decrease then increase. GB accommodation mechanisms are enhanced at the slower strain rates. Also, vacancy emission due to dislocation interactions within a grain was not observed in high strain rate MD simulations. Further understanding of this mechanism is beyond the scope of this thesis.

Chapter 5 Discussion

The main objective of this thesis is to understand the origin of the constant deformation resistance in NC metals and develop a better understanding on the interplay between multiple deformation mechanisms, in particular dislocation-based and GB-mediated processes. This goal is mainly achieved by stress reduction during *in situ* X-ray diffraction. MD simulations of the stress reduction tests provide further information on the deformation mechanisms at the atomic scale. In this chapter, Section 5.1 will discuss the results obtained for NC Ni batches. In Section 5.2 the effects of alloying and grain size will be discussed for the case of NC Ni₅₀Fe₅₀. Finally, Section 5.3 will discuss the results of MD simulations and compare them with what is known for MD simulations performed at higher strain rates.

5.1 Nanocrystalline Ni

In this section the results for NC Ni₃₅ batch will be first highlighted and discussed, after which the grain size effect will be addressed by comparing Ni₆₅ with Ni₃₅. Finally, some comments will be made on the activation volume as well as the athermal stress that are derived from transient testing.

5.1.1 Major observations

From the results reported in Section 3.1 and 3.2, the following important observations for NC Ni₃₅ can be highlighted:

The behaviour of the macroscopic strain and the FWHM as a function of the magnitude of the stress reduction reveals the presence of multiple transient regimes: in Figure 3-9 Regimes I-IV were identified when *in situ* conventional stress reduction tests were performed in tension. Figure 5-1 summarizes the major results including those in Figure 3-11. Figure 5-1a displays the evolution of the strain rate as a function of the inelastic strain and Figure 5-1b displays the interplay between the FWHM and the strain.

- Inspection of the strain evolution evidences a continuous forward flow for small/ moderate stress drops (Regimes I-II) and the dominance of an initial anelastic back strain for large stress drops (Regimes III-IV where $R < \sim 0.5$). The strain rate after the stress drop always decreases continuously towards the quasi-stationary value, showing an apparent “hardening”. This is verified even for a test followed by long-term creep in tension ($R = 0.70$ in Figure 5-1a) and stress reductions at larger strain in compression (Figure 3-16). In conventional pure CG materials, however, an increase of strain rate is usually observed after a certain creep period, so-called “transient softening” [115][120].
- In Regime I the FWHM immediately increases after the stress reduction, whereas in Regimes II-IV the peaks become narrower. For a moderate stress drop performed in Regime II, the FWHM does increase again after a while.
- Regime I corresponds to a high stress dependence of the strain rate at “constant structure”, whereas in Regimes II-III this dependence becomes lower and $\dot{\epsilon}_r/\dot{\epsilon}_0$ is logarithmically proportional to σ/σ_0 (see

Figure 3-13). This suggests that there exist two classes of mechanisms that dominate at different regimes and both contribute to the strain rate.

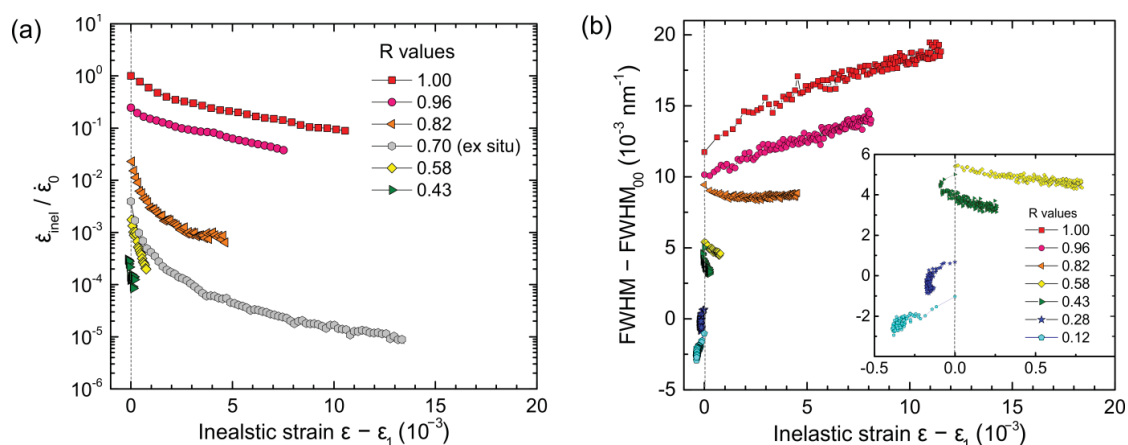


Figure 5-1 Transient behaviour of NC Ni₃₅ after the stress reductions: (a) the evolution of the strain rate as a function of the inelastic strain; (b) the corresponding change of the peak broadening. $FWHM_{00}$ refers to the initial broadening prior to loading. The inset represents a zoom-in.

The *in situ* multistep test shows consistency with the results obtained by conventional stress reduction tests: this is evidenced in terms of the evolution of the strain rate as well as the peak broadening (see Figure 3-21 and Figure 3-22).

- The microstructure “hardens” while approaching the quasi-stationary state. This is observed either by a continuous decrease of strain rate at a given stress step or by stepwise increasing stress while keeping similar low strain rates (see Figure 3-22a). The latter is viewed as an alternative way to approach the quasi-stationary state as illustrated in Figure 3-19.
- The behaviour of the FWHM has a different dependence on the applied stress. For low-stress steps the FWHM decreases during the 20 min creep periods; for higher-stress steps the FWHM increases with creep time (see Figure 3-22b and c).

The quasi-stationary flow stress is strain rate dependent; near a given quasi-stationary state the $\dot{\epsilon}$ - σ value is similar and independent of strain path: the former is evident in continuous deformation tests performed with different strain rates (Figure 3-4); the latter is derived by comparing the quasi-stationary $\dot{\epsilon}$ - σ value obtained from different types of tests (Figure 3-14a, Figure 3-22a, Figure 3-23a). Further discussion will be held in Section 5.1.2.

5.1.2 Deformation behaviour

It is well established that for NC metals with grain sizes in the range 10-100 nm, plastic deformation is governed by the interplay between dislocation-based and GB-mediated deformation mechanisms. In the present work, the above observations can be rationalized by such a model where both categories of deformation mechanisms are included and playing a role in producing inelastic strain. In general, under GB-mediated mechanisms one understands essential internal stress relaxation and defects recovery.

Four transient regimes

Within this model the behaviour of both macroscopic strain and diffraction peak broadening as a function of relative reduced stress R can be rationalized as the consequence of a competition between dislocation-based and GB accommodation mechanisms. Depending on the magnitude of the stress reduction, the ratio between these two categories changes resulting in the different regimes. Figure 5-2 is a schematic representation of this model that describes the presence of four transient regimes as shown in Figure 3-9.

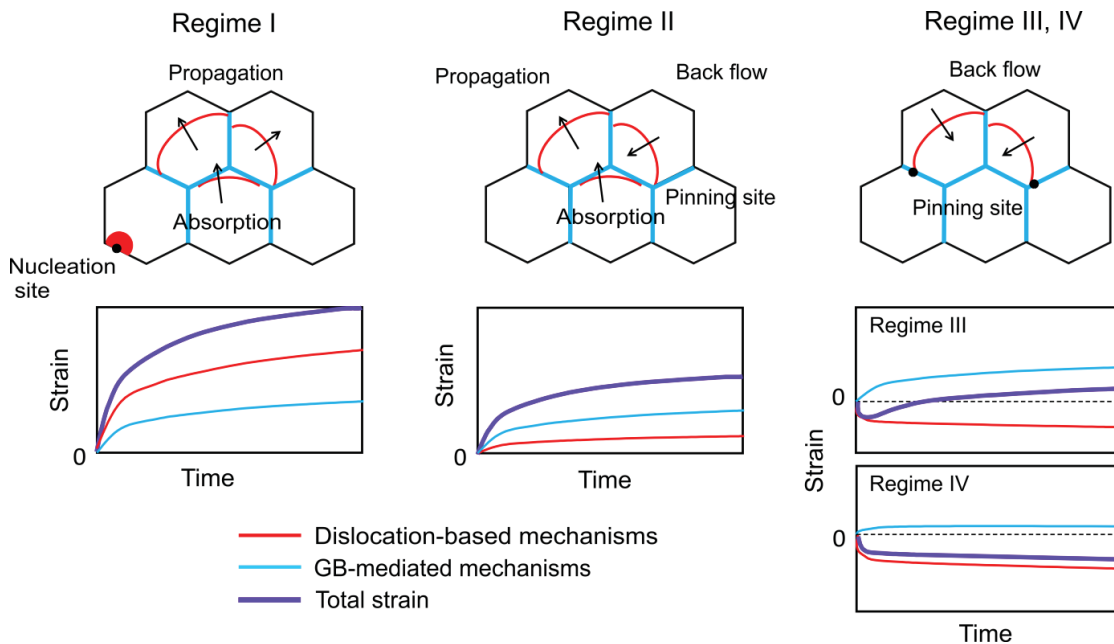


Figure 5-2 Schematic of the model describing forward and backward dislocation flow (red), and GB-mediated mechanisms (blue) for Regimes I-IV together with the corresponding evolution of strain contribution with creep time.

During plastic deformation with a constant strain rate up to a stress level of σ_0 , dislocations have been active. As a consequence, in some grains dislocations will be present within the grain interior, whereas in other grains dislocations might just have been nucleated or be close to absorption. Also, due to prior deformation, a development of high internal stresses of type II (intergranular) and III (intragranular) is expected. When a stress reduction is performed at σ_0 , the material responds differently depending on the magnitude of the stress drop:

- Regime I: when the stress is dropped slightly but still well above the internal stress, dislocations will further nucleate and propagate, however at a reduced rate. Overall dislocation activity will occur in smaller amounts because only those dislocations for which the applied stress is sufficient to overcome the local back stress can propagate. At the same time, dislocation slip requires GB accommodation processes [39][40][153] which also contribute to the plastic strain. However, as long as dislocation-based mechanisms still dominate over GB-mediated recovery, the diffraction peak broadening exhibits a net increase during the transient creep periods.

- Regime II: after the moderate stress reductions, the contribution of the dislocation activity is further suppressed so that GB-mediated mechanisms take over, thereby reducing the peak broadening. Note that the strain produced by dislocations slip is the net result of forward and backward flow. Figure 5-2 shows one of the cases where their net contribution is still positive but significantly reduced.
- Regimes III-IV: when the stress reduction is large enough, an initial negative strain is evidenced, which is ascribed to the dominance of back flow mainly from backward motion of dislocations. This process is relatively fast during which the internal back stresses drops quickly, thereby quickly reducing its contribution to backward flow. In contrast, GB-mediated recovery processes are relatively slow. They continue long after the stress reduction and generate forward flow that gradually declines with the progress of recovery. In the meantime, the internal stresses are relaxed.

Inspection of stress reduction tests in MD simulations evidences similar trends in creep strain versus time curves (Figure 4-2a): for small/ moderate stress drops, the forward strain is developed during creep; for large stress drops, however, an initial anelastic back strain dominates. Previous MD simulations [154][155][156] have shown the reverse dislocation motion upon unloading contributing to an anelastic back flow. In the present MD simulations, one observes that dislocation activity in terms of nucleation and slip events considerably decreases with increasing magnitude of the stress drop.

A quantitative analysis is shown in Figure 4-2b where the number of propagating dislocations in the same periods is reduced with decreasing R . At the smallest R of 0.53 and 0.33, small nucleation sites still exist but none of the dislocations are capable of propagating within current simulation time (1.7 ns). In one particular grain, however, a dislocation that had already propagated till the middle of the grain is observed to continue propagating after the stress reduction. This can be rationalized by a lack of local internal back stresses imposed by pinning sites, as for instance, GB ledges and impurities, etc. Also, in current MD simulations the mechanisms responsible for GB accommodation have been extensively explored after the stress reduction. It is observed that in addition to GB migration and GB sliding, other GB accommodation processes such as GB dislocation motion and active atomic diffusion along GBs are identified during the long-term creep.

Continuous decline of strain rates

After medium/ large stress drops performed on NC Ni, the strain rate associated with GB-mediated mechanisms was brought into foreground. It exhibits a continuous decline with plastic strain that results from GB structural relaxation (see Figure 5-1a). However, when similar magnitudes of stress drop (in terms of R value) were performed on pre-deformed pure CG polycrystals and single crystals [114][115][116][117][118][119][120], the strain rates versus plastic strain curves exhibit a different shape. This is exemplified in Figure 5-3 by the case study of CaF₂ [115] where subgrain structures (mainly low-angle boundaries) have been created in the grain interior during prior deformation.

In Figure 5-3a, it is evidenced that after a stress reduction of $R \leq 0.87$ the evolution of the strain rate is non-monotonic. This is interpreted by a model presented in Figure 5-3b where the strain rate is decomposed into two contributions: boundary migration and individual dislocation slip. Immediately after a medium/ large stress drop, the migration of subgrain boundaries produces most of the forward strain. At the same time, stress concentrations at the boundaries relax, resulting in two effects: (1) a decline of strain rate from boundary migration and (2) a resume of dislocation glide in subgrains. The latter occurs from the moment that local thermal stresses become positive again. After sufficient plastic strain is generated, the

slow coarsening of subgrains related with boundary migration gradually enhances stress concentrations at the boundaries as the pile-ups of free dislocations magnify. Eventually, both strain rates inside subgrains and strain rates due to boundary migration increase until a new quasi-stationary state (including the boundary spacing) is reached. Within this model, boundary migration leads to recovery of boundary area by boundary recombination. Such strains associated with recovery mechanisms seem to be a general phenomenon observed for single or CG materials. It occurs whenever a quasi-stationary state has been established at the point of stress reduction when crystal boundaries are present. This was confirmed by reduction tests on single crystal CaF_2 [115] and LiF [114]: the phenomenon becomes only prominent once subgrain structures have been generated.

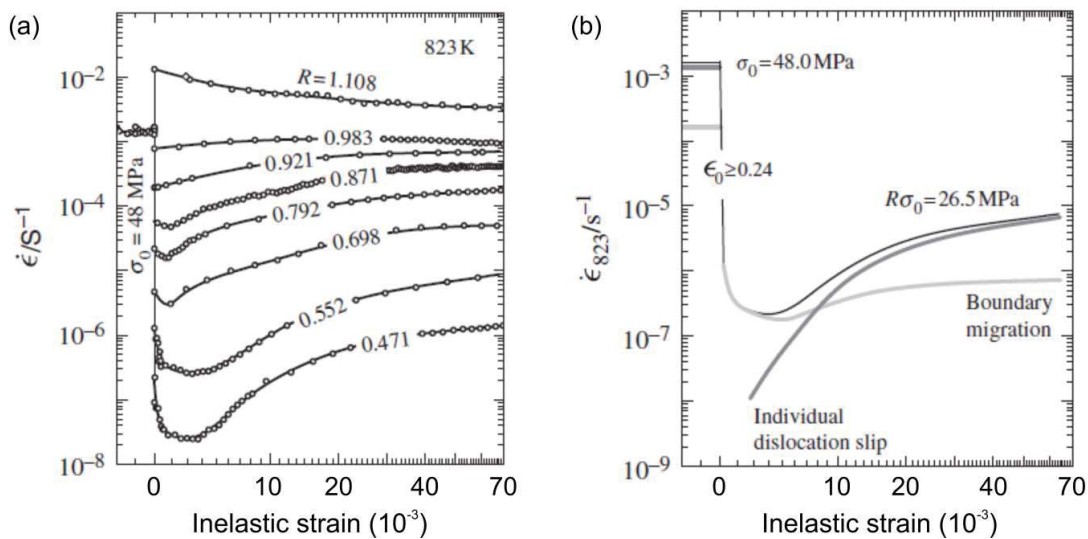


Figure 5-3 CaF_2 that contains subgrain with (mainly) low-angle boundaries after prior deformation: (a) after a medium/ large stress drop the inelastic strain rate during transient creep exhibits a non-monotonic change; (b) the total transient strain rate can be decomposed into contributions from two mechanisms [115].

Lack of an increase in strain rate, i.e. lack of transient softening, for NC Ni can be rationalized as follows: firstly, in contrast to those CG materials, subgrain structures with low-angle boundaries are virtually absent and not formed during plastic deformation of ED NC Ni where most of the GBs have a high-angle character. Secondly, the electrodeposition process produces several impurities that may decorate the GBs, making these structures relatively stable against grain growth [51]. With other words, the GBs in this material are expected to be less mobile. Finally, limited plastic strain ($< 2\%$) is generated in the creep regime, i.e. an amount that is probably insufficient to cause significant structure coarsening. In fact, in case significant grain coarsening would be present, an increase of plastic strain rate is expected, which was not observed here. However, it cannot be excluded that minor grain growth occurs as a consequence of GB accommodation mechanisms. In Section 3.4, the grain sizes during/ after continuous deformation were evaluated, demonstrating a minor increase ($< 2 \text{ nm}$) in tension and a modest increase ($\sim 10 \text{ nm}$) after large plastic deformation in compression. Inspection of MD simulations performed on NC Ni [40][157] suggests

that the GBs and TJs during deformation approach a more ordered structure and a more equilibrium geometry, which reduces plasticity or equivalently increases strength.

Non-monotonic change of FWHM

For intermediate stress drops in Regime II, the peak broadening exhibits a non-monotonic behaviour: after initial reduction the FWHM starts increasing again (see Figure 3-11). MD simulations suggest GB accommodation are present during deformation [14][40][158]. So similar to the case of CG materials, local forward dislocation motion may be re-activated.

To verify whether dislocations can still be emitted after the long-term creep, a medium stress reduction test ($R = 0.86$) followed by creep periods of 2290 ps was simulated by MD (see Section 4.2). As shown in Figure 4-4, several slip events were observed immediately after the stress reduction, followed by a period of mainly GB accommodation contributing to the strain. As creep progressed further, dislocation slip in the grain interior started again and can increase the FWHM. In one of the grains (G14 in Figure 4-5), two slip events were successively detected after creep periods of 1300 ps: (1) the first dislocation Dis1 was emitted from the precursor at $t = 1315$ ps, and soon afterwards it was pinned at the GB 12-14 for 700 ps before further propagation. (2) The second dislocation Dis2 was freshly nucleated at the GBs at $t = 2100$ ps; upon Dis2 emission it interacted with Dis1 and formed a jog in between. These two dislocations have the same Burgers vector but opposite sign, and travelled at the same time across the grain. At the beginning, they propagated fairly slowly because of another pinning site at the GB 15-14. Once they got unpinned, there was a significant increase in their travelling speed, which left a vacancy behind and gave rise to the strain burst in the strain-time curve. A detailed analysis of GB activity shows that the aforementioned dislocation events are associated with the prior occurrence of GBs structure adaption. Processes such as GBD motion, confinement of delocalized GBD core, GB sliding, GB/TJ migration, and other important atomic diffusion along the GBs were observed prior to dislocation emission. This is exemplified in Figure 5-4 by a case study of the configuration at $t = 1305$ ps (prior to Dis1 emission). Atoms in GBs are coloured according to CNA analysis in Figure 5-4a and shear strain analysis in Figure 5-4b. Besides, Figure 4-10 has shown that the full confinement of delocalized GBD core by forming a perfect GBD assists Dis1 unpinning at $t = 2085$ ps.

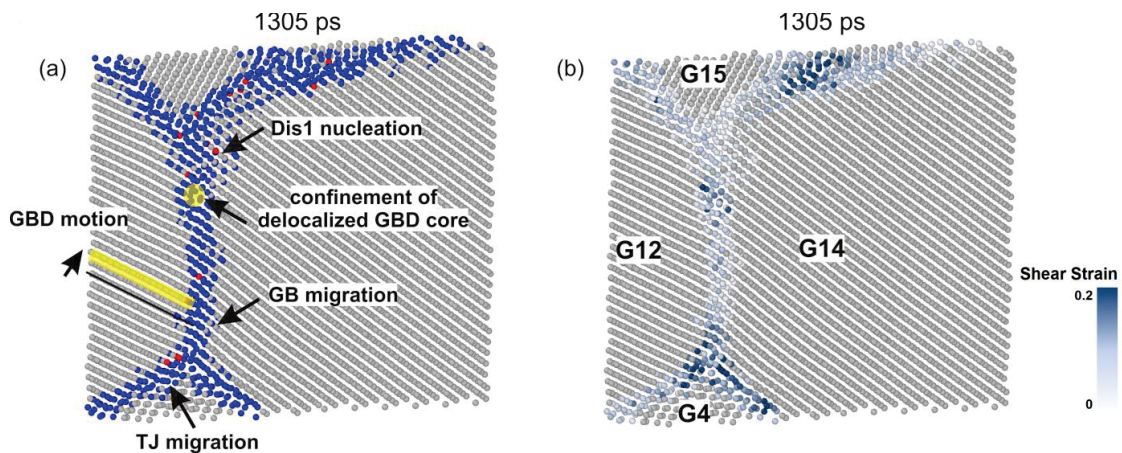


Figure 5-4 A configuration prior to Dis1 emission: atoms in GBs are coloured according to CNA in (a) and shear strain analysis in (b).

The role of GB accommodation

Before discussing the attainment of constant deformation resistance during uniaxial deformation, the role of GB accommodation in the work-hardening regime has to be mentioned. For NC materials, the onset of plastic deformation is rather heterogeneous [68] and only a fraction of grains will have deformed plastically. This can be rationalized by the fact that in a nano-sized grain the plastic strain produced by one dislocation per grain is large (of the order of $\sim b/d$, b : Burgers vector, d : grain diameter) [159]. In addition, because of the heterogeneous nature of NC materials some grains will have “easy” sources for dislocation nucleation whereas in other grains dislocation nucleation requires high stresses. As long as plastic events are scarce, dislocations can be accommodated by GBs and part of the internal stresses induced by electrodeposition process can be removed. This is evidenced by an extra reduction of the FWHM during the first unloads in load-unload experiments, i.e. a recovery of the RMS strain. Once a great majority of grains start deforming, the increased number of dislocations makes absorption by GBs more and more difficult. They may temporarily be stored at the GBs, thus increasing the local stress intensities. This view is supported by an increase in the FWHM upon unloading from the region nearby maximum flow stress in tension and from the plateau regime in compression; both point towards an increased RMS strain.

Quasi-stationary state

In NC materials, due to the extremely small mean free dislocation paths limited by the boundaries of nano-sized grains, the rate of defect generation inside grains and at boundaries must be very high. The correlation between the dislocation generation rate and the grain size can be derived from the following picture: assuming that dislocations are circular loops that expand under an applied stress and are deposited as extrinsic dislocations at the boundaries, then the rate of dislocation generation $\dot{\rho}^+$ is given by [160]:

$$\dot{\rho}^+ = \frac{2M}{br} \dot{\epsilon} = \frac{1}{b\Lambda} \dot{\epsilon} \quad (5-1)$$

with M the Taylor factor, b the Burgers vector, r the grain radius, $\Lambda = r/2$ the dislocation mean free path, and $\dot{\epsilon}$ the strain rate. With other words, there exists an inverse correlation between $\dot{\rho}^+$ and r .

The high resulting defect density (point defects, dislocations, grain boundaries and their reaction products) provides a high driving force for dynamic recovery. Once all grains have deformed, it is expected that GBs will receive dislocations with respective Burgers vector \mathbf{b}_1 and \mathbf{b}_2 to be absorbed from both sides. This is visualized in Figure 5-5. They can react with each other by GB accommodation processes, leading to GBD recombination/annihilation. Such processes are accelerated as dislocation storage at GBs is enhanced; eventually a certain limit of dislocation density in the structure will be reached. The role of GB diffusion in facilitating dislocations annihilation by climb has been discussed in Refs. [160][161], which is more efficient compared to annihilation processes in conventional CG materials.

Overall, one can expect that in NC materials a quasi-stationary state where some (but not necessary all) structure parameters have saturated will be attained in a relatively small strain interval ($< 4\%$). This quasi-stationary state is reflected in a constant flow stress, where dislocation-based and GB accommodation processes reach a dynamic equilibrium. In other words, the rate of dislocation generation is compensated by the rate of recovery, resulting in no net change of dislocation density. This view is consistent with *in situ* results, where the FWHM becomes saturated in the plateau regime, indicating that the upper limit of defect density in the structure is attained for the current deformation condition. For CG materials, e.g. CG

Ni, the observation of plateau regime is delayed, i.e. a mild work-hardening regime over a larger strain range > 20 % is observed [162][163].

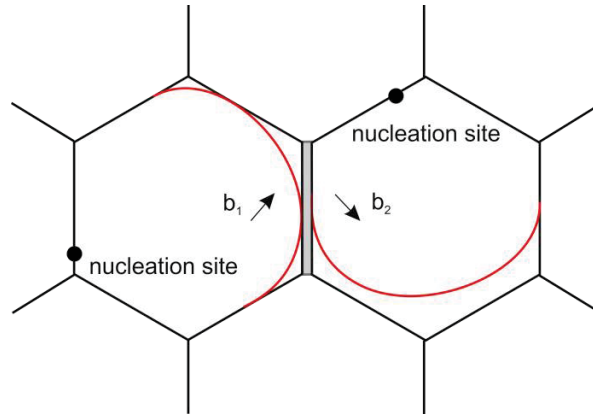


Figure 5-5 Once all grains have deformed, it is expected that GBs will receive dislocations with respective Burgers vector b_1 and b_2 to be absorbed from both sides.

Based on the discussion above, the different behaviours of the peak broadening observed for *in situ* stress reductions in tension and compression can be rationalized as follows: in compression mode stress reductions were performed at a well-defined quasi-stationary state where there is no work-hardening. Any magnitude of the stress drop will lead to a net recovery of defects, bringing the current structure to a new quasi-stationary state that corresponds to a lower stress level. Therefore, a decline of the FWHM during transient creep is always observed irrespective of R . In contrast, stress reductions in tension were performed at a stress level prior to the maximum flow stress. The transient behaviour is a superimposition of a continuous work-hardening and GB-mediated recovery. Depending on the quasi-stationary value of the FWHM at the reduced stress, the current FWHM value may either increase or decrease with further plastic strain.

Also, it is known that both deformation modes can attain a constant flow stress; however, one obtains very limited plastic strain in tension when compared to compression. The consequence of a lack of further straining hardening during tensile deformation is the early onset of necking as described by the Considère criterion. In Ref. [28], K.S. Kumar *et al.* studied the damage evolution on ED NC Ni (~ 30 nm) using *in situ* TEM, showing that the nucleation and growth of voids at GBs/TJs play a role in leading fracture. A similar observation on UFG Al thin films was obtained by F. Mompou *et al.* [164]. In general, such voids are created when there is a lack of accommodation of the plastic deformation mechanisms. In compression mode, the formation of nanovoids can be suppressed. Also, as suggested by MD simulations [165], once nano-cracks are formed, they tend to be aligned parallel to the compression direction such that the propagation along GBs is inhibited. Therefore, one can expect that other mechanisms will be initiated to continue the deformation. In Figure 3-3, a slight decrease in flow stress is observed when further straining in compression (> 15 % strain), which hints for a modest grain coarsening as was measured by post-mortem TEM (Section 3.4.2). This result shows the consistency with those in literature; grain coarsening in

NC Ni was only reported when undergoing very high deformation level, such as compression [91], high pressure torsion (HPT) [58][166], and rolling [167][168].

Strain rate dependence of quasi-stationary flow stress

Figure 3-4 shows the strain rate dependence of quasi-stationary flow stress during continuous deformation. This can be rationalized by the time dependence of the accommodation processes. Electrodeposited NC Ni is well-known to have non-equilibrium GBs. When deformation is performed at lower strain rates, there is more time to relax these GBs to lower energy configurations meanwhile also contributing to the emission and absorption of dislocations. As suggested by the current MD simulations, more GB accommodation especially those strongly thermal activated processes, e.g. GBD motion and active atomic diffusion, are observed at lower strain rates. In contrast, when the deformation rate is higher, a certain amount of strain needs to be produced within shorter time periods. This means that in the transition from micro to macro plasticity more grains will have to contribute to plasticity by dislocation events. Thus, the flow stress is raised by an increased number of dislocations to be generated. A consistent picture is provided by a clear difference in fracture surface topography resulting from low (3×10^{-4} /s) and high (3×10^{-1} /s) strain rate testing as reported in Ref. [163].

Strain path independence of quasi-stationary state

For NC Ni₃₅, it is found that the $\dot{\epsilon}$ - σ value near a given quasi-stationary state is very similar when the results from different types of experiments are compared, as shown below:

- Continuous deformation vs. stress reduction test: the stress-strain curve of a continuous deformation test is similar to that of a stress reduction test in which the reloading is performed at the same rate (see Figure 3-14).
- Continuous deformation vs. multistep test: the constant flow stress σ reached in a continuous deformation test with a low strain rate $\dot{\epsilon}$ (pink curve in Figure 3-22a) is similar to the $\dot{\epsilon}$ - σ relationship reached in a multistep test (green dot in Figure 3-22a)
- Stress reduction vs. multistep test: for a given stress level σ , the $\dot{\epsilon}$ -FWHM value at the end of creep periods is similar for a conventional stress reduction test and a multistep test. Two different stress levels are compared in Table 5-1.

The above observations suggest that the quasi-stationary state is strain path independent, i.e. the establishment of a characteristic balance between dislocation generation and recovery by GB accommodation under the current deformation conditions is independent of prior deformation path.

Table 5-1 Comparison of the strain rate and the FWHM at the end of creep periods for a given stress in conventional stress reduction tests and a multistep test.

Stress reduction tests	σ (GPa)	Strain rate (/s)	FWHM (10^3 /nm)	Creep time (min)
Conventional stress reduction	1.64	6.9×10^{-7}	8.85	60
	1.18	1.8×10^{-7}	3.50	60
Multistep	1.66	7.2×10^{-7}	8.91	20
	1.17	1.5×10^{-7}	3.57	20

5.1.3 Grain size effects

The above highlighted results were reviewed for NC Ni₆₅. Overall one can say that the transient behaviours of Ni₆₅ and Ni₃₅ are very similar as well as their signatures in the diffraction pattern. After a medium/large stress drop, it is found that the forward strain rate associated with GB-mediated mechanisms is lower in Ni₆₅ but the dependence on the stress drop is not very different from that of Ni₃₅: the slope of the logarithmic normalized reduced strain rates $\dot{\epsilon}_r/\dot{\epsilon}_0$ versus R amounts 4.6 for Ni₃₅ and 5.0 for Ni₆₅, see Figure 3-13.

To further explore the influence of grain size on GB-mediated mechanisms, their relative contribution to the overall strain rate at the point of stress reduction, i.e. a state closer to quasi-stationary, is estimated. This is illustrated in Figure 5-6, which shows a zoom-in of the high- R region of Figure 3-13 (for NC Ni batches) as well as Figure 3-26 (for NC Ni₅₀Fe₅₀). The relative contribution can be obtained by extrapolating the linear slope $\dot{\epsilon}_r/\dot{\epsilon}_0$ fitted to the large and medium stress drops to $R = 1$, as indicated by the cross symbol. It is found that 24% of the strain rate in Ni₃₅ comes from GB-mediated mechanisms whereas only 12% in Ni₆₅. This can be expected since the volume fraction of GBs/TJs increases with decreasing grain size, which means the overall GBs/TJs activity plays an increasing role in plastic deformation. On the other hand, assuming that the generated plastic strain prior to stress reduction is predominantly due to dislocations, a larger number of dislocations are needed in Ni₃₅. Whether this would change the relative amount of the strain rate between dislocation slip and recovery component is difficult to say. One should not forget that the character of the GBs can be different which can influence the type of accommodation involved as well as the amount required. Also, since NC Ni₆₅ exhibits a stronger (100) out-of-plane texture than that of NC Ni₃₅, the influence of texture cannot be excluded.

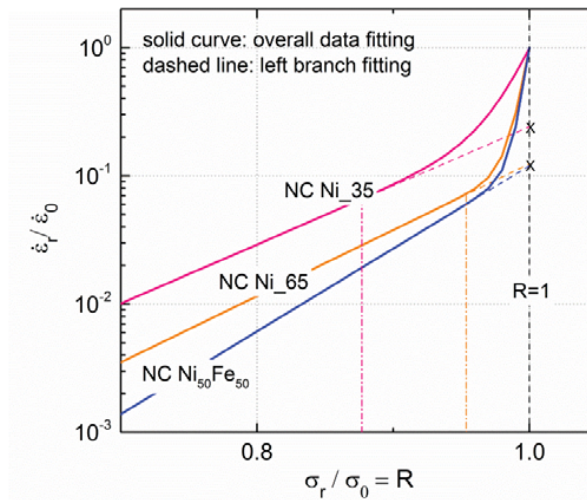


Figure 5-6 A zoom-in of the high- R region of Figure 3-13 as well as Figure 3-26. The relative contribution of the GB-mediated processes to the overall strain rate at the point of stress reduction can be obtained by extrapolating the linear slope $\dot{\epsilon}_r/\dot{\epsilon}_0$ fitted to the large and medium stress drops to $R = 1$, as indicated by the cross symbol.

Finally, it is interesting to note that in Ni₅₀Fe₅₀ with the smallest grain size, only 12 % of the strain rate would come from accommodation mechanisms at $R = 1$, suggesting that GB character and alloying play an important role besides the grain size. Further discussion on Ni₅₀Fe₅₀ will be held in Section 5.2.

5.1.4 Activation volume and athermal stress

As has been shown above, both dislocation glide and GB accommodation processes contribute to the plastic strain. As a consequence, the activation volume derived traditionally from the basic assumption of only thermally activated dislocation glide should be taken with caution. Nevertheless, one may estimate an “apparent” activation volume V of thermally activated dislocation motion by rewriting equation (1-2) as

$$V = \sqrt{3}k_B T \left(\frac{\partial \ln \dot{\epsilon}_r}{\partial \sigma_r} \right)_{\sigma_r = \sigma_0} \quad (5-2)$$

Here $\dot{\epsilon}_r$ is the experimentally measured reduced strain rate. By taking the derivative of the $\ln \dot{\epsilon}_r - \sigma_r$ curve at $\sigma_r = \sigma_0$, i.e. $R = 1$, $V = 9b^3$ and $32b^3$ for NC Ni₃₅ and NC Ni₆₅ are obtained, respectively. Also, according to equation (1-3), the strain rate sensitivity m is determined as $m = 0.028$ and 0.015 , respectively. These values are very similar to those reported in Refs. [102][103][104][105][169][170]. Compared with CG Ni the enhanced strain rate sensitivity in NC Ni may be in part influenced by the presence of GB-mediated processes. Lower strain rates offer more time to produce positive strain via GB accommodation mechanisms; strongly thermal activated processes, such as dislocation climb at GBs may play an important role [104][160].

In Ref. [112] the magnitude of the athermal stress for NC Ni from Goodfellow was estimated from conventional *ex situ* stress reduction tests. The athermal stress is assumed to equal the applied stress when the initial creep rate measured from first 10 s after a stress drop becomes zero [101][110][111][112]. However, the *in situ* tests presented in this work suggest that GB-mediated plasticity may also contribute significantly to the strain rate. As a consequence, the values of the athermal stress are presumably underestimated. A potential other criterion to find the athermal stress is to take the value of the applied stress when the $\dot{\epsilon}_r - \sigma_r$ curve in Figure 5-6 starts deviating from the linearity, as illustrated by the pink and orange dash dot lines. This method assumes that the thermal stress on dislocation glide is zero for a stress reduction after which the component of the strain rate from dislocations becomes zero instead of the overall rate. For NC Ni batches investigated in this thesis, the athermal stress would be about 80 % of the σ_0 for NC Ni₃₅ and 90 % for NC Ni₆₅. In contrast, ~ 50 % of the σ_0 are measured for both when deriving the athermal stress from the $\sigma_0 - \Delta\sigma$ value with $\Delta\sigma$ corresponding to a threshold magnitude that results in a zero initial creep rate, as was done in Ref. [112].

5.2 Nanocrystalline Ni₅₀Fe₅₀ versus Ni

5.2.1 Major observations

From what has been reported in Section 3.3, this section compares the highlights of results for NC Ni₅₀Fe₅₀ with those for NC Ni (Section 5.1.1). The FWHM of {200} peak is mainly used for Ni₅₀Fe₅₀ owing to its qualitatively similar behaviour as the {311} peak but a higher signal-to-noise ratio.

NC Ni₅₀Fe₅₀ exhibits three regimes, as compared to four regimes for NC Ni: only Regimes II-IV similar to NC Ni are observed, see Figure 3-24. Regime I where both macroscopic strain and FWHM increase during creep periods is missing.

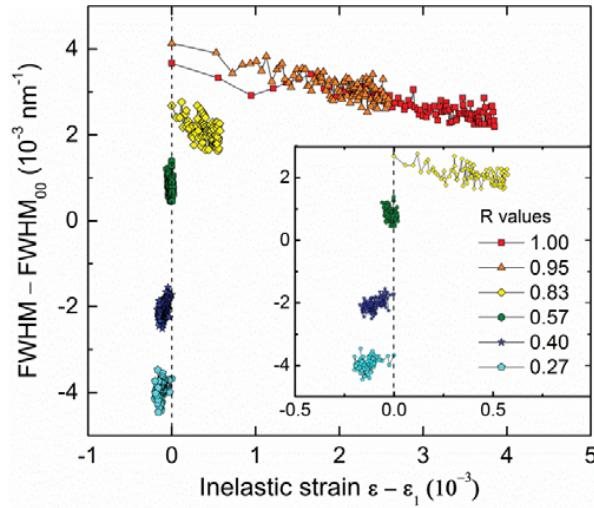


Figure 5-7 The interplay between the FWHM of {200} diffraction peak and the inelastic strain in NC Ni₅₀Fe₅₀

- Inspection of the behaviour of the strain reveals some similarities: one observes anelastic back strain for large stress drops and a continuous decline of strain rate irrespective of R . Also, the strain rate can be decomposed into two contributions with respective high and low stress sensitivity, see Figure 3-26.
- Inspection of the behaviour of the FWHM evidences some differences: there is a lack of FWHM increase even for a small stress reduction. This is visualized in Figure 5-7 where the interplay between the FWHM and the inelastic strain is displayed for the case of $\sigma_0 = 1.7$ GPa. In addition, when σ_0 reaches 1.9 GPa, one observes a peak family dependent FWHM evolution only while keeping stress constant ($R = 1$) (see Figure 3-25). It is noted that the FWHM of {311} diffraction peak that is mostly affected by the presence of dislocation hardly decreases.

The *in situ* multistep test exhibits a similar transient hardening but a lack of FWHM increase when creeping at high stress levels.

- The hardening effect during transients is evident from the $\dot{\epsilon}$ - σ evolution: one observes a continuous decrease of $\dot{\epsilon}$ at a constant σ as well as an overall increase of σ at similar $\dot{\epsilon}$ (see Figure 3-28). However, inspection of the plastic strain generated per step shows very limited amounts when compared to those of NC Ni.
- The evolution of the FWHM during creep periods depends on the applied stress: immediately after a stress reduction, the FWHM decreases during the initial low-stress creep; upon further increasing stress, the FWHM almost remains unchanged; no evident increase is observed even during high-stress creep. This is consistent with the results reported in conventional stress reduction tests.

The presence of the reloading yield point, the magnitude of which depends on the strain reached prior to the reloading: this result is in good agreement with the yield point phenomenon reported in Ref. [121] in

which samples from the very same batch were investigated. This phenomenon occurs whenever there is a change of strain rate. Figure 3-27 demonstrates that the relative peak height increases with more plastic strain generated prior to the reloading.

5.2.2 Deformation behaviour

For NC $\text{Ni}_{50}\text{Fe}_{50}$, the deformation model proposed in Section 5.1.2 that both dislocation-based and GB-mediated mechanisms play a role in generating plastic strain can be utilized to rationalize the similarities in the transient behaviours. However, one should keep in mind that both alloying and grain size can have influences when compared to NC Ni. The following discussions will focus on the interpretation of those peculiar behaviours observed for NC $\text{Ni}_{50}\text{Fe}_{50}$.

The behaviour of FWHM

From what has been reported for *in situ* conventional stress reduction tests in tension (Figure 3-9, Figure 3-12, Figure 3-24), Figure 5-8 summarizes the total change of the FWHM versus the total change of the inelastic strain during the creep periods of 30 min for NC Ni₃₅, Ni₆₅, and $\text{Ni}_{50}\text{Fe}_{50}$. The data points framed in the black squares represent the values measured at a relative reduced stress $R = 1$. For NC Ni one observes the expected behaviour: as the magnitude of the stress reduction increases (decreasing R), less plastic strain is produced and the peak broadening decreases accordingly. For R values below ~ 0.5 the FWHM decreases during the creep periods because the forward dislocation glide is largely suppressed and GB-mediated mechanisms prevail. For $\text{Ni}_{50}\text{Fe}_{50}$, however, the opposite trend is observed: the largest reduction of the peak broadening is observed at $R = 1$, which reduces with decreasing values of R . With other words, more plastic strain goes hand in hand with more reduction of the peak broadening.

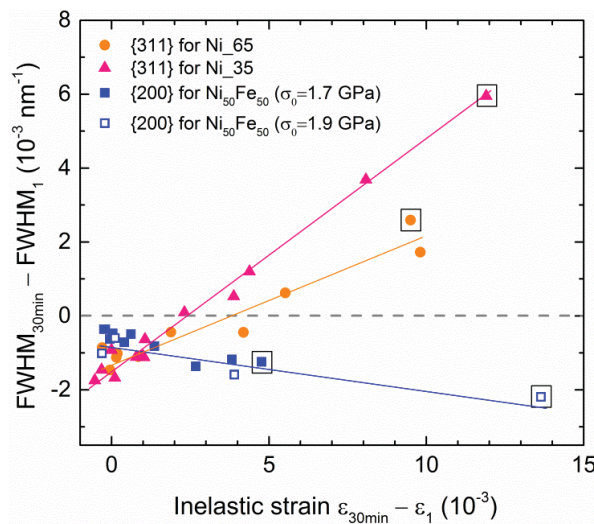


Figure 5-8 The total change of the peak broadening versus the total change of the inelastic strain generated during the creep periods of 30 min: FWHM_1 and ϵ_1 refer to the values at the start of the creep; FWHM_{30min} and ϵ_{30min} refer to the values measured at the end of the creep. The data points framed in the black squares were measured at a relative reduced stress $R = 1$. R decreases along the straight lines from the right side of plot to the left.

There are several possible reasons for the observed differences between NC Ni and Ni₅₀Fe₅₀. The most obvious one is related to the effect of solutes. It was shown that in this batch of NC Ni₅₀Fe₅₀ the Fe atoms are in solute solution in the FCC Ni matrix, however with local compositional fluctuations at the GBs and in the grain interiors [122]. Solute atoms are known to affect dislocation mobility [171]. The addition of Fe to the Ni matrix leads to a large reduction of the shear modulus, which in turn results in a softening effect [73][113]. As a consequence, the strength of this Ni₅₀Fe₅₀ batch is similar to that of NC Ni₃₅, despite its smaller grain size and the presence of solutes. On the other hand, solutes may induce strain aging effects, i.e. solutes diffuse to mobile dislocations that are (temporarily) pinned, leading to an increase of the required stress to unpin them. The presence of an upper/ lower yield point upon reloading or changing the strain rate is an indication of such strain aging effects [113]. The stress reduction tests performed in this work further strengthen this hypothesis. Figure 5-9 shows for both NC Ni₃₅ and Ni₅₀Fe₅₀ the evolution of strain rate as a function of inelastic strain generated during creep after stress reductions with $R = 1$ and $R = 0.9$. Three remarkable differences can be noticed: (1) the slopes for Ni₅₀Fe₅₀ are much steeper compared to Ni, (2) for Ni₅₀Fe₅₀ the initial strain rate at $R = 0.9$ is very much reduced compared to $R = 1$ (nearly two orders of magnitude), which is much less pronounced for the case of Ni, (3) at $R = 0.9$ the slope for Ni₅₀Fe₅₀ is significantly steeper compared to $R = 1$, which is also much less pronounced for the case of Ni. All these observations point towards a mechanism in NC Ni₅₀Fe₅₀ where dislocation glide is suppressed effectively when changing from constant strain rate to constant stress (even at $R = 1$). This may also explain the opposite trend observed for Ni₅₀Fe₅₀ in Figure 5-8: since dislocations are pinned by solutes the main contribution to the change in FWHM arises from recovery which decreases with decreasing R .

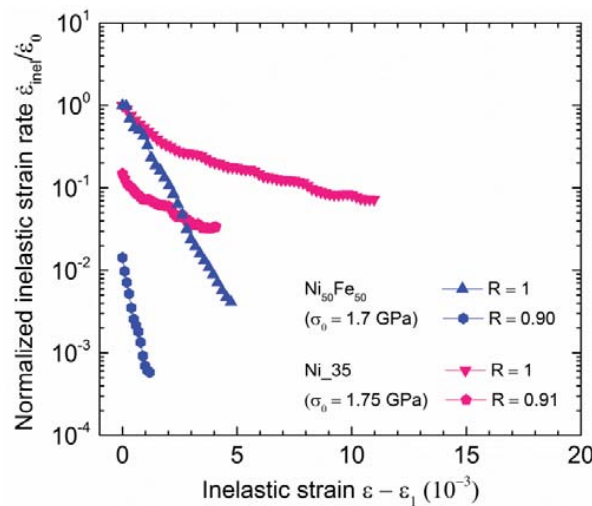


Figure 5-9 The evolution of normalized inelastic strain rate $\dot{\epsilon}_{inel}/\dot{\epsilon}_0$ as a function of inelastic strain generated during creep after stress reductions with $R = 1$ and $R = 0.9$: Ni₃₅ and Ni₅₀Fe₅₀ are respectively denoted as pink and blue symbols.

Other arguments can be used to explain the different behaviour in Figure 5-8. NC Ni-Fe is known to exhibit grain growth during plastic deformation [53][134][136][172][173][174]. Therefore, the reduction of the FWHM during creep after stress reduction may be interpreted as an indication for grain growth. The

reduction of the FWHM at $R = 1$ ($\sim 2 \times 10^3 \text{ nm}^{-1}$) would correspond to an increase of the average grain size by $\sim 7\%$ (1 nm) in the direction perpendicular to the loading axis. With decreasing values of R grain growth is reduced, leading to a lower decrease of the FWHM. Such a large grain growth is however unlikely, as only 0.5 % strain is produced during creep at $R = 1$ ($\sigma_0 = 1.7 \text{ GPa}$).

Moreover, for the case of $\text{Ni}_{50}\text{Fe}_{50}$ the effect of stacking fault energy (SFE) also needs to be considered. It is known that the addition of soluble alloying elements in FCC metals decreases the SFE [175]. In the case of Ni-Fe alloys, the SFE decreases approximately linearly with the addition of Fe to the Ni matrix [176][177]. As a result, the low SFE facilitates the emission of partial dislocations over full dislocations. Furthermore, Ni-Fe is known to exhibit a high density of growth twins [113][134][135][172][178]. Under certain conditions a reduction of such growth twins has been observed. For instance, L. Li *et al.* [179] found a reduction of twin density after cold rolling of Ni-18wt%Fe, S. Cheng *et al.* [135][172] report on a similar observation for Ni-20wt%Fe after substantial deformation under dynamic loading and after the cyclic deformation with overall plastic strain $< 2\%$, and so does work of S. Ni *et al.* where Ni-20wt%Fe was under severe plastic deformation. Therefore, the inverse trend for the FWHM observed in Figure 5-8 for $\text{Ni}_{50}\text{Fe}_{50}$ may also be attributed to detwinning, which would result in an increase of the X-ray coherent scattering length and, consequently, a decrease in peak broadening. With decreasing values of R the detwinning mechanism is effectively reduced.

The multistep tests experiments on Ni (Figure 3-22) and $\text{Ni}_{50}\text{Fe}_{50}$ (Figure 3-28) reveal a clear dependence of the FWHM on the applied stress; each load step leads to an immediate change in FWHM. For Ni the FWHM decreases at low stress levels during the creep period that follows each step, showing that GB accommodation is still the most important contributor. At higher stress levels the FWHM increases during the 20 min creep periods, indicative for dislocation slip. This is in good agreement with the result of the regular stress reduction tests. For $\text{Ni}_{50}\text{Fe}_{50}$ the FWHM remains constant during the creep period at low stress levels (except for the first creep periods after the stress reduction) and even slightly decreases at higher stress levels. This indicates that the deformation mechanism responsible for the reduction of the FWHM (recovery, de-twinning/ grain growth) is active at high stress levels.

Question remains why for $\text{Ni}_{50}\text{Fe}_{50}$ the FWHM only increases upon each increase of the applied load and not during the creep period. The *in situ* tensile experiments on $\text{Ni}_{50}\text{Fe}_{50}$ [113] have revealed that during regular monotonic loading the FWHM hardly increases and that after unloading the FWHM is strongly reduced compared to the initial state. These results together with those reported in this thesis indicate that for $\text{Ni}_{50}\text{Fe}_{50}$ dislocation-based plasticity is easily suppressed and that GB accommodation processes are very active. The increase of the FWHM as a function of applied stress may therefore be mainly related to an increase of the width of the distribution of intergranular strains within a grain family, rather than by an increase in dislocation density.

Prior strain dependence of reloading yield point

When reloading yield point is attributed to a strain aging effect, the strain dependence of the peak height can be explained by different models. The early models following A. Cottrell [180] considered a vacancy mechanism, suggesting that the growing peak height with strain is related to an increase of diffusivity of solute atoms when excess vacancies are generated during plastic deformation. Later on L.P. Kubin *et al.* [181] [182][183] proposed a dislocation model, suggesting that such strain dependence is governed by an increase of mobile dislocation density with strain. Inspection of stress reduction tests performed at $R = 1$

for $\sigma_0 = 1.9$ GPa and $\sigma_0 = 1.7$ GPa indicates the latter model for the interpretation of differences in the behaviour of strain and FWHM. As can be seen in Figure 5-8, on the one hand, the plastic strain generated within same creep period is 2.8 times larger in the case of $\sigma_0 = 1.9$ GPa. On the other hand, the {311} diffraction peak that is most affected by the presence of dislocations almost remains constant while creeping at $\sigma_0 = 1.9$ GPa (see Figure 3-25) but exhibits a visible reduction in the case of $\sigma_0 = 1.7$ GPa. This may explain why a peak family dependent FWHM evolution is only visible when stress is kept constant ($R = 1$) at higher σ_0 .

Invalidity of “constant structure”

The stress dependence of strain rate in Figure 3-26 is validated under the assumption of “constant structure”. However, when strain aging is present the conditions of constant structure may have been strongly violated because the solute concentration in relation to the mobile dislocation density is strain rate dependent. With other words, the solute concentration around dislocations increases with decreasing mobile dislocation velocity, thus resulting in an increase of thermal stress σ_{sol}^* for thermally activated overcoming of solutes drag. This questions the validity of using Figure 3-26 in estimating the activation volume, athermal stress, and the relative contribution of GB-mediated mechanisms to the overall strain rate.

Quasi-stationary state for NC Ni₅₀Fe₅₀

Assuming the maximum flow stresses reached during uniaxial tensile deformation of NC Ni₅₀Fe₅₀ is indicative of quasi-stationary state, Ref. [113] demonstrated that this quasi-stationary flow stress hardly depends on the strain rate, see Figure 5-10.

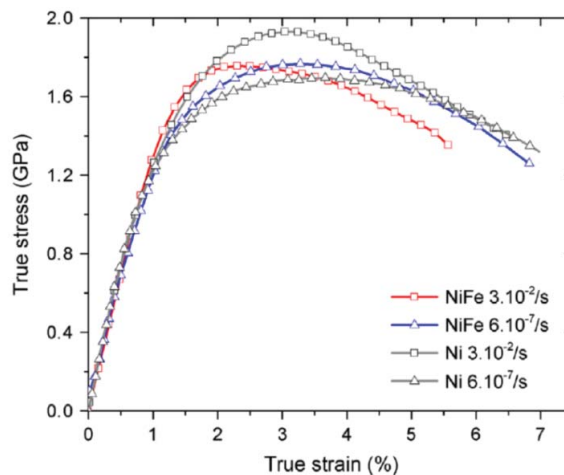


Figure 5-10 Stress-strain curves of continuous deformation tests at different strain rates for NC Ni and NC NiFe [113].

In this work, the same batch Ni₅₀Fe₅₀ was investigated. This behaviour can be rationalized by a strain aging effect by which the σ_{sol}^* component is enhanced at lower deformation rates. In Figure 5-10, however, one observes that the Ni₅₀Fe₅₀ specimen deformed at a high strain rate (red curve) exhibits a pronounced earlier

onset of necking than that performed at a low rate. Whether the measured maximum flow stress would have increased further without necking or it indeed represents the quasi-stationary flow stress is unknown. To make this point clear, continuous compression tests need to be done in the future.

5.3 MD simulation at lower strain rates

Stress reductions followed by creep were simulated by MD simulations to verify whether dislocations can still be emitted and propagate after a long-term creep period. In Section 5.1, it has been discussed that even after creep periods up to 1300 ps, dislocation events may still occur. It is observed that more than one dislocation is emitted in succession with a time interval of ~ 800 ps, after which they interact with each other and travel simultaneously across the grain. Figure 5-11 summarizes these relevant events in relation to the creep strain versus time curve. It has been noticed that after the stress drop the strain rates are considerably reduced by two orders of magnitudes to 10^6 /s. At such lower rates, the occurrence of dislocation events is associated with a variety of GB-mediated mechanisms involved in changing GB structures. Mechanisms such as GB sliding, GB/ TJ migration, GBD motion, confinement of GBD core, and other active atomic diffusion along the GBs are observed. As a consequence, dislocation nucleation is re-activated.

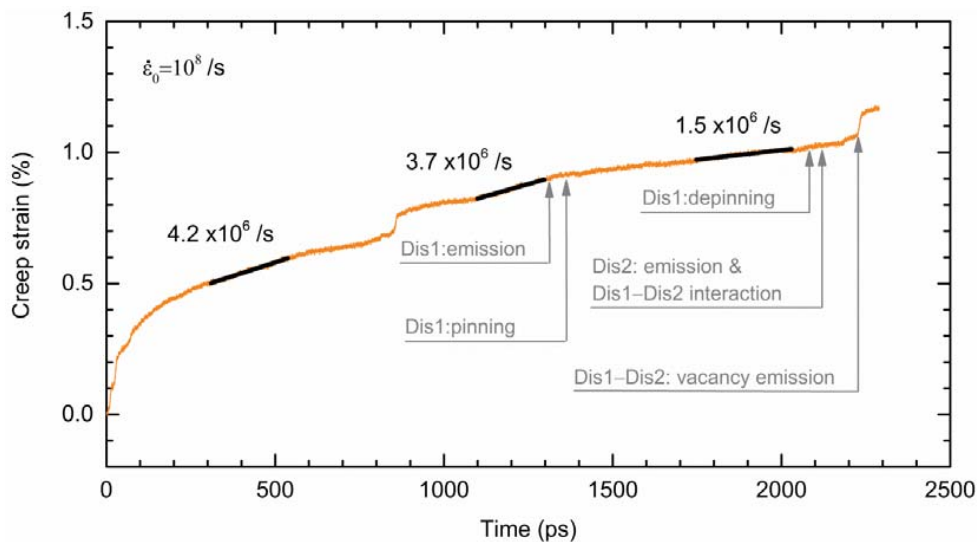


Figure 5-11 Creep strain versus time curve for one test with a stress reduction of $R = 0.86$ followed by creep periods of 2290 ps.

Another important finding of these MD simulations is that it provides an approach to reveal the mechanisms that are not seen in atomistic simulations with higher strain rate. In general, MD simulations are carried out at much higher strain rates (usually $> 10^7$ /s) and much shorter deformation times (usually < 0.5 ns) than those experimentally performed. Under such conditions GB accommodation is very limited where time-dependent processes are seriously suppressed. To overcome these restrictions, V. Yamakov et

al. [48] performed MD simulations on NC Pd at elevated temperature where distinct GB diffusion creep can be identified. However, experimental works [184][185] done on NC metals suggest that diffusion-based mechanisms at the GBs can become active at/ near room temperature as their volume fraction of GBs/ TJ increases with decreasing grain size. The present MD simulations performed at lower strain rates and with longer simulation times provide a consistent picture (in spite that the simulation time is still very short compared to experiment): atomic diffusion along the GBs is frequently observed and involved in different accommodation processes.

Finally, toward a further understanding of strain rate related deformation mechanisms, the results of continuous deformation with and without stress reduction are compared when the same amount of plastic strain is generated. Table 5-2 compares the number of slip events and deformation time in both cases. It is found that when the deformation continues without stress drop (10^8 /s), more slip events are observed within much shorter deformation time. This would indicate that at higher strain rates the relative contribution of dislocation slip to the overall strain is larger than that at lower rates. Further confirmation needs a quantitatively analysis to obtain this proportion. The differences between these two deformation modes are also addressed by comparing the structure of particular GB (GB 12-14) as studied before (see Section 4.2). This is visualized in Figure 5-12 where their respective configurations after producing the same amount of strain are displayed. The atomic displacement vectors (light blue) represent the difference between the current configuration 110 ps or 2290 ps relative to the configuration at the stress reduction. The important observations at higher rates/ shorter deformation time can be highlighted as follows:

- The overall GB accommodation in particular atomic diffusion along the GBs is decreased. This can be observed by comparing their magnitude of atomic displacements.
- The distance of GBD upwards motion is two atomic lattice spacing ($2d_{111}$) less. At higher rates this process must be driven by a higher load with the loading axis parallel to the GB 12-14. Emission/absorption of point defects from/ towards the dislocation core proceeds fast. In contrast, stress reduction followed by a long-term creep period allows GBD motion being controlled by GB diffusion, the driving force of which can arise from the concentration gradient of point defects (free volume) around the GBD. This may rationalize the motion of a perfect GBD in current simulations, whereas delocalized GBDs are suggested to facilitate GBD motion in Ref. [13].
- Dis1 emission is observed and remaining in the initial stage of propagation. This configuration is similar
- Confinement of delocalized GBD core is observed as well, however in the case of stress reduction a perfect GBD is finally formed.
- to that observed for the case of stress reduction at $t = 2085$ ps (see Figure 4-9). However, the latter identifies more atomic diffusion along the GB 12-14. Upon further straining after 110 ps in the case of without stress drop, one observes the propagation of dislocations from other slip systems with the highest Schmid factors and the reabsorption of Dis1. Dis2 emission from GB 12-14 is not detected.

Overall, the differences mentioned above can be rationalized by the role of time-dependent accommodation processes that result in different GB structures. The present work provides an overview of the first results. Furthering understanding in the occurrence of these mechanisms is still needed.

Table 5-2 Comparison of the number slip events and deformation time in continuous deformation with and without stress reduction when the same amount of strain is produced.

Deformation mode	Strain produced	Total number of slip events	Deformation time
Without stress drop	1.166 %	~10	110 ps
With stress drop		~8	2290 ps

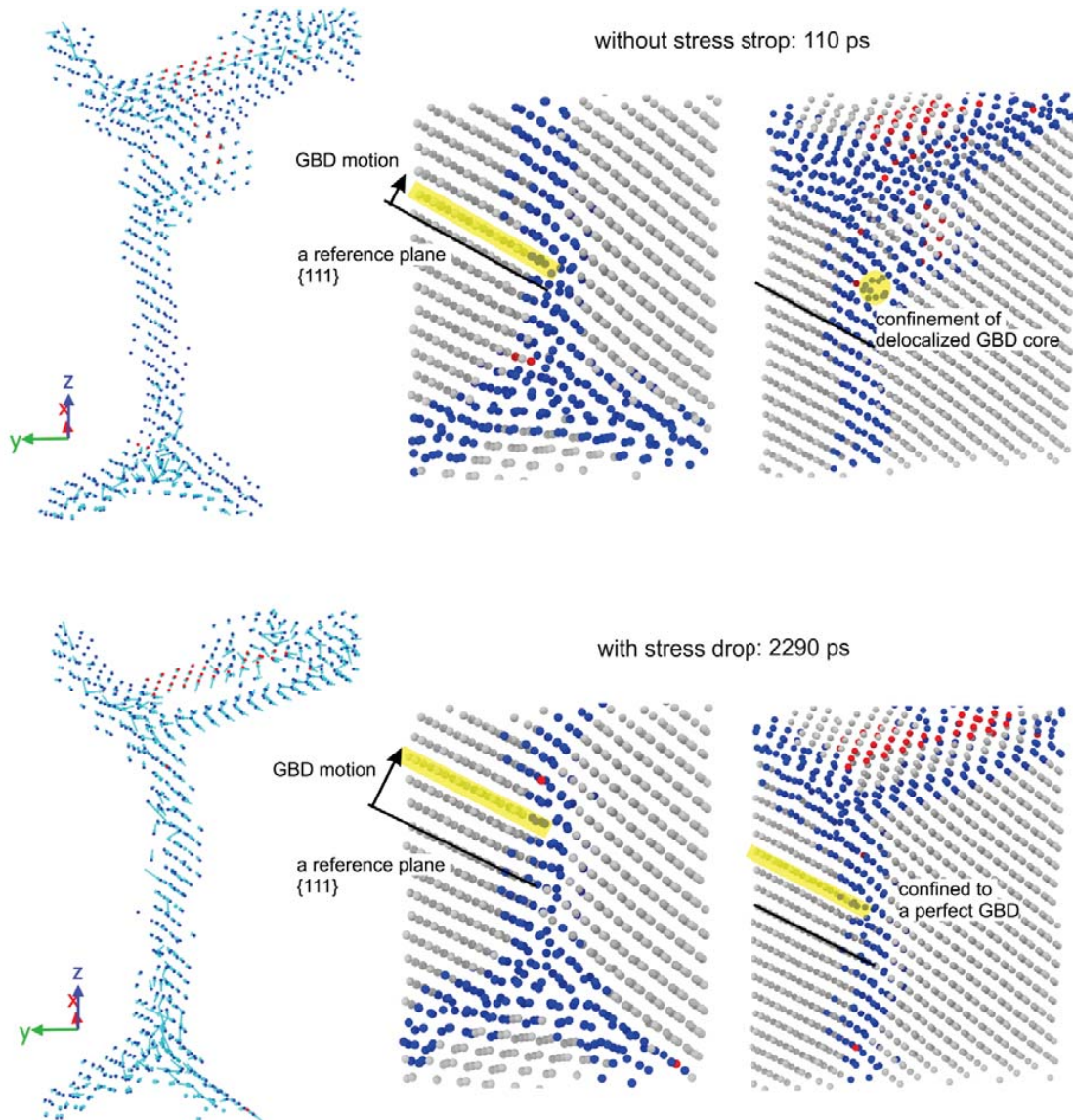


Figure 5-12 The configurations of continuous deformation with and without stress reduction are compared when the same amount of strain is produced. The inspection is carried out in the same sections of GB 12-14 as studied in Figure 4-11, Figure 4-7, and Figure 4-9.

Chapter 6 Conclusion

6.1 Achieved results

For NC materials, the stress-strain behaviour during uniaxial deformation (tension and compression) is usually characterized by a short initial work hardening followed by a constant flow stress regime. Within this thesis, three electrodeposited NC materials have been investigated: NC Ni₃₅, Ni₆₅, and Ni₅₀Fe₅₀ with the respective average grain size of 35 nm, 65 nm, and 15 nm. The *in situ* continuous deformation and *in situ* load-unload deformation on two NC Ni batches confirms previous observations for NC Ni from Goodfellow [15][18][94]. All materials exhibit minor grain growth under tension while the post-mortem TEM characterization implemented on NC Ni₃₅ evidences a modest grain coarsening under compression.

The development of a constant deformation resistance has been investigated and understood in terms of the interplay between different deformation mechanisms, in particular dislocation-based and GB accommodation mechanisms. The methods applied were stress reduction experiments: after a sufficient stress drop, dislocation slip is suppressed enough such that the role of GB accommodation on plastic deformation is made visible during long-term transient creep. Such a technique was combined with *in situ* X-ray diffraction, allowing identifying these two types of mechanisms by their opposite footprint on the peak broadening: in general, the dislocation slip increases the FWHM whereas the GB accommodation processes are expected to decrease the FWHM. To gain a comprehensive view of transient behaviour, stress reduction was performed either in a conventional way where the reduced stress was kept constant, or in a modified way where the reduced stress was stepwise increased, i.e. multistep test.

For NC Ni₃₅ batch:

- The *in situ* conventional stress reduction tests with different magnitudes of stress drop were respectively performed in tension and compression. Under tension stress reductions were conducted prior to the maximum flow stress where work-hardening remained present. Inspection of the transient behaviour of strain and FWHM as a function of the relative reduced stress R reveals the presence of four regimes as a consequence of a competition between dislocation-based and GB-mediated mechanisms. It is suggested that dislocation-based mechanisms dominate at high stress levels and GB-mediated mechanisms dominate at low stress levels. For a moderate stress reduction, a non-monotonic behaviour of FWHM was observed, suggesting an alternation of mechanisms. Under compression stress reductions were performed in the constant flow stress regime. The evidence of FWHM reduction irrespective of R indicates the dominance of GB-mediated mechanisms during transients. Both deformation modes demonstrate that GB accommodation processes play an important role in producing plastic strain and recovering defects and internal stresses. It is proposed that the constant flow stress reached during uniaxial deformation reflects a quasi-stationary state where the dislocation generation and recovery compensate each other reaching a dynamic equilibrium.
- The *in situ* multistep test provides an alternative way to approach a quasi-stationary state after the stress drop. Such type of test was carried out for a large stress reduction, showing consistency with the results revealed by conventional stress reduction tests. In addition, by comparing different types of

experiments performed (i.e. conventional stress reduction tests, multistep tests, and continuous deformation tests performed at different strain rates), a similar $\dot{\epsilon}$ - σ value near a given quasi-stationary state is obtained, suggesting the establishment of a characteristic balance between multiple deformation mechanisms independent of the deformation path.

- The fact that GB accommodation contributes to the plastic strain has a significant consequence for the parameters of thermally activated glide of dislocations (e.g. athermal stress and activation volume) that are traditionally derived from stress/ strain rate change tests. Within this thesis, it has been shown that the athermal stress is considerably lower when it is derived from the value of $\sigma_0 - \Delta\sigma$ with $\Delta\sigma$ corresponding to a threshold magnitude that results in a zero initial creep rate. For NC Ni₃₅, one obtains ~ 50 % of the σ_0 ; however, ~ 80 % of the σ_0 was measured once the contribution of GB-mediated mechanisms is subtracted from the overall strain rate.

For NC Ni₆₅ batch:

- The results for both Ni batches are qualitatively in good agreement. The main difference is that prior to the stress reduction, the relative contribution of GB-mediated processes to the overall strain rate is larger in NC Ni₃₅ (~ 24 %) than in NC Ni₆₅ (~ 12 %).

For NC Ni₅₀Fe₅₀ batch:

- The role of GB accommodation mechanisms during plastic deformation is confirmed. On the other hand, it exhibits some peculiar behaviour when compared to NC Ni batches, such as the lack of FWHM increase when creeping at high stress levels, larger plastic strains accompanied with more reduction of FWHM, and the presence of a reloading yield point that is also dependent on the prior strain reached. All these observations can be interpreted as superposition effects from alloying and grain size. Several possibilities for the interpretation are proposed, including strain aging, grain growth, and detwinning.

Inspired by the experimental transient testing, MD simulations of stress drops were carried out in the different stress drop regimes. The creep strain versus time curves after the stress drops depend on the magnitude of the stress drop, and exhibit similar trends as those for *in situ* experiments. As the stress drop increases, dislocation activity during creep periods is largely suppressed. For one test with a medium stress drop followed by long-term creep, detailed analysis of dislocation as well as GB activity reveals the following facts:

- Dislocation slip can continue to operate after the adaption of the GB structures by a variety of GB accommodation mechanisms. This suggests that the non-monotonic behaviour of the FWHM during transient creep (after initial reduction the FWHM increases again) can be indeed explained by the presence of GB accommodation mechanisms changing the character of the GBs.
- Compared with MD simulations performed during continuous deformation with very high strain rates (100-1000 times higher), the present simulations evidence more pronounced atomic diffusion along the GBs that is involved in different accommodation processes. It is expected that this is closer to experimental reality.

6.2 Outlook

The *in situ* stress reduction tests presented in this thesis suggest that GB-mediated plasticity may also contribute significantly to creep at room temperature. This is of practical importance in the application of NC materials under varying conditions. In manufacturing industry, as for instance Mimotec SA (Company Specialized in Manufacturing Microparts, Microcomponents, Microfluidics, Micromoulds per Technology UV-LIGA), ED NC Ni is widely used for manufacturing micromechanical components using UV-LIGA process. Components, as for instance springs, require the shape to be maintained when subjected to a demand load. However, the presence of creep/stress relaxation even in a small amount can have a detrimental effect on their functional properties.

To minimize creep effects while retaining the high strength, the following two aspects can be considered for the future development:

- To optimize the annealing process parameters: it is known that ED NC samples in as-prepared state exhibit large internal stress variation. This can be the driving force for creep/ stress relaxation at room temperature where GB structure relaxation produces the strain. To reduce internal stress sources without causing grain coarsening, optimization of post-mortem thermal treatment (temperature, annealing time etc.) can be the option. On the other hand, annealing promotes impurities segregation at the GBs, acting as pinning sites for dislocation/ GB activity.
- To explore grain size distributions effects: it is known that in a bimodal grain size distribution, the large grains give ductility while small grains are responsible for the high strength. It will be of great interest to have a comparison of creep/ relaxation behaviour between bimodal and homogeneous grain size distribution, and see which microstructure type gives the benefits to the desired mechanical properties.

For NC Ni₅₀Fe₅₀ the interpretation of the X-ray diffraction results is inherently more complex and open to many possible interpretations. For the sake of scientific interest and a potential practical application of NC alloys, further experimental work on NC Ni₅₀Fe₅₀ may involve:

- Deformation in compression mode: (1) continuous deformation tests with different strain rates help verify whether the maximum flow stresses reached in tensile tests reflect true quasi-stationary states. Further, *in situ* tests can be applied to see whether the peak broadening saturates in the stress plateau regime. This is particularly interesting since NC Ni₅₀Fe₅₀ lacks of pronounced increase in peak broadening upon tensile loading. (2) The *in situ* stress reduction under compression might shed light on the deformation mechanisms that occur at larger strains, such as grain coarsening. Also, one can verify whether dislocation-based mechanisms in NC Ni₅₀Fe₅₀ play an increasing role with strain, as suggested in the present work.
- ACOM-TEM as a complementary characterization technique: this technique provides a statistically quantitative evaluation of grain size distribution, crystal orientation, and texture evolution. By characterizing the as-prepared/ deformed microstructures, one may explore the mechanisms such as grain growth, detwinning, and grain rotation. However, due to very small grain size and the fact that the Ni₅₀Fe₅₀ is magnetic, TEM sample observations will be rather challenging.
- Mechanical tests at cryogenic and/ or elevated temperatures: by studying the influence of temperature on the deformation behaviour, one may further develop the knowledge on the deformation mechanisms of this NC alloy and explore its potential application at various temperatures. One has to

6.2 Outlook

keep in mind that the investigation of alloying effects on particular mechanisms, such as strain aging, should be carried out at a well-controlled temperature where grain growth and phase transformation are not involved.

- Repeat the stress reduction tests on NiFe samples with different compositions: by varying the Fe content while keeping the grain size constant the alloying effect could be addressed in more detail.

MD simulations of stress drops followed by creep provide an approach to explore the mechanisms that are not observed in higher strain rate atomistic simulations, as for instance vacancy emission due to dislocation interactions within a grain. Future work involves further understanding in the occurrence of this mechanism.

References

- [1] H. Gleiter, Nanocrystalline materials, in: P.D.W.G.J. Bunk (Ed.), *Adv. Struct. Funct. Mater.*, Springer Berlin Heidelberg, 1991: pp. 1–37.
- [2] C. Suryanarayana, Nanocrystalline materials, *Int. Mater. Rev.* 40 (1995) 41–64.
- [3] G. Palumbo, S.J. Thorpe, K.T. Aust, On the contribution of triple junctions to the structure and properties of nanocrystalline materials, *Scr. Metall. Mater.* 24 (1990) 1347–1350.
- [4] E.O. Hall, The Deformation and Ageing of Mild Steel: III Discussion of Results, *Proc. Phys. Soc. Sect. B.* 64 (1951) 747–753.
- [5] N.J. Petch, The Cleavage Strength of Polycrystals, *J Iron Steel Inst.* 174 (1953) 25–28.
- [6] A.H. Chokshi, A. Rosen, J. Karch, H. Gleiter, On the validity of the hall-petch relationship in nanocrystalline materials, *Scr. Metall.* 23 (1989) 1679–1683.
- [7] A.M. El-Sherik, U. Erb, G. Palumbo, K.T. Aust, Deviations from hall-petch behaviour in as-prepared nanocrystalline nickel, *Scr. Metall. Mater.* 27 (1992) 1185–1188.
- [8] G. Saada, Hall–Petch revisited, *Mater. Sci. Eng. A.* 400–401 (2005) 146–149.
- [9] J.R. Trelewicz, C.A. Schuh, The Hall–Petch breakdown in nanocrystalline metals: A crossover to glass-like deformation, *Acta Mater.* 55 (2007) 5948–5958.
- [10] M.A. Meyers, A. Mishra, D.J. Benson, Mechanical properties of nanocrystalline materials, *Prog. Mater. Sci.* 51 (2006) 427–556.
- [11] M. Dao, L. Lu, R.J. Asaro, J.T.M. De Hosson, E. Ma, Toward a quantitative understanding of mechanical behavior of nanocrystalline metals, *Acta Mater.* 55 (2007) 4041–4065.
- [12] H. Van Swygenhoven, M. Spaczer, A. Caro, D. Farkas, Competing plastic deformation mechanisms in nanophase metals, *Phys. Rev. B.* 60 (1999) 22–25.
- [13] H. Van Swygenhoven, P.M. Derlet, A. Hasnaoui, Atomic mechanism for dislocation emission from nanosized grain boundaries, *Phys. Rev. B.* 66 (2002) 24101.
- [14] P.M. Derlet, A. Hasnaoui, H. Van Swygenhoven, Atomistic simulations as guidance to experiments, *Scr. Mater.* 49 (2003) 629–635.
- [15] Z. Budrovic, H.V. Swygenhoven, P.M. Derlet, S.V. Petegem, B. Schmitt, Plastic Deformation with Reversible Peak Broadening in Nanocrystalline Nickel, *Science.* 304 (2004) 273–276.
- [16] F. Dalla Torre, Microstructure and mechanical properties of nanocrystalline Ni produced by three different synthesis techniques, *Diss. EPFL*, 2002.
- [17] K.S. Kumar, H. Van Swygenhoven, S. Suresh, Mechanical behavior of nanocrystalline metals and alloys, *Acta Mater.* 51 (2003) 5743–5774.
- [18] S. Brandstetter, H. Van Swygenhoven, Deformation mechanisms of nanocrystalline nickel studied by in-situ X-ray diffraction, *Diss. EPFL*, 2008.
- [19] Brandl, Christian, Deformation mechanism in nanocrystalline FCC metals studied by atomistic simulations, *Diss. EPFL*, 2010.

References

- [20] H. Van Swygenhoven, P.M. Derlet, A.G. Frøseth, Stacking fault energies and slip in nanocrystalline metals, *Nat. Mater.* 3 (2004) 399–403.
- [21] V. Yamakov, D. Wolf, S.R. Phillpot, H. Gleiter, Deformation twinning in nanocrystalline Al by molecular-dynamics simulation, *Acta Mater.* 50 (2002) 5005–5020.
- [22] A.G. Frøseth, P.M. Derlet, H. Van Swygenhoven, Twinning in Nanocrystalline fcc Metals, *Adv. Eng. Mater.* 7 (2005) 16–20.
- [23] H. Van Swygenhoven, P.M. Derlet, A.G. Frøseth, Nucleation and propagation of dislocations in nanocrystalline fcc metals, *Acta Mater.* 54 (2006) 1975–1983.
- [24] E. Bitzek, C. Brandl, P.M. Derlet, H. Van Swygenhoven, Dislocation Cross-Slip in Nanocrystalline fcc Metals, *Phys. Rev. Lett.* 100 (2008) 235501.
- [25] X.L. Wu, E. Ma, Dislocations in nanocrystalline grains, *Appl. Phys. Lett.* 88 (2006) 231911.
- [26] X. Wu, E. Ma, Y.T. Zhu, Deformation defects in nanocrystalline nickel, *J. Mater. Sci.* 42 (2007) 1427–1432.
- [27] F. Dalla Torre, H. Van Swygenhoven, M. Victoria, Nanocrystalline electrodeposited Ni: microstructure and tensile properties, *Acta Mater.* 50 (2002) 3957–3970.
- [28] K.S. Kumar, S. Suresh, M.F. Chisholm, J.A. Horton, P. Wang, Deformation of electrodeposited nanocrystalline nickel, *Acta Mater.* 51 (2003) 387–405.
- [29] R.C. Hugo, H. Kung, J.R. Weertman, R. Mitra, J.A. Knapp, D.M. Follstaedt, In-situ TEM tensile testing of DC magnetron sputtered and pulsed laser deposited Ni thin films, *Acta Mater.* 51 (2003) 1937–1943.
- [30] Z.W. Shan, J.M.K. Wiezorek, E.A. Stach, D.M. Follstaedt, J.A. Knapp, S.X. Mao, Dislocation Dynamics in Nanocrystalline Nickel, *Phys. Rev. Lett.* 98 (2007) 95502.
- [31] L. Wang, Z. Zhang, E. Ma, X.D. Han, Transmission electron microscopy observations of dislocation annihilation and storage in nanograins, *Appl. Phys. Lett.* 98 (2011) 51905.
- [32] M. Chen, E. Ma, K.J. Hemker, H. Sheng, Y. Wang, X. Cheng, Deformation Twinning in Nanocrystalline Aluminum, *Science*. 300 (2003) 1275–1277.
- [33] X.Z. Liao, Y.H. Zhao, S.G. Srinivasan, Y.T. Zhu, R.Z. Valiev, D.V. Gunderov, Deformation twinning in nanocrystalline copper at room temperature and low strain rate, *Appl. Phys. Lett.* 84 (2004) 592–594.
- [34] Y.T. Zhu, X.Z. Liao, X.L. Wu, Deformation twinning in bulk nanocrystalline metals: Experimental observations, *JOM*. 60 (2008) 60–64.
- [35] H.V. Swygenhoven, A. Caro, D. Farkas, Grain boundary structure and its influence on plastic deformation of polycrystalline FCC metals at the nanoscale: a molecular dynamics study, *Scr. Mater.* 8–9 (2001) 1513–1516.
- [36] H. Van Swygenhoven, D. Farkas, A. Caro, Grain-boundary structures in polycrystalline metals at the nanoscale, *Phys. Rev. B*. 62 (2000) 831–838.
- [37] H. Conrad, J. Narayan, On the grain size softening in nanocrystalline materials, *Scr. Mater.* 42 (2000) 1025–1030.

References

- [38] J. Schiøtz, F.D. Di Tolla, K.W. Jacobsen, Softening of nanocrystalline metals at very small grain sizes, *Nature*. 391 (1998) 561–563.
- [39] H. Van Swygenhoven, P.M. Derlet, Grain-boundary sliding in nanocrystalline fcc metals, *Phys. Rev. B*. 64 (2001) 224105.
- [40] A. Hasnaoui, H. Van Swygenhoven, P.M. Derlet, Cooperative processes during plastic deformation in nanocrystalline fcc metals: A molecular dynamics simulation, *Phys. Rev. B*. 66 (2002) 184112.
- [41] T. Shimokawa, A. Nakatani, H. Kitagawa, Grain-size dependence of the relationship between intergranular and intragranular deformation of nanocrystalline Al by molecular dynamics simulations, *Phys. Rev. B*. 71 (2005) 224110.
- [42] D. Farkas, S. Mohanty, J. Monk, Strain-driven grain boundary motion in nanocrystalline materials, *Mater. Sci. Eng. A*. 493 (2008) 33–40.
- [43] F. Sansoz, V. Dupont, Grain growth behavior at absolute zero during nanocrystalline metal indentation, *Appl. Phys. Lett.* 89 (2006) 111901.
- [44] M. Velasco, H. Van Swygenhoven, C. Brandl, Coupled grain boundary motion in a nanocrystalline grain boundary network, *Scr. Mater.* 65 (2011) 151–154.
- [45] A. Suzuki, Y.M. Mishin, Atomic Mechanisms of Grain Boundary Motion, *Mater. Sci. Forum*. 502 (2005) 157–162.
- [46] J.W. Cahn, Y. Mishin, A. Suzuki, Coupling grain boundary motion to shear deformation, *Acta Mater.* 54 (2006) 4953–4975.
- [47] D. Farkas, A. Frøseth, H. Van Swygenhoven, Grain boundary migration during room temperature deformation of nanocrystalline Ni, *Scr. Mater.* 55 (2006) 695–698.
- [48] V. Yamakov, D. Wolf, S.R. Phillpot, H. Gleiter, Grain-boundary diffusion creep in nanocrystalline palladium by molecular-dynamics simulation, *Acta Mater.* 50 (2002) 61–73.
- [49] R.W. Siegel, G.J. Thomas, Grain boundaries in nanophase materials, *Ultramicroscopy*. 40 (1992) 376–384.
- [50] G.J. Thomas, R.W. Siegel, J.A. Eastman, Grain boundaries in nanophase palladium : high resolution electron microscopy and image simulation, *Scr. Metall.* 24 (1990) 201–206.
- [51] S. Brandstetter, K. Zhang, A. Escudro, J.R. Weertman, H. Van Swygenhoven, Grain coarsening during compression of bulk nanocrystalline nickel and copper, *Scr. Mater.* 58 (2008) 61–64.
- [52] D.S. Gianola, S. Van Petegem, M. Legros, S. Brandstetter, H. Van Swygenhoven, K.J. Hemker, Stress-assisted discontinuous grain growth and its effect on the deformation behavior of nanocrystalline aluminum thin films, *Acta Mater.* 54 (2006) 2253–2263.
- [53] G.J. Fan, L.F. Fu, H. Choo, P.K. Liaw, N.D. Browning, Uniaxial tensile plastic deformation and grain growth of bulk nanocrystalline alloys, *Acta Mater.* 54 (2006) 4781–4792.
- [54] K. Zhang, J.R. Weertman, J.A. Eastman, Rapid stress-driven grain coarsening in nanocrystalline Cu at ambient and cryogenic temperatures, *Appl. Phys. Lett.* 87 (2005) 61921.
- [55] T.J. Rupert, D.S. Gianola, Y. Gan, K.J. Hemker, Experimental Observations of Stress-Driven Grain Boundary Migration, *Science*. 326 (2009) 1686–1690.

References

- [56] M. Legros, D.S. Gianola, K.J. Hemker, In situ TEM observations of fast grain-boundary motion in stressed nanocrystalline aluminum films, *Acta Mater.* 56 (2008) 3380–3393.
- [57] M. Jin, A.M. Minor, J.W. Morris Jr., Strain-induced coarsening in nano-grained films, *Thin Solid Films.* 515 (2007) 3202–3207.
- [58] B. Yang, H. Vehoff, A. Hohenwarter, M. Hafok, R. Pippan, Strain effects on the coarsening and softening of electrodeposited nanocrystalline Ni subjected to high pressure torsion, *Scr. Mater.* 58 (2008) 790–793.
- [59] Z. Shan, E.A. Stach, J.M.K. Wiezorek, J.A. Knapp, D.M. Follstaedt, S.X. Mao, Grain Boundary-Mediated Plasticity in Nanocrystalline Nickel, *Science.* 305 (2004) 654–657.
- [60] Y.B. Wang, B.Q. Li, M.L. Sui, S.X. Mao, Deformation-induced grain rotation and growth in nanocrystalline Ni, *Appl. Phys. Lett.* 92 (2008) 11903.
- [61] M.A. Meyers, E. Ashworth, A model for the effect of grain size on the yield stress of metals, *Philos. Mag. A.* 46 (1982) 737–759.
- [62] D.J. Benson, H.-H. Fu, M.A. Meyers, On the effect of grain size on yield stress: extension into nanocrystalline domain, *Mater. Sci. Eng. A.* 319–321 (2001) 854–861.
- [63] H.S. Kim, Y. Estrin, M.B. Bush, Constitutive modelling of strength and plasticity of nanocrystalline metallic materials, *Mater. Sci. Eng. A.* 316 (2001) 195–199.
- [64] R.J. Asaro, P. Krysl, B. Kad, Deformation mechanism transitions in nanoscale fcc metals, *Philos. Mag. Lett.* 83 (2003) 733–743.
- [65] R.J. Asaro, S. Suresh, Mechanistic models for the activation volume and rate sensitivity in metals with nanocrystalline grains and nano-scale twins, *Acta Mater.* 53 (2005) 3369–3382.
- [66] B. Zhu, R.J. Asaro, P. Krysl, R. Bailey, Transition of deformation mechanisms and its connection to grain size distribution in nanocrystalline metals, *Acta Mater.* 53 (2005) 4825–4838.
- [67] L. Li, M.G. Lee, P.M. Anderson, E. Bitzek, P.M. Derlet, H. Van Swygenhoven, A Quantized Crystal Plasticity Finite Element Model for Stress-Strain Response of Nanocrystalline Metals, *MATERIALS SCIENCE AND TECHNOLOGY-ASSOCIATION FOR IRON AND STEEL TECHNOLOGY- 3* (2007) 1542.
- [68] L. Li, P.M. Anderson, M.-G. Lee, E. Bitzek, P. Derlet, H.V. Swygenhoven, The stress–strain response of nanocrystalline metals: A quantized crystal plasticity approach, *Acta Mater.* 57 (2009) 812–822.
- [69] L. Li, S. Van Petegem, H. Van Swygenhoven, P.M. Anderson, Slip-induced intergranular stress redistribution in nanocrystalline Ni, *Acta Mater.* 60 (2012) 7001–7010.
- [70] J. Weissmüller, Proceedings of the First International Conference on Nanostructured Materials Alloy effects in nanostructures, *Nanostructured Mater.* 3 (1993) 261–272.
- [71] C.C. Koch, R.O. Scattergood, K.A. Darling, J.E. Semones, Stabilization of nanocrystalline grain sizes by solute additions, *J. Mater. Sci.* 43 (2008) 7264–7272.
- [72] R. Pippan, S. Scheriau, A. Taylor, M. Hafok, A. Hohenwarter, A. Bachmaier, Saturation of Fragmentation During Severe Plastic Deformation, *Annu. Rev. Mater. Res.* 40 (2010) 319–343.
- [73] T.J. Rupert, J.C. Trenkle, C.A. Schuh, Enhanced solid solution effects on the strength of nanocrystalline alloys, *Acta Mater.* 59 (2011) 1619–1631.

References

- [74] L.E. Murr, *Interfacial phenomena in metals and alloys*, (1975).
- [75] M. Ke, S.A. Hackney, W.W. Milligan, E.C. Aifantis, Observation and measurement of grain rotation and plastic strain in nanostructured metal thin films, *Nanostructured Mater.* 5 (1995) 689–697.
- [76] C.J. Youngdahl, R.C. Hugo, H. Kung, J.R. Weertman, TEM Observation of Nanocrystalline Copper During Deformation, *MRS Proceedings 634* (2000) B1.2.1–B1.2.6.
- [77] S.X. Mcfadden, A.V. Sergueeva, T. Kruml, J.-L. Martin, A.K. Mukherjee, Superplasticity in Nanocrystalline Ni₃Al and Ti Alloys, *MRS Proceedings 634* (2000) B1.3.1–B1.3.6.
- [78] L. Wang, X. Han, P. Liu, Y. Yue, Z. Zhang, E. Ma, In Situ Observation of Dislocation Behavior in Nanometer Grains, *Phys. Rev. Lett.* 105 (2010) 135501.
- [79] P. Liu, S.C. Mao, L.H. Wang, X.D. Han, Z. Zhang, Direct dynamic atomic mechanisms of strain-induced grain rotation in nanocrystalline, textured, columnar-structured thin gold films, *Scr. Mater.* 64 (2011) 343–346.
- [80] M.A. Haque, M.T.A. Saif, In-situ tensile testing of nano-scale specimens in SEM and TEM, *Exp. Mech.* 42 (2002) 123–128.
- [81] M.A. Haque, M.T.A. Saif, Application of MEMS force sensors for in situ mechanical characterization of nano-scale thin films in SEM and TEM, *Sens. Actuators Phys.* 97–98 (2002) 239–245.
- [82] M.A. Haque, M.T.A. Saif, Deformation mechanisms in free-standing nanoscale thin films: A quantitative in situ transmission electron microscope study, *Proc. Natl. Acad. Sci.* 101 (2004) 6335–6340.
- [83] M.A. Haque, M.T.A. Saif, In situ Tensile Testing of Nanoscale Freestanding Thin Films Inside a Transmission Electron Microscope, *J. Mater. Res.* 20 (2005) 1769–1777.
- [84] J. Rajagopalan, C. Rentenberger, H. Peter Karnthaler, G. Dehm, M.T.A. Saif, In situ TEM study of microplasticity and Bauschinger effect in nanocrystalline metals, *Acta Mater.* 58 (2010) 4772–4782.
- [85] Y. Zhu, H.D. Espinosa, An electromechanical material testing system for in situ electron microscopy and applications, *Proc. Natl. Acad. Sci.* 102 (2005) 14503–14508.
- [86] E. Hosseinian, O.N. Pierron, Quantitative in situ TEM tensile fatigue testing on nanocrystalline metallic ultrathin films, *Nanoscale.* 5 (2013) 12532–12541.
- [87] M.-S. Colla, B. Amin-Ahmadi, H. Idrissi, L. Malet, S. Godet, J.-P. Raskin, D. Schryvers, T. Pardoen, Dislocation-mediated relaxation in nanograined columnar palladium films revealed by on-chip time-resolved HRTEM testing, *Nat. Commun.* 6 (2015) 5922.
- [88] S. Gravier, M. Coulombier, A. Safi, N. Andre, A. BoÉ, J.P. Raskin, T. Pardoen, New On-Chip Nanomechanical Testing Laboratory - Applications to Aluminum and Polysilicon Thin Films, *J. Microelectromechanical Syst.* 18 (2009) 555–569.
- [89] T. Pardoen, A versatile lab-on-chip test platform to characterize elementary deformation mechanisms and electromechanical couplings in nanoscopic objects, *Comptes Rendus Phys.* 17 (2016) 485–495.

References

- [90] A. Kobler, A. Kashiwar, H. Hahn, C. Kübel, Combination of in situ straining and ACOM TEM: A novel method for analysis of plastic deformation of nanocrystalline metals, *Ultramicroscopy* 128 (2013) 68–81.
- [91] J. Lohmiller, M. Grewer, C. Braun, A. Kobler, C. Kübel, K. Schüler, V. Honkimäki, H. Hahn, O. Kraft, R. Birringer, P.A. Gruber, Untangling dislocation and grain boundary mediated plasticity in nanocrystalline nickel, *Acta Mater.* 65 (2014) 295–307.
- [92] F. Momprou, M. Legros, Quantitative grain growth and rotation probed by in-situ TEM straining and orientation mapping in small grained Al thin films, *Scr. Mater.* 99 (2015) 5–8.
- [93] S. Brandstetter, Ž. Budrović, S.V. Petegem, B. Schmitt, E. Stergar, P.M. Derlet, H.V. Swygenhoven, Temperature-dependent residual broadening of x-ray diffraction spectra in nanocrystalline plasticity, *Appl. Phys. Lett.* 87 (2005) 231910.
- [94] S. Brandstetter, H. Van Swygenhoven, S. Van Petegem, B. Schmitt, R. Maaß, P.M. Derlet, From Micro to Macroplasticity, *Adv. Mater.* 18 (2006) 1545–1548.
- [95] S. Van Petegem, S. Brandstetter, B. Schmitt, H. Van Swygenhoven, Creep in nanocrystalline Ni during X-ray diffraction, *Scr. Mater.* 60 (2009) 297–300.
- [96] H. Li, H. Choo, Y. Ren, T.A. Saleh, U. Lienert, P.K. Liaw, F. Ebrahimi, Strain-Dependent Deformation Behavior in Nanocrystalline Metals, *Phys. Rev. Lett.* 101 (2008) 15502.
- [97] S. Cheng, S.Y. Lee, L. Li, C. Lei, J. Almer, X.-L. Wang, T. Ungar, Y. Wang, P.K. Liaw, Uncommon Deformation Mechanisms during Fatigue-Crack Propagation in Nanocrystalline Alloys, *Phys. Rev. Lett.* 110 (2013) 135501.
- [98] S. Cheng, A.D. Stoica, X.-L. Wang, Y. Ren, J. Almer, J.A. Horton, C.T. Liu, B. Clausen, D.W. Brown, P.K. Liaw, L. Zuo, Deformation Crossover: From Nano- to Mesoscale, *Phys. Rev. Lett.* 103 (2009) 35502.
- [99] Y.M. Wang, R.T. Ott, A.V. Hamza, M.F. Besser, J. Almer, M.J. Kramer, Achieving Large Uniform Tensile Ductility in Nanocrystalline Metals, *Phys. Rev. Lett.* 105 (2010) 215502.
- [100] Y.M. Wang, R.T. Ott, M.F. Besser, A.V. Hamza, Temperature-dependent competing deformation mechanisms in nanocrystalline metals, *Phys. Rev. B.* 85 (2012) 144122.
- [101] D. Caillard, J.L. Martin, *Thermally Activated Mechanisms in Crystal Plasticity*, Elsevier, 2003.
- [102] F. Dalla Torre, P. Spätig, R. Schäublin, M. Victoria, Deformation behaviour and microstructure of nanocrystalline electrodeposited and high pressure torsioned nickel, *Acta Mater.* 53 (2005) 2337–2349.
- [103] Y.M. Wang, A.V. Hamza, E. Ma, Temperature-dependent strain rate sensitivity and activation volume of nanocrystalline Ni, *Acta Mater.* 54 (2006) 2715–2726.
- [104] Y.J. Li, J. Mueller, H.W. Höppel, M. Göken, W. Blum, Deformation kinetics of nanocrystalline nickel, *Acta Mater.* 55 (2007) 5708–5717.
- [105] V. Maier, K. Durst, J. Mueller, B. Backes, H.W. Höppel, M. Göken, Nanoindentation strain-rate jump tests for determining the local strain-rate sensitivity in nanocrystalline Ni and ultrafine-grained Al, *J. Mater. Res.* 26 (2011) 1421–1430.

References

- [106] Y.M. Wang, A.V. Hamza, E. Ma, Activation volume and density of mobile dislocations in plastically deforming nanocrystalline Ni, *Appl. Phys. Lett.* 86 (2005) 241917.
- [107] P. Spätig, J. Bonneville, J.-L. Martin, A new method for activation volume measurements: application to Ni₃(Al,Hf), *Mater. Sci. Eng. A.* 167 (1993) 73–79.
- [108] T. Kruml, O. Coddet, J.L. Martin, About the determination of the thermal and athermal stress components from stress-relaxation experiments, *Acta Mater.* 56 (2008) 333–340.
- [109] G. Guisbiers, M.-S. Colla, M. Coulombier, J.-P. Raskin, T. Pardoën, Study of creep/relaxation mechanisms in thin freestanding nanocrystalline palladium films through the lab-on-chip technology, *J. Appl. Phys.* 113 (2013) 24513.
- [110] T. Kruml, O. Coddet, J.L. Martin, The investigation of internal stress fields by stress reduction experiments, *Mater. Sci. Eng. A.* 387–389 (2004) 72–75.
- [111] T. Kruml, O. Coddet, J.-L. Martin, About stress reduction experiments during constant strain-rate deformation tests, *Z. Für Met.* 96 (2005) 589–594.
- [112] S.V. Petegem, S. Brandstetter, H.V. Swygenhoven, J.-L. Martin, Internal and effective stresses in nanocrystalline electrodeposited Ni, *Appl. Phys. Lett.* 89 (2006) 73102.
- [113] S. Van Petegem, J. Zimmermann, H. Van Swygenhoven, Microstructure and deformation mechanisms in nanocrystalline Ni–Fe. Part II. In situ testing during X-ray diffraction, *Acta Mater.* 61 (2013) 5846–5856.
- [114] W. Müller, M. Biberger, W. Blum, Subgrain-boundary migration during creep of lif III. Stress reduction experiments, *Philos. Mag. A.* 66 (1992) 717–728.
- [115] S. Mekala, P. Eisenlohr, W. Blum, Control of dynamic recovery and strength by subgrain boundaries – insights from stress-change tests on CaF₂ single crystals, *Philos. Mag.* 91 (2011) 908–931.
- [116] J. Hausselt, W. Blum, Dynamic recovery during and after steady state deformation of Al-11wt%Zn, *Acta Metall.* 24 (1976) 1027–1039.
- [117] W. Blum, A. Rosen, A. Cegielska, J.L. Martin, Two mechanisms of dislocation motion during creep, *Acta Metall.* 37 (1989) 2439–2453.
- [118] W. Blum, S. Vogler, M. Biberger, A.K. Mukherjee, Stress dependence of the creep rate at constant dislocation structure, *Mater. Sci. Eng. A.* 112 (1989) 93–106.
- [119] M. Biberger, J.C. Gibeling, Analysis of creep transients in pure metals following stress changes, *Acta Metall. Mater.* 43 (1995) 3247–3260.
- [120] W. Blum, *High-Temperature Deformation and Creep of Crystalline Solids*, in: *Mater. Sci. Technol.*, Wiley-VCH Verlag GmbH & Co. KGaA, 2006.
- [121] S. Van Petegem, J. Zimmermann, H. Van Swygenhoven, Yield point phenomenon during strain rate change in nanocrystalline Ni–Fe, *Scr. Mater.* 65 (2011) 217–220.
- [122] S. Van Petegem, J. Zimmermann, S. Brandstetter, X. Sauvage, M. Legros, H. Van Swygenhoven, Microstructure and deformation mechanisms in nanocrystalline Ni–Fe. Part I. Microstructure, *Acta Mater.* 61 (2013) 5835–5845.

References

- [123] Budrovic, Zeljka, Footprints of deformation mechanisms during in-situ x-ray diffraction: nanocrystalline and ultrafine grained materials, *Appl. Phys. Lett.* 86 (2005) 231910.
- [124] H.V. Swygenhoven, B. Schmitt, P.M. Derlet, S.V. Petegem, A. Cervellino, Z. Budrovic, S. Brandstetter, A. Bollhalder, M. Schild, Following peak profiles during elastic and plastic deformation: A synchrotron-based technique, *Rev. Sci. Instrum.* 77 (2006) 13902.
- [125] P. Eisenloh, W. Blum, SmooMuDS: A versatile tool for data reduction and smoothing for determination of noise-free rates, in particular deformation rates of materials, (2015).
- [126] <http://www.gmp.wm.uni-erlangen.de/SmooMuDS.php>.
- [127] P. Weidinger, W. Blum, U. Hunsche, A. Hampel, The influence of friction on plastic deformation in compression tests, *Phys. Status Solidi A.* 156 (1996) 305–315.
- [128] P.R. Willmott, D. Meister, S.J. Leake, M. Lange, A. Bergamaschi, M. Böge, M. Calvi, C. Cancellieri, N. Casati, A. Cervellino, Q. Chen, The materials science beamline upgrade at the Swiss Light Source, *J. Synchrotron Rad.* 20 (2013) 667–682.
- [129] F. Gozzo, B. Schmitt, Th. Bortolamedi, C. Giannini, A. Guagliardi, M. Lange, D. Meister, D. Maden, P. Willmott, B.D. Patterson, First experiments at the Swiss Light Source Materials Science beamline powder diffractometer, *J. Alloys Compd.* 362 (2004) 206–217.
- [130] B.E. Warren, *X-ray Diffraction*, Courier Corporation, 1969.
- [131] B.E. Warren, B.L. Averbach, The Effect of Cold-Work Distortion on X-Ray Patterns, *J. Appl. Phys.* 21 (1950) 595–599.
- [132] N.C. Halder, C.N.J. Wagner, Separation of particle size and lattice strain in integral breadth measurements, *Acta Crystallogr.* 20 (1966) 312–313.
- [133] H. Van Swygenhoven, S. Van Petegem, In-situ mechanical testing during X-ray diffraction, *Mater. Charact.* 78 (2013) 47–59.
- [134] L. Li, T. Ungár, Y.D. Wang, J.R. Morris, G. Tichy, J. Lendvai, Y.L. Yang, Y. Ren, H. Choo, P.K. Liaw, Microstructure evolution during cold rolling in a nanocrystalline Ni–Fe alloy determined by synchrotron X-ray diffraction, *Acta Mater.* 57 (2009) 4988–5000.
- [135] S. Cheng, Y. Zhao, Y. Guo, Y. Li, Q. Wei, X.-L. Wang, Y. Ren, P.K. Liaw, H. Choo, E.J. Lavernia, High Plasticity and Substantial Deformation in Nanocrystalline NiFe Alloys Under Dynamic Loading, *Adv. Mater.* 21 (2009) 5001–5004.
- [136] S. Ni, Y.B. Wang, X.Z. Liao, S.N. Alhajeri, H.Q. Li, Y.H. Zhao, E.J. Lavernia, S.P. Ringer, T.G. Langdon, Y.T. Zhu, Grain growth and dislocation density evolution in a nanocrystalline Ni–Fe alloy induced by high-pressure torsion, *Scr. Mater.* 64 (2011) 327–330.
- [137] D. Frenkel, B. Smit, *Understanding Molecular Simulations: from Algorithms to Applications*, (1996).
- [138] S. Plimpton, Fast Parallel Algorithms for Short-Range Molecular Dynamics, *J. Comput. Phys.* 117 (1995) 1–19.
- [139] <http://lammmps.sandia.gov>

References

- [140] G. Voronoi, Nouvelles applications des paramètres continus à la théorie des formes quadratiques. Deuxième mémoire. Recherches sur les paralléloèdres primitifs., *J. Für Reine Angew. Math.* 134 (1908) 198–287.
- [141] Y. Mishin, D. Farkas, M.J. Mehl, D.A. Papaconstantopoulos, Interatomic Potentials for Al and Ni From Experimental Data and AB Initio Calculations, in: *Symp. J – Multiscale Model. Mater.*, 1998: p. 535.
- [142] H. Van Swygenhoven, J.R. Weertman, Deformation in nanocrystalline metals, *Mater. Today*. 9 (2006) 24–31.
- [143] A. Stukowski, Visualization and analysis of atomistic simulation data with OVITO—the Open Visualization Tool, *Model. Simul. Mater. Sci. Eng.* 18 (2010) 15012.
- [144] <http://ovito.org>.
- [145] D. Faken, H. Jónsson, Systematic analysis of local atomic structure combined with 3D computer graphics, *Comput. Mater. Sci.* 2 (1994) 279–286.
- [146] H. Van Swygenhoven, P.M. Derlet, Chapter 81 Atomistic Simulations of Dislocations in FCC Metallic Nanocrystalline Materials, in: John Hirth (Ed.), *Dislocations Solids*, Elsevier, 2008: pp. 1–42.
- [147] J. Cormier, J.M. Rickman, T.J. Delph, Stress calculation in atomistic simulations of perfect and imperfect solids, *J. Appl. Phys.* 89(2001) 99–104.
- [148] F. Shimizu, S. Ogata, J. Li, Theory of Shear Banding in Metallic Glasses and Molecular Dynamics Calculations, *Mater. Trans.* 48 (2007) 2923–2927.
- [149] L. Thilly, S.V. Petegem, P.-O. Renault, F. Lecouturier, V. Vidal, B. Schmitt, H.V. Swygenhoven, A new criterion for elasto-plastic transition in nanomaterials: Application to size and composite effects on Cu–Nb nanocomposite wires, *Acta Mater.* 57 (2009) 3157–3169.
- [150] S. Brandstetter, P.M. Derlet, S. Van Petegem, H. Van Swygenhoven, Williamson–Hall anisotropy in nanocrystalline metals: X-ray diffraction experiments and atomistic simulations, *Acta Mater.* 56 (2008) 165–176.
- [151] J.L. Martin, B. Lo Piccolo, T. Kruml, J. Bonneville, Characterization of thermally activated dislocation mechanisms using transient tests, *Mater. Sci. Eng. A.* 322 (2002) 118–125.
- [152] J.L. Martin, T. Kruml, Characterizing thermally activated dislocation mobility, *J. Alloys Compd.* 378 (2004) 2–12.
- [153] H. Van Swygenhoven, A. Caro, D. Farkas, A molecular dynamics study of polycrystalline fcc metals at the nanoscale: grain boundary structure and its influence on plastic deformation, *Mater. Sci. Eng. A.* 309–310 (2001) 440–444.
- [154] R.E. Miller, L.E. Shilkrot, W.A. Curtin, A coupled atomistics and discrete dislocation plasticity simulation of nanoindentation into single crystal thin films, *Acta Mater.* 52 (2004) 271–284.
- [155] X. Li, Y. Wei, W. Yang, H. Gao, Competing grain-boundary- and dislocation-mediated mechanisms in plastic strain recovery in nanocrystalline aluminum, *Proc. Natl. Acad. Sci.* 106 (2009) 16108–16113.
- [156] V. Yamakov, D. Wolf, M. Salazar, S.R. Phillpot, H. Gleiter, Length-scale effects in the nucleation of extended dislocations in nanocrystalline Al by molecular-dynamics simulation, *Acta Mater.* 49 (2001) 2713–2722.

References

- [157] A. Hasnaoui, H. Van Swygenhoven, P.M. Derlet, On non-equilibrium grain boundaries and their effect on thermal and mechanical behaviour: a molecular dynamics computer simulation, *Acta Mater.* 50 (2002) 3927–3939.
- [158] H. van Swygenhoven, P.M. Derlet, Z. Budrovic, A. Hasnaoui, Unconventional deformation mechanism in nanocrystalline metals?, *Z. Für Met.* 94 (2003) 1106–1110.
- [159] G. SAADA, From the single crystal to the nanocrystal, *Philos. Mag.* 85 (2005) 3003–3018.
- [160] W. Blum, P. Eisenlohr, Dislocation mechanics of creep, *Mater. Sci. Eng. A.* 510–511 (2009) 7–13.
- [161] Y.J. Li, X.H. Zeng, W. Blum, Transition from strengthening to softening by grain boundaries in ultrafine-grained Cu, *Acta Mater.* 52 (2004) 5009–5018.
- [162] T. Chan, D. Backman, R. Bos, T. Sears, I. Brooks, U. Erb, In Situ Heat Generation and Strain Localization of Polycrystalline and Nanocrystalline Nickel, in: *Thermomechanics Infra-Red Imaging Vol. 7*, Springer New York, 2011: pp. 17–23.
- [163] R. Schwaiger, B. Moser, M. Dao, N. Chollacoop, S. Suresh, Some critical experiments on the strain-rate sensitivity of nanocrystalline nickel, *Acta Mater.* 51 (2003) 5159–5172.
- [164] F. Mompou, M. Legros, A. Boé, M. Coulombier, J.-P. Raskin, T. Pardoen, Inter- and intragranular plasticity mechanisms in ultrafine-grained Al thin films: An in situ TEM study, *Acta Mater.* 61 (2013) 205–216.
- [165] D.V. Bachurin, P. Gumbsch, Accommodation processes during deformation of nanocrystalline palladium, *Acta Mater.* 58 (2010) 5491–5501.
- [166] X.Z. Liao, A.R. Kilmametov, R.Z. Valiev, H. Gao, X. Li, A.K. Mukherjee, J.F. Bingert, Y.T. Zhu, High-pressure torsion-induced grain growth in electrodeposited nanocrystalline Ni, *Appl. Phys. Lett.* 88 (2006) 21909.
- [167] X.L. Wu, Y.T. Zhu, Y.G. Wei, Q. Wei, Strong Strain Hardening in Nanocrystalline Nickel, *Phys. Rev. Lett.* 103 (2009) 205504.
- [168] A. Kulovits, S.X. Mao, J.M.K. Wiezorek, Microstructural changes of nanocrystalline nickel during cold rolling, *Acta Mater.* 56 (2008) 4836–4845.
- [169] X. Shen, J. Lian, Z. Jiang, Q. Jiang, High strength and high ductility of electrodeposited nanocrystalline Ni with a broad grain size distribution, *Mater. Sci. Eng. A.* 487 (2008) 410–416.
- [170] C.D. Gu, J.S. Lian, Q. Jiang, W.T. Zheng, Experimental and modelling investigations on strain rate sensitivity of an electrodeposited 20 nm grain sized Ni, *J. Phys. Appl. Phys.* 40 (2007) 7440.
- [171] H. Neuhäuser, C. Schwink, Solid Solution Strengthening, in: *Mater. Sci. Technol.*, Wiley-VCH Verlag GmbH & Co. KGaA, 2006.
- [172] S. Cheng, Y. Zhao, Y. Wang, Y. Li, X.-L. Wang, P.K. Liaw, E.J. Lavernia, Structure Modulation Driven by Cyclic Deformation in Nanocrystalline NiFe, *Phys. Rev. Lett.* 104 (2010) 255501.
- [173] Y.B. Wang, J.C. Ho, X.Z. Liao, H.Q. Li, S.P. Ringer, Y.T. Zhu, Mechanism of grain growth during severe plastic deformation of a nanocrystalline Ni–Fe alloy, *Appl. Phys. Lett.* 94 (2009) 11908.

References

- [174] S. Ni, Y.B. Wang, X.Z. Liao, S.N. Alhajeri, H.Q. Li, Y.H. Zhao, E.J. Lavemia, S.P. Ringer, T.G. Langdon, Y.T. Zhu, Strain hardening and softening in a nanocrystalline Ni–Fe alloy induced by severe plastic deformation, *Mater. Sci. Eng. A.* 528 (2011) 3398–3403.
- [175] L.E. Murr, *Interfacial phenomena in metals and alloys*, (1975).
- [176] W. Charnock, J. Nutting, The Effect of Carbon and Nickel upon the Stacking-Fault Energy of Iron, *Met. Sci. J.* 1 (1967) 123–127.
- [177] R.E. Schramm, R.P. Reed, Stacking fault energies of fcc Fe–Ni alloys by x-ray diffraction line profile analysis, *Metall. Trans. A.* 7 (1976) 359–363.
- [178] J.D. Giallonardo, G. Avramovic-Cingara, G. Palumbo, U. Erb, Microstrain and growth fault structures in electrodeposited nanocrystalline Ni and Ni–Fe alloys, *J. Mater. Sci.* 48 (2013) 6689–6699.
- [179] L. Li, T. Ungár, Y.D. Wang, J.R. Morris, G. Tichy, J. Lendvai, Y.L. Yang, Y. Ren, H. Choo, P.K. Liaw, Microstructure evolution during cold rolling in a nanocrystalline Ni–Fe alloy determined by synchrotron X-ray diffraction, *Acta Mater.* 57 (2009) 4988–5000.
- [180] A. Cottrell, *Dislocations and plastic flow in crystals.*, Clarendon Press, Oxford, 1953.
- [181] L.P. Kubin, Y. Estrin, The Portevin-Le Chatelier effect in deformation with constant stress rate, *Acta Metall.* 33 (1985) 397–407.
- [182] L.P. Kubin, Y. Estrin, Evolution of dislocation densities and the critical conditions for the Portevin-Le Chatelier effect, *Acta Metall. Mater.* 38 (1990) 697–708.
- [183] L.P. Kubin, Y. Estrin, C. Perrier, On static strain ageing, *Acta Metall. Mater.* 40 (1992) 1037–1044.
- [184] N. Wang, Z. Wang, K.T. Aust, U. Erb, Room temperature creep behavior of nanocrystalline nickel produced by an electrodeposition technique, *Mater. Sci. Eng. A.* 237 (1997) 150–158.
- [185] W.M. Yin, S.H. Whang, R. Mirshams, C.H. Xiao, Creep behavior of nanocrystalline nickel at 290 and 373 K, *Mater. Sci. Eng. A.* 301 (2001) 18–22.

Curriculum Vitae

Zhen Sun

Date of birth: 16.Oct 1985
Place of birth: Suzhou, China

Education

- 06/2012 - present **PhD** **École polytechnique fédérale de Lausanne, Switzerland**
Materials Science and Engineering
Paul Scherer Institute, Switzerland
-supervise a summer student on the project of MimotecSA
- 09/2008 - 08/2011 **MSc** **Rheinisch-Westfälische Technische Hochschule Aachen, Germany**
Metallurgical Engineering
- 09/2004 - 07/2008 **BSc** **University of Science and Technology Beijing, China**
Materials Science and Engineering

Publications

- Z. Sun, S. Van Petegem, A. Cervellino, K. Durst, W. Blum, H. Van Swygenhoven, Dynamic recovery in nanocrystalline Ni, *Acta Mater.* 91 (2015) 91–100.
- Z. Sun, S. Van Petegem, A. Cervellino, W. Blum, and H. Van Swygenhoven, Grain size and alloying effects on dynamic recovery in nanocrystalline metals, *Acta Mater.* (submitted in April 2016)
- Z. Sun, M. Dupraz, C. Brandl, and H. Van Swygenhoven, Stress reduction tests in molecular dynamics simulations, *Acta Mater.* (in preparation)

Conferences/Workshops

Oral presentation

- 12/1015 2015 MRS Fall Meeting & Exhibit, United States
08/2015 17th International Conference on the Strength of Materials, Czech Republic
12/2014 2014 MRS Fall Meeting & Exhibit, United States
09/2014 MSE 2014, Germany
09/2014 3rd General Meeting of the GDRi CNRS "Mechanics of Nano-objects", Switzerland
09/2013 Euromat 2013, Spain
07/2013 GDRi CNRS Mecano General Meeting on the Mechanics of Nano-objects, Germany

Poster

- 07/2014 Gordon Research Conferences "Structural Nanomaterials", China
03/2014 Gradschool CNRS "Solid Mechanics for Nanoscientists", France
10/2013 Small Scale Plasticity International School, France

